Study of supernova remnants with H.E.S.S. and analysis of prototype data of the FlashCam Cherenkov Camera

Dissertation

der Mathematisch-Naturwissenschaftlichen Fakultät
der Eberhard Karls Universität Tübingen
zur Erlangung des Grades eines
Doktors der Naturwissenschaften
(Dr. rer. nat.)

vorgelegt von
Massimo Capasso
aus Bari, Italien

Tübingen
2019

Gedruckt mit Genehmigung der Mathematisch-Naturwissenschaftlichen Fakultät der Eberhard Karls Universität Tübingen.

Tag der mündlichen Qualifikation:	03.05.2019
Dekan:	Prof. Dr. Wolfgang Rosenstiel
1. Berichterstatter:	Prof. Dott. Andrea Santangelo
2. Berichterstatter:	Prof. Dr. Josef Jochum

"Ma vie n'est pas derrière moi, ni avant, ni maintenant. Elle est dedans."

J. Prévert

Abstract

This thesis will present the results of two data analysis projects conducted in the framework of the H.E.S.S. (High Energy Stereoscopic System) Collaboration. H.E.S.S. is a system of five Cherenkov telescopes located in Namibia, which detect VHE (Very High Energy) γ-rays from Galactic and Extragalactic sources. Both of the presented projects focus on Galactic supernova remnants (SNRs), which are among the astrophysical objects known to emit VHE γ-rays.

Supernova remnants are the remains of a star exploding into a so-called supernova. More precisely, due to the explosion, the outer layers of the pre-supernova star are ejected at high velocity and particles are accelerated by the shock wave up to very high energies, hundreds of times higher than those reached at the Large Hadron Collider (LHC), currently the most powerful particle accelerator on Earth. One of the key reasons why SNRs are of particular interest in the astrophysics community is that they are believed to be responsible for the production and acceleration of the bulk of Galactic Cosmic Rays (CRs) (hydrogen and helium nuclei and heavier particles). In this context, VHE γ-rays produced by the interaction of the supernova ejecta with the ambient medium provide a clean tracer to probe this hypothesis, though a definite answer on the topic is yet to be found.

Given these premises, this work is structured as follows:

Chapter 1 will provide an introduction on VHE γ-ray astronomy. The driving idea is to try and follow a sequence of questions. How does the sky actually look in VHE γ-rays? How are the latter produced? Where do they come from, i.e., which are the astrophysical sources that produce them? How can we detect them?

Chapter 2 focuses on the search for new supernova remnants in our Galaxy with the H.E.S.S. experiment. In the energy range covered with H.E.S.S., the only way to identify new supernova remnant candidates is by their shell-like appearance. The idea of this work was then to scan the H.E.S.S. dataset looking for shell-like structures and see if they could be confirmed as supernova remnants. This morphological search criterion is not new in the astrophysics community; however, it was the first time, to our knowledge, in which it was successfully applied to VHE γ-ray data. The search led to the identification of three new significant shell structures; one of them could be confirmed as supernova remnant.

Chapter 3 presents a second analysis project involving the study of a supernova remnant and of its surroundings. As mentioned above, VHE γ-rays can be produced in the interaction between CRs accelerated at a supernova remnant shock-front and the ambient medium (consisting of both atomic and molecular gas). Therefore, if the VHE γ-ray emission from a supernova remnant or from its neighborhood is found to be coincident with known dense gas regions, this shows that such a process is likely taking place. Having this in mind, a correlation study between the VHE γ-ray and gas emission from the supernova remnant HESS J1731$-$347 region was carried out. The physical implications of the outcome of this study are then discussed.

Finally, a glance at the future. The Astronomy and Astrophysics Institute of the University of Tübingen is currently contributing to the development of the next-generation ground-based VHE γ-ray telescopes, the Cherenkov Telescope Array (CTA). One of the projects concerns the realization of the focal plane instrument for one of the telescope types foreseen by CTA. In this context, an analysis of prototype data was performed. This thesis concludes with an overview of the main results obtained so far (Chapter 4).

Kurzzusammenfassung

In dieser Dissertation werden die Ergebnisse von zwei Datenanalyse-Projekten vorgestellt, die im Rahmen der H.E.S.S. (High Energy Stereoscopic System) Kollaboration durchgeführt wurden. H.E.S.S. ist ein System aus fünf Cherenkov-Teleskopen in Namibia, die VHE (Very High Energy) Gammastrahlung aus galaktischen und extragalaktischen Quellen detektieren. Beide vorgestellten Projekte konzentrieren sich auf galaktische Supernovaüberreste (Supernova remnants, SNRs), astrophysikalische Objekte, von denen bekannt ist, dass sie VHE Gammastrahlung ausstrahlen.

Supernovaüberreste sind die Überbleibsel eines Sterns, der als Supernova explodiert ist. Durch die Explosion wurden die äußeren Schichten des Prä-Supernova-Sterns mit hoher Geschwindigkeit ausgestoßen, und durch die Shockwelle wurden Teilchen auf sehr hohe Energien beschleunigt; die erreichten Energien sind hundertfach höher als beim Large Hadron Collider (LHC), dem stärksten von Menschen gebauten Teilchenbeschleuniger der Erde. SNRs sind besonders interessant, weil sie wahrscheinlich für die Produktion und Beschleunigung der Kosmischen Strahlung (Wasserstoff- und Heliumkerne sowie schwerere Teilchen) verantwortlich sind. In diesem Zusammenhang bietet VHE-Gammastrahlung, durch die Wechselwirkung der ausgestoßenen Materie mit dem Umgebungsmedium erzeugt wird, eine Möglichkeit, um diese Hypothese zu untersuchen, wobei eine eindeutige Antwort auf das Thema noch nicht gefunden werden konnte.

Die vorliegende Arbeit ist wie folgt strukturiert:

Kapitel 1 enthält eine Einführung in die VHE Gammastrahlen-Astronomie. Diese orientiert sich dabei an den folgenden Fragen: Wie sieht der Himmel im Bereich der VHE-Gammastrahlung aus? Wie wird diese produziert? Woher kommt sie, d.h. aus welchen astrophysikalischen Quellen stammt sie? Wie können wir sie detektieren?

Kapitel 2 beschäftigt sich mit der Suche nach neuen Supernovaüberresten in unserer Galaxie mit dem H.E.S.S. Experiment. Im Energiebereich, der mit H.E.S.S. abgedeckt wird, ist der einzige Weg um neue Supernovaüberrestkandidaten zu identifizieren, ihr ringförmiges Aussehen. Die Idee dieser Arbeit ist deswegen, den H.E.S.S. Datensatz zu untersuchen, um ringförmige Strukturen zu finden, und sehen, ob sie als Supernovaüberreste klassifiziert werden könnten. Dieses morphologische Suchkriterium ist in der astrophysikalischen Gemeinschaft nicht neu; es war jedoch unseres Wissens das erste Mal, dass es erfolgreich auf VHE-Gammastrahlung-Daten angewendet wurde. Die Suche führte zur Identifizierung von drei neuen signifikanten Strukturen; eine konnte als Supernovaüberrest bestätigt werden.

In Kapitel 3 wird ein zweites Datenanalyse-Projekt vorgestellt, bei dem ein Supernovaüberrest und seine Umgebung untersucht werden. Wie oben erwähnt, könnte VHE-Gammastrahlung in der Wechselwirkung zwischen CRs, die an der Shockwelle eines Supernovaüberrests beschleunigt werden, und dem Umgebungsmedium (bestehend aus atomarem und molekularem Gas) erzeugt werden. Wenn sich herausstellt, dass die

VHE-Gammastrahlung eines Supernovaüberrests oder seiner Umgebung mit bekannten Regionen mit dichtem Gas zusammenfällt, zeigt dies, dass wahrscheinlich ein solcher Prozess stattfindet. Vor diesem Hintergrund wurde eine Korrelationsstudie zwischen der VHE-Gammastrahlung und der Gasemission aus dem Supernovaüberrest HESS J1731-347 durchgeführt. Anschließend werden die Implikationen des Ergebnisses dieser Studie diskutiert.

Zum Schluss noch ein Blick in die Zukunft. Das Institut für Astronomie und Astrophysik der Universität Tübingen leistet derzeit einen Beitrag zur Entwicklung der bodengestützten Gammateleskope der nächsten Generation, des Cherenkov Telescope Array (CTA). Eines der Projekte betrifft die Realisierung des Fokalinstruments für einen der von CTA vorgesehenen Teleskoptypen. In diesem Zusammenhang wurde eine Analyse von Prototypdaten durchgeführt. Diese Arbeit schließt mit einem Überblick über die wichtigsten bisher erzielten Ergebnisse (Kapitel 4).

Contents

List of Figures

List of Tables

List of Abbreviations

AGN	**A**ctive **G**alactic **N**ucleus
AIC	**A**kaike **I**nformation **C**riterion
CC	**C**ore **C**ollapse
CCO	**C**entral **C**ompact **O**bject
CRs	**C**osmic **R**ays
CTA	**C**herenkov **T**elescope **A**rray
d.o.f.	**d**egree **o**f **f**reedom
DAQ	**D**ata **A**cquisition
ECPL	**E**xponential **c**utoff **p**ower **l**aw
ESO	**E**uropean **S**outhern **O**bservatory
FC	**F**lash **C**am
FOV	**F**ield **O**f **V**iew
GRB	**G**amma **R**ay **B**urst
H.E.S.S.	**H**igh **E**nergy **S**tereoscopic **S**ystem
IAAT	**I**nstitut für **A**stronomie und **A**strophysik **T**übingen
ISM	**I**nterstellar **M**edium
LHC	**L**arge **H**adron **C**ollider
LST	**L**arge-**S**ized **T**elescope
MAGIC	**M**ajor **A**tmospheric **G**amma-ray **I**maging **C**herenkov
MST	**M**edium-**S**ized **T**elescope
NSB	**N**ight-**S**ky **B**ackground
p.e.	**p**hoto-**e**lectron(s)
PDP	**P**hoto **D**etector **P**lane
PL	**P**ower **l**aw
PMT	**P**hoto **M**ultiplier **T**ube
ROI	**R**egion **O**f **I**nterest
ROS	**R**eadout **S**ystem
SMA	**S**liding **M**oving **A**verage
SN	**S**upernova
SNR	**S**upernova **R**emnant
SPE	**S**ingle **P**hoto **E**lectron
SST	**S**mall-**S**ized **T**elescope
VERITAS	**V**ery **E**nergetic **R**adiation **I**maging **T**elescope **A**rray **S**ystem
VHE	**V**ery **H**igh **E**nergy

Chapter 1

VHE γ-ray astronomy: a powerful window on the energetic sky

1.1 How does the sky look like in VHE γ-rays?

When one lifts his eyes up to the night sky, what he expects to see is similar to what shown in Figure 1.1.

As it often happens, however, what one can observe naked-eye represents a very small portion of a much bigger picture. Using a very nice *musical* comparison, limiting to the optical band would be like playing just one octave on a piano, having about 70 at disposal! γ-radiation alone spans 20 octaves and offers the possibility to investigate the most energetic phenomena of the Universe.

The data that were used for this work cover the so-called *very high energy* part of the γ-radiation, which ranges between $\sim 0.1 - 100\,\mathrm{TeV}$. How does the sky look like in VHE γ-rays then? Figure 1.2 shows the VHE γ-ray image of the inner part of the Milky Way at longitudes from $l = 250°$ to $65°$, latitudes $|b| \leq 3.5°$, in four longitude slices. This image was produced with the data from the latest survey of the Galactic plane with H.E.S.S. (H.E.S.S. Collaboration et al., 2018b) and was the starting point of the study presented in Chapter 2.

The number of known VHE γ-ray sources is fairly small compared to the optical ones, and some of them have been extensively studied over the past 20 years (e.g. the supernova remnant shell RX J1713.7−3946). However, the answer to the question on the origin of this emission is still matter of debate for many physical objects. To be more precise: the radiation processes that lead to the production of VHE γ-rays are actually well known from particle physics. The real challenge consists in trying to disentangle the contribution from each of them to the actually observed emission from a given object.

The following paragraphs will give an overview of these processes, of the sources where they take place and of the instruments capable of detecting VHE γ-rays.

1.2 Emission mechanisms

The production of γ-rays from astrophysical sources usually takes place when accelerated particles (electrons, protons or heavier nuclei) interact with the ambient matter (thermal gas) and electromagnetic fields. In the literature several classifications of these processes are

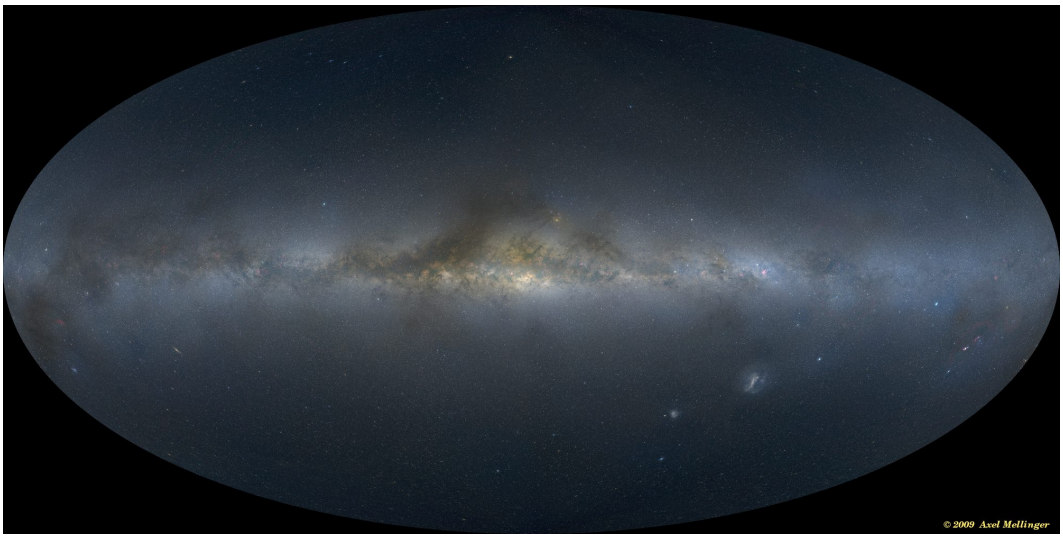

FIGURE 1.1: A. Mellinger, A Color All-Sky Panorama Image of the Milky Way, **Publ. Astron. Soc. Pacific 121, 1180-1187 (2009)**.

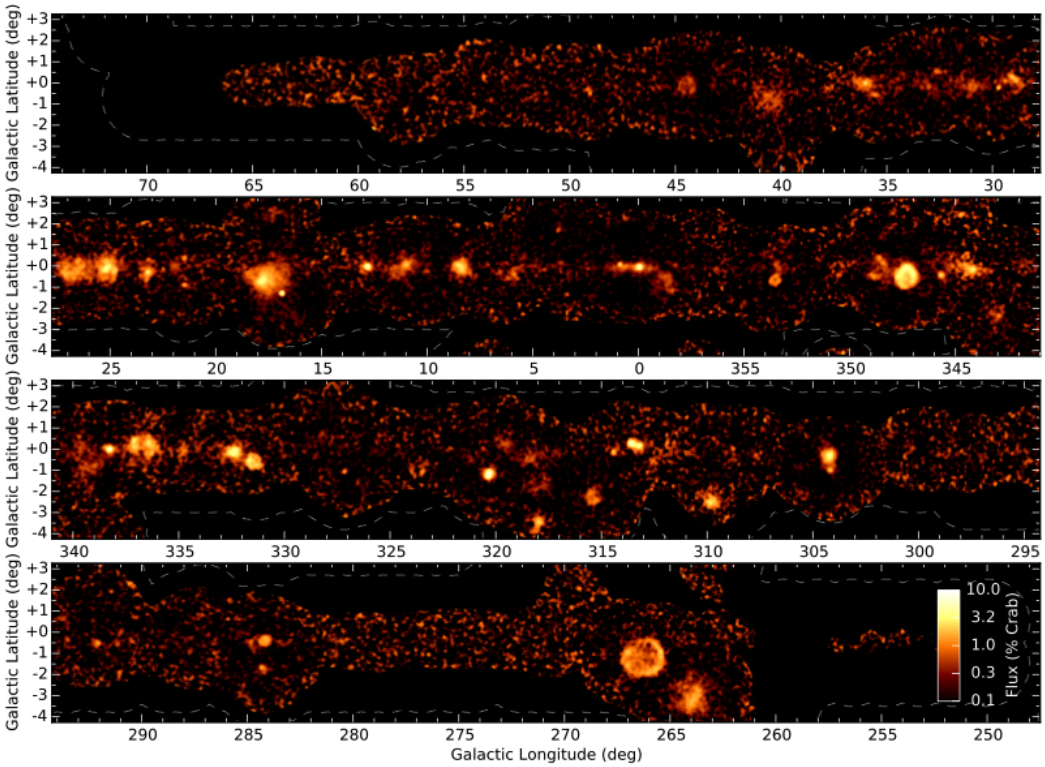

FIGURE 1.2: Integral flux above 1 TeV in units of % of the Crab nebula, the brightest VHE γ-ray source in the sky. Image taken from (H.E.S.S. Collaboration et al., 2018b).

proposed, as outlined in Aharonian (2004): by character of interactions (leptonic or hadronic, absorption or radiation) or by type of the target.

As the main subject of the data analysis projects of this thesis are SNRs, the following paragraphs will rather focus on the competing processes that are commonly advocated to explain the HE ($\sim 0.1 - 100\,\mathrm{GeV}$) and VHE ($\sim 0.1 - 100\,\mathrm{TeV}$) γ-ray emission from these objects.

1.2.1 Bremsstrahlung

When an electron undergoes acceleration in the Coulomb field of a nucleus, it emits photons by *Bremsstrahlung* (*braking radiation*).

The energy loss of an electron via Bremsstrahlung is usually characterized in terms of the so-called radiation length X_0, commonly expressed in units of $\mathrm{g\,cm^{-2}}$. X_0 is defined as *the mean distance over which a high-energy electron loses all but 1/e of its energy* (see e.g. http://pdg.lbl.gov/2016/reviews/rpp2016-rev-passage-particles-matter.pdf for a nice review); in other terms, after each radiation length, the energy of the original electron is reduced by a factor e due to Bremsstrahlung.

This kind of radiation mechanism by high energy electrons is effective until the *critical energy* E_c is reached. At E_c ionization becomes the dominant energy loss process.

As underlined in Aharonian (2004), it is interesting to note that the average energy loss-rate via Bremsstrahlung is proportional to the electron energy E_e, so that the corresponding lifetime

$$t_{br} = \frac{E_e}{-\mathrm{d}E_e/\mathrm{d}t} \simeq 4 \times 10^7 (n/1\,\mathrm{cm^{-3}})^{-1}\mathrm{yr} \tag{1.1}$$

is energy independent (n is the number density of the ambient gas). Equation (1.1) implies that Bremsstrahlung energy losses do not modify the shape of the electron spectrum, which is then reproduced by the photon one. [1]

1.2.2 Inverse Compton scattering

In the inverse Compton (IC) scattering, ultra-relativistic electrons scatter low-energy photons to high energies. The IC cross-section depends only on the product $k_0 = \omega_0\epsilon_0$, where ω_0 and ϵ_0 are the energy of the interacting photon and electron, respectively, expressed in units of $m_e c^2$ (Aharonian, 2004). For $k_0 \ll 1$, i.e., in the non-relativistic regime, it is similar to the Thomson cross-section (σ_T)

$$\sigma_{IC} \approx \sigma_T(1 - 2k_0) \tag{1.2}$$

[1] this is actually valid in the case of a power-law (PL) spectrum of electrons $\mathrm{d}N/\mathrm{d}E_e \propto E_e^{-\Gamma}$ and as long as the electron's energy is above the critical energy E_c, i.e., the electron energy losses are dominated by Bremsstrahlung.

TABLE 1.1: Mean fraction of primary energy transferred to the secondary photon in the IC scattering (ics) for different values of k_0 (adapted from Aharonian (2004))

k_0	0.01	0.1	1	10^2	10^4	10^6
$(\bar{\epsilon}_\gamma/\epsilon_0)_{ics}$	0.014	0.099	0.358	0.760	0.867	0.910

while for $k_0 \gg 1$ (ultra-relativistic regime) it decreases with k_0 following

$$\sigma_{IC} \approx \frac{3}{8}\sigma_T k_0^{-1} \ln(4k_0) \tag{1.3}$$

In the Thomson regime, the average energy gain of the upscattered photons, at the expenses of the electrons' kinetic energy, is proportional to the electrons' Lorentz factor Γ_e

$$\epsilon_\gamma \approx \omega_0 \epsilon_e^2 = \omega_0 \Gamma_e^2 \tag{1.4}$$

Equation (1.4) implies that only a fraction $k_0 \ll 1$ of the initial electron energy is transferred to the up-scattered photon; for increasing values of k_0, a higher fraction of primary energy is transferred (see Table 1.1).

Along with the decay of neutral pions, Inverse Compton scattering is one of the two processes that can potentially explain the production of VHE γ-ray photons in SNRs.

1.2.3 π_0-decay

Relativistic protons and nuclei which are accelerated by an astrophysical source can interact with the ambient gas through inelastic collisions. This leads to the production of secondary particles like pions, kaons and hyperons that subsequently decay into γ-rays. The main channel for the production of VHE radiation in this case is the decay of neutral pions (π_0), with a mean lifetime $t_{\pi_0} = 8.4 \times 10^{-17}$s. The minimum required protons' kinetic energy for the production of π_0-mesons is (Aharonian, 2004):

$$E_{th} = 2\, m_{\pi_0}\, c^2\, (1 + m_{\pi_0}/4m_p) \approx 280\,\mathrm{MeV} \tag{1.5}$$

where m_p and m_{π_0} are the proton's and the neutral pion's mass respectively.

A peculiar feature of the γ-ray spectrum from neutral pion decay is the threshold at photon energies $E_\gamma = m_\pi\, c^2/2 \approx 67.5\,\mathrm{MeV}$, often named *pion bump*. The pion bump has been exploited to claim the hadronic nature of the γ-ray emission from SNRs (e.g. in Ackermann et al. (2013) or Giordano et al. (2012)).

Figure 1.3 shows one example on how the HE and VHE emission by a supernova remnant can be modelled, in the hypothesis that the main γ-ray production mechanisms are the ones outlined above.

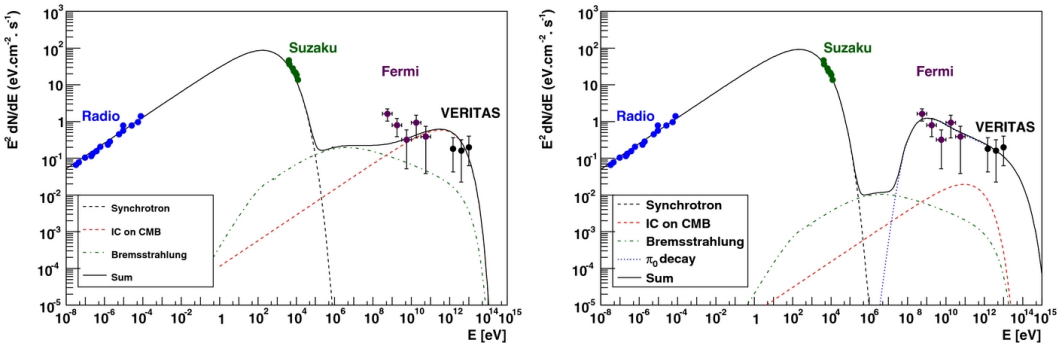

FIGURE 1.3: Broadband *spectral energy distribution* (SED) model of Tycho's SNR, in the hypothesis that the HE and VHE γ-ray emission is dominated by IC scattering (left) or π_0-decay (right). Image taken from Giordano et al. (2012).

1.3 γ-ray sources

Several objects are known to emit HE to VHE γ-rays, from our Galaxy and outside. Among the Galactic emitters, supernova remnants and pulsar wind nebulae represent the most populated source classes; extragalactic sources of particular interest in astrophysics include e.g. active galactic nuclei (AGNs) and gamma-ray bursts (GRBs).

The following section will give an overview of the main γ-ray emitters in our Galaxy, with a deeper focus on supernova remnants and how they are possibly linked to the origin of Cosmic Rays.

1.3.1 Galactic sources

Figure 1.4 shows the pie chart of the VHE γ-ray sources detected in the latest survey of the Galactic Plane with H.E.S.S. Most of them are unidentified or do not have a clear association with other catalogs.

Among the 31 clear identifications, 4 main source types can be distinguished:

- **Supernova remnants**. They are the remnants of violent star explosions known as *Supernovae*. The blast wave can accelerate particles of the surrounding medium up to very high energies (possibly up to $\sim 10^{15}$eV in our Galaxy). The VHE γ-ray emission from SNRs could stem from relativistic electrons scattering off low-energy ambient photons (*leptonic* scenario), from π_0 decay after the interaction between relativistic protons accelerated at SNRs' shock fronts and the ambient gas (*hadronic* scenario) or from a blend of these two mechanisms.

- **Pulsar Wind Nebulae**. A fast-rotating neutron star or *pulsar* steadily dissipates rotational kinetic energy according to the following equation (Gaensler and Slane, 2006):

$$\dot{E} = -\frac{dE_{rot}}{dt} = 4\pi^2 I \frac{\dot{P}}{P^3} \tag{1.6}$$

where I is the pulsar's moment of inertia, P is the pulsar's rotation period and $\dot{P} = \mathrm{d}P/\mathrm{d}t$ is its derivative with respect to time; values of $\dot{E}$ can range from $5 \times 10^{38}\mathrm{erg\,s^{-1}}$

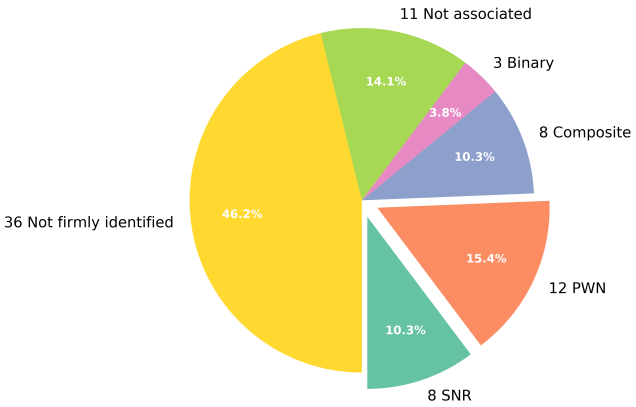

FIGURE 1.4: Pie chart of the VHE γ-ray sources from the latest survey of the Galactic Plane with H.E.S.S. Exploded from the chart, the two most populated source classes in VHE γ-rays. Reproduced from H.E.S.S. Collaboration et al. (2018b).

to $3 \times 10^{28} \mathrm{erg\,s^{-1}}$. The energy dissipated by the pulsar can power a wind of relativistic electrons and positrons, which emit synchrotron radiation in the radio and X-ray bands. The VHE γ-ray emission from PWNe can be then explained as IC scattering of the relativistic particles in the pulsar's wind, mainly off the synchrotron photons emitted at lower energies.

- **Binary systems**. They consist of a compact object (like e.g. a neutron star) and a massive star companion. The VHE γ-ray emission from these objects could be related to particles accelerated at the shock between the wind of the massive star and the one of a pulsar (Dubus, 2013).

- **Composite SNRs**. They consist of an SNR and a PWN.

Supernova remnants and the origin of Cosmic Rays

For a star in the main sequence, the hydrostatic equilibrium between the force of gravity and the pressure gradient of hot gas is maintained by the generation of nuclear energy in the star's core (Longair, 2011). This equilibrium can be kept during all the evolutionary stages of the star, until the nuclear fuel at the star's core is exhausted. When this happens, the core collapses, until some other equilibrium configuration providing pressure support is reached (e.g. *electron degeneracy pressure* in white dwarfs and *neutron degeneracy pressure* in neutron stars). More massive dead stars can also give origin to *black holes*.

In the case a neutron star or a black hole is formed, a huge amount of energy is liberated: the outer envelope of the progenitor star is ejected at high velocities, giving rise to a so-called *supernova remnant*. In other words, supernova remnants are the *leftovers* of violent stars' explosions known as *Supernovae* (SN).

The process outlined above describes the so-called *core-collapse* (CC) Supernovae. In *Type Ia* Supernovae, on the other hand, a slowly-rotating carbon-oxygen white dwarf accretes material from a companion, until the *Chandrasekhar* limit of about 1.44 solar masses ($M_\odot$[2]) is reached. At this point, the core undergoes nuclear fusion, releasing enough energy to disrupt the star in a Supernova. In both core-collapse and Type Ia Supernovae, the energy released in the explosion amounts to about $10^{51}\mathrm{erg}$ (Reynolds, 2008)[3].

One of the reasons why SNRs have been intensively studied by the astrophysical community, is that they could explain the origin of Galactic Cosmic Rays. Following the arguments proposed in Gaisser (1990), the power required to supply Galactic CRs is

$$L_{CR} = \frac{V_D \rho_E}{\tau_R} \sim 5 \times 10^{40} \mathrm{erg\,s^{-1}} \tag{1.7}$$

where V_D is the volume of the Galactic disk ($V_D = \pi R^2 d \sim \pi \left(15\,\mathrm{kpc}^2\right)(200\,\mathrm{pc}) \sim 4 \times 10^{66}\mathrm{cm}^3$), τ_R is the CRs residence time in the Galaxy ($\tau_R \sim 6 \times 10^6 \mathrm{yr}$) and ρ_E is the local energy density of CRs ($\rho_E \sim 1\,\mathrm{eV/cm}^3$). The power requirement expressed by Equation 1.7 could be satisfied by a core-collapse SN explosion every $30\,\mathrm{yr}$, ejecting $10\,M_\odot$ with a velocity of about $5 \times 10^8 \mathrm{cm\,s^{-1}}$:

$$L_{SN} \sim 3 \times 10^{42} \mathrm{erg\,s^{-1}}. \tag{1.8}$$

Given Equation 1.8, an efficiency of few percent would suffice for supernova shock waves to power all Galactic CRs.

Moreover, it can be shown (Gaisser, 1990) that particle acceleration at a strong shock wavefront (such as the ones in SN explosions) naturally leads to a power-law spectrum with index close to the one observed for local CRs.

Such mechanism is known as *first order Fermi acceleration*: a test particle crossing the SNR shock front, progressively gains energy at each encounter with the shock itself ($E \rightarrow E + \xi E$), ξ being the fractional energy gain per encounter.

Given P_{esc} the probability that the test particle escapes the acceleration region at each crossing, the number of particles N accelerated to energies greater than E can be expressed by a power-law:

$$N\,(>E) \propto \frac{1}{P_{esc}} \left(\frac{E}{E_0}\right)^{-\gamma} \tag{1.9}$$

where E_0 is the initial particle energy and $\gamma \approx P_{esc}/\xi$.

In the first order Fermi mechanism, ξ is proportional to the velocity of the shocked gas (*downstream*, u_2) relative to unshocked gas (*upstream*, u_1):

$$\xi \sim \frac{4}{3}\beta = \frac{4}{3}\frac{u1 - u2}{c} \tag{1.10}$$

[2] $1\,M_\odot \sim 2 \times 10^{30}\mathrm{kg}$

[3] In CC Supernovae, the kinetic energy of the ejected material is actually less than a percent of the energy released in neutrinos (which is about $3 \times 10^{53}\mathrm{erg}$) (Longair, 2011).

where c is the speed of light.

The index γ depends only on the compression ratio $u1/u2$:

$$\gamma = \frac{3}{u1/u2 - 1} \tag{1.11}$$

In the case of a monatomic gas, with Mach number of the flow much greater than 1 ($M = u1/c1$, being $c1$ the sound speed in the gas):

$$\gamma \approx 1 + \frac{4}{M^2} \tag{1.12}$$

In the test particle approximation (i.e., the accelerated particles do not affect the acceleration region), the index γ is universal and close to the observed one ($\gamma \approx 1.1$). In reality, due to streaming instabilities caused by the CRs themselves, the acceleration process is non-linear and can lead to spectra with non-ideal indices (e.g., $\gamma = 2$).

1.4 γ-ray detection

As outlined in the previous sections, there are a number of astrophysical sources that emit VHE γ-rays, through well defined processes that (in most of the cases) involve the interaction between accelerated particles and the ambient radiation or matter fields. The next question that needs to be answered is: how can one detect them?

Any instrument that deals with the detection of uncharged radiation must follow the same basic principle of operation: in order to be detected, the radiation must first undergo an interaction that produces at least one charged particle in the final state. For the detection of γ-rays, three main physical processes are exploited: *photoelectric effect*, *Compton scattering* and *pair production*. In all of these processes one photon either partially or completely transfers its energy to one electron of the detector's material (one suggested reading on the subject is Knoll (2000)).

For the range of energies of interest to this work, the dominant process is pair production. Pair production is a threshold process: it becomes energetically possible if the γ-ray energy exceeds twice the rest mass of the electron ($E_{th} = 1.02\,\mathrm{MeV}$). In practice, the probability of this process becomes significant only above photon energies of several MeV. In this interaction the photon is replaced by an electron-positron $e^- - e^+$ pair; the excess energy above the $1.02\,\mathrm{MeV}$ threshold goes into kinetic energy shared by the electron and the positron.

1.4.1 Satellite and ground-based experiments

Exploiting one of the interaction mechanisms mentioned above, γ-rays from an astrophysical source can be detected. Regardless of the specific kind of instrument that can be built, a very important question is *where* to place such instrument.

Figure 1.5 is of critical importance when approaching this subject: it represents the transparency of the atmosphere for radiation of different wavelengths. In the domain of γ-rays,

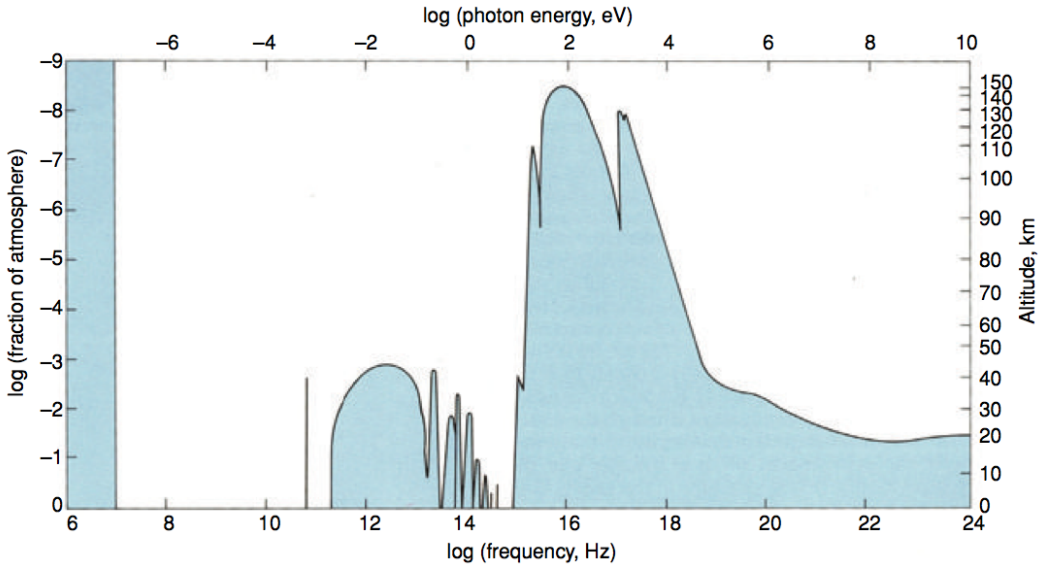

FIGURE 1.5: Transparency of the atmosphere for radiation of different wavelengths. The solid line shows the height above sea-level at which Earth's atmosphere is 50% transparent to incoming electromagnetic radiation, for radiation of different wavelengths. Figure taken from Longair (2011)

this means that one has to operate the detector in space, as Earth's atmosphere is opaque at these energies. Nowadays, there exist several satellite experiments that perform direct detection of γ-rays in space (e.g., : INTEGRAL, AGILE and Fermi-LAT (Atwood et al., 2009)). These experiments cover the energy band from tens of keV up to several tens of GeV.

In the VHE band it is unfortunately not possible (at present) to build an instrument and fly it to space to perform direct detection of γ-ray photons. This is mainly due to the very low flux at these energies, which would imply the need for either a very large effective area instrument or a very long observation time [4]. This ultimately means finding an *indirect* way of detecting them on the ground. One solution is represented by the so-called *imaging atmospheric Cherenkov telescopes* (IACTs), which will be described in the following paragraphs.

1.4.2 Imaging atmospheric Cherenkov telescopes

The main idea of an IACT is to exploit the atmosphere as a calorimeter, meaning that a γ-ray impinging on top of the atmosphere progressively degrades its energy through a series of interactions that lead to the development of a so-called *electromagnetic (e.m.) shower* (or *cascade*). The final observable of such a telescope is actually a *by-product* of this process.

A schematic representation of the development of an e.m. cascade is illustrated in Figure 1.6. A γ-ray entering the atmosphere produces an electron and a positron, having half of the initial photon energy each. Both the electron and the positron radiate in turn a Bremsstrahlung photon, further halving their energy. This bifurcation process continues until the critical energy E_c is reached, i.e. until the leptons' energy losses by Bremsstrahlung equal the losses by ionization; after this point the cascade fades out.

[4] A very simple estimation of the needed effective area for the detection of a prototype γ-ray source is proposed in Appendix A

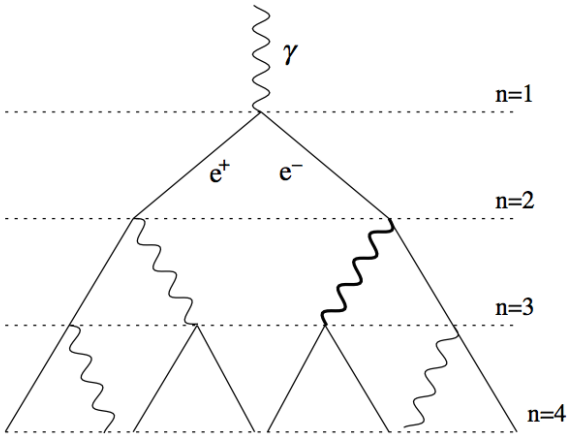

FIGURE 1.6: Schematic view of an e.m. shower. Figure taken from Matthews (2005)

The presented description is known as *Heitler's* model of an e.m. shower. From this simple representation, two very important conclusions can be derived[5]: the number of particles N_{max} that develop in an e.m shower is proportional to the initial photon energy E_i and the depth X_{max} at which the maximum size of the cascade is achieved is proportional to $\log E_i$.

Principle of operation

In the previous paragraph, the basics of the development of an e.m. shower have been outlined (a comprehensive review on the subject is given in Grieder (2010)). What is actually observed by an IACT is the *Cherenkov light* produced by the shower's charged particles.

In fact, as electrons and positrons move through the atmosphere, the air's molecules are polarized; moreover, since they travel faster than light's phase velocity (c/n, with n air's refractive index), the electromagnetic waves emitted in the molecules' relaxation process interfere constructively.

The light is then emitted in a coherent wave, with angle $\theta_c = \arccos(1/\beta\, n)$, being $\beta = v_{particle}/c$.

Due to the fact that the electrons and positrons travel with very high velocities and that air's refractive index is close to unity, the product $\beta\, n$ is approximately 1 as well. As a consequence, Cherenkov light is emitted at very small angles (about 1°) with respect to the particles' trajectory and illuminates an area on the ground of approximately $250\,\mathrm{m}$ in diameter (the so-called Cherenkov *light pool*). Figure 1.7 shows the light pool originating from a γ-ray shower with primary energy $1\,\mathrm{TeV}$.

A telescope placed on the ground within the light pool, will be able to observe the shower: the image reconstructed in the focal plane can be parametrized with an ellipse (Hillas, 1985). Parameters which are important for the image analysis are e.g., the width and length of the ellipse, the distance to the camera center and the angular offset between the source and the reconstructed direction, as outlined in Aharonian et al. (2006b). A schematic example of the imaging of the Cherenkov light from an e.m. shower is shown in figure 1.8.

[5] Appendix B contains a summary of the main results coming from Heitler's model

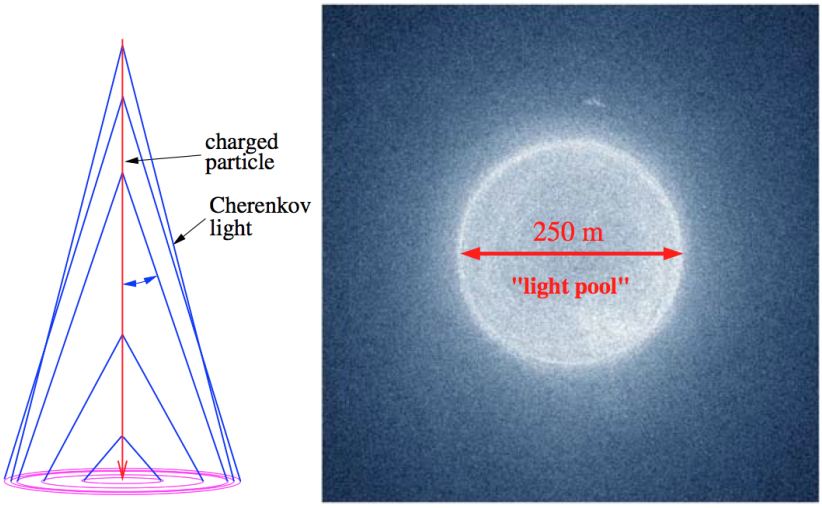

FIGURE 1.7: *Left:* Emission of Cherenkov light from a single particle travelling down the atmosphere: the angle of emission widens with decreasing altitude; most of the light is concentrated on the edge of the *light pool*, generating the so-called *Cherenkov ring* effect (see Appendix B for more details). *Right:* Cherenkov *light pool* at an height of $1800\,\mathrm{m}$ a.s.l., generated from a $1\,\mathrm{TeV}$ γ-ray-initiated e.m. cascade. Figure taken from Völk and Bernlöhr (2009)

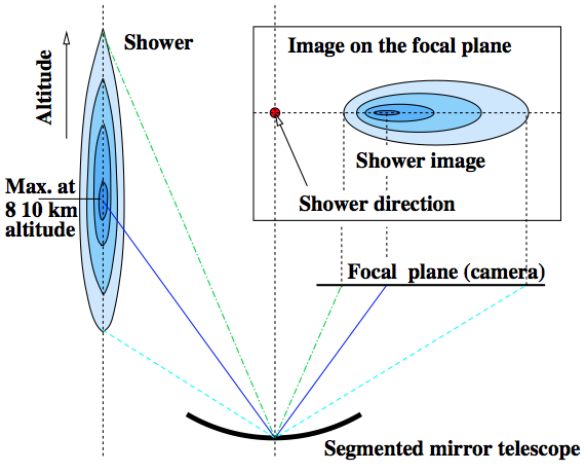

FIGURE 1.8: Imaging of a γ-ray initiated e.m. shower by a telescope. Image taken from Völk and Bernlöhr (2009)

Along with γ-rays, also charged particles (protons and heavier nuclei cosmic rays) can impinge on the atmosphere and initiate air showers. In the cascade development, secondary hadrons and leptons are produced: such a cascade consists therefore of a mixture of electromagnetic and hadronic components and has to be distinguished from a γ-ray initiated shower. This is mainly done through the analysis of the images produced in a telescope's camera: CR-induced hadronic showers have a more irregular shape and can be rejected (though not completely) by proper cuts on Hillas' parameters. [6]

Another source of noise is the light coming from background stars, usually named *Night Sky Background* (NSB). However, as most of the Cherenkov photons produced in an e.m. shower arrive on the ground within few nanoseconds, a properly chosen observation time window can be exploited to reduce such background component.

Additionally, the performance of a single telescope can be affected by muon events. If the Cherenkov light generated by a muon hits the telescope near the edge of the dish, only part of the Cherenkov ring will be imaged, possibly resembling the elliptical shape of a low-energy γ-ray shower. This problem can be solved by imposing a requirement on the *multiplicity* of telescopes observing the same event: this almost completely eliminates the contamination from muon background. Stereoscopic observations also allow to better reconstruct the shower direction and to improve the energy resolution of the system.

In the approximation that both hadronic and muonic background contaminations can be rejected by means of one of the methods mentioned above, residual background events are e.m. showers initiated by either electrons or positrons. These showers cannot be distinguished by those originating from a γ-ray on the basis of their morphological appearance in the telescopes' cameras. Such background is therefore estimated from the *sky-maps* produced off-line, in regions surrounding the source of interest, as described in Aharonian et al. (2006b).

Current and next generation of IACTs

At present, there exist three main IACTs performing indirect detection of VHE γ-rays on the ground. All of them consist of stereoscopic systems, located in different sites around the world.

MAGIC (Major Atmospheric Gamma-ray Imaging Cherenkov) consists of a system of two clone telescopes with $17\,\mathrm{m}$ diameter reflectors in the Canary Island La Palma, Spain (https://magic.mpp.mpg.de).

VERITAS (Very Energetic Radiation Imaging Telescope Array System) is an array of four $12\,\mathrm{m}$ optical reflectors, operating at the Fred Lawrence Whipple Observatory (FWLO) in southern Arizona, USA (http://veritas.sao.arizona.edu).

Both MAGIC and VERITAS conduct observations from Earth's northern hemisphere; as an example, Figure 1.9 shows the sky coverage of the VERITAS array.

[6] Image analysis based on Hillas' parameters has proven to be a robust method for the rejection of background hadronic showers and the characterization of γ-ray induced ones. Alternative approaches compare the detected images with a three-dimensional model of the shower (de Naurois and Rolland, 2009) or apply multivariate analysis techniques to improve the background rejection power (Ohm, van Eldik, and Egberts, 2009).

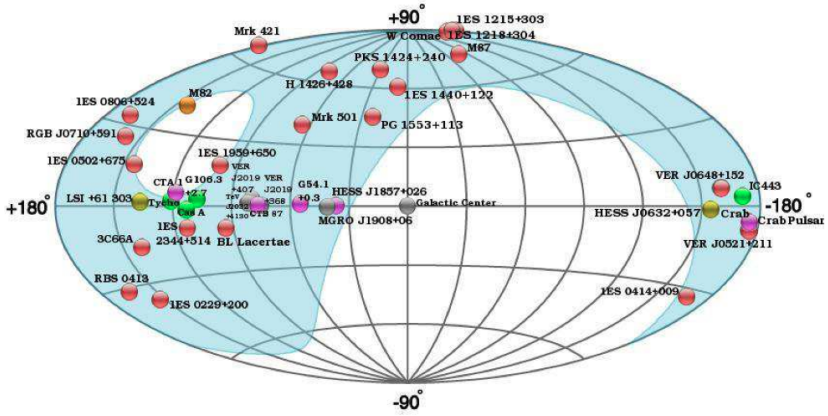

FIGURE 1.9: The VERITAS source map as of July 2011. Image taken from Holder (2011)

FIGURE 1.10: View of the full H.E.S.S. array (Credit: H.E.S.S. Collaboration, Frikkie van Greunen)

H.E.S.S. (High Energy Stereoscopic System) instead, is located in the southern hemisphere, on the Khomas Highland of Namibia at an altitude of $1800\,\mathrm{m}$ a.s.l. This results in a unique access to the inner part of our Galaxy, not visible to the other experiments. In its first phase, the H.E.S.S. array consisted of four identical $12\,\mathrm{m}$-diameter IACTs, each equipped with mirrors with a total area of $107\,\mathrm{m}^2$ and cameras of 960 photomultiplier tubes. In this configuration, the array is sensitive in the energy range from about $100\,\mathrm{GeV}$ (threshold at zenith) to some tens of TeV, with a resolution of approximately 15%. The direction of the incoming γ-rays can be reconstructed with an accuracy of less than $0.1°$; together with a large field-of-view (FOV) with $\oslash \simeq 3°$ flat ($\gtrsim 70\%$) γ-ray acceptance, this makes the instrument particularly suited for the discovery and study of extended VHE γ-ray sources in our Galaxy with typical sizes $\leq 0.5°$, such as those presented in this study (for further details on the array's performance, see Aharonian et al. (2006b)).

Starting from 2012, a much larger telescope ($614\,\mathrm{m}^2$ mirror area) is operational in the middle of the original array, lowering the energy threshold to some tens of GeV and further improving the point-source sensitivity for soft-spectrum sources (Holler et al., 2015). Figure 1.10 shows a view of the full array.

Over the years, the three above-mentioned IACTs arrays have widely demonstrated their

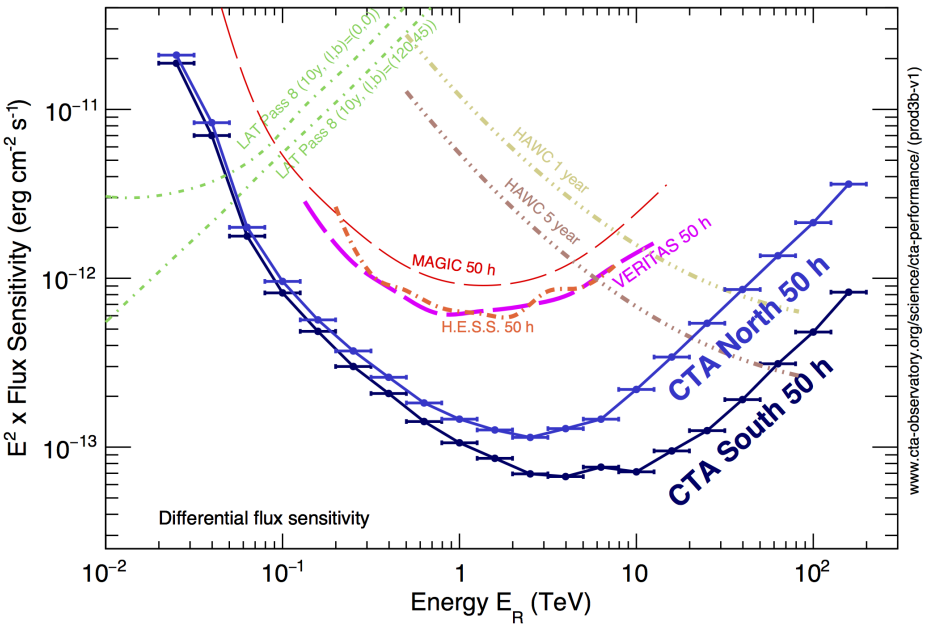

FIGURE 1.11: Differential flux sensitivity curves for the CTA northern and southern arrays, compared to the existing γ-ray instruments. The shown sensitivity is defined as the minimum flux needed by CTA to obtain a 5-standard-deviation detection of a point-like source calculated in non-overlapping logarithmic energy bins. *Source*: https://www-cta-observatory.org/science/cta-performance.

detection capabilities: more than 140 TeV sources have been detected since the first observation of the Crab Nebula above 1 TeV with the Whipple telescope, in 1989 (Weekes et al., 1989).

The next-generation IACT system, currently under development, is the Cherenkov Telescope Array (CTA). CTA will consist of two arrays of IACTs located in two sites in the northern and the southern hemisphere, respectively. With about 100 telescopes with three different dish sizes (small, medium and large) CTA aims at covering the γ-ray energy range from 20 GeV to at least 300 TeV, with an improved sensitivity of about one order of magnitude at 1 TeV with respect to the currently operational telescopes (see Figure 1.11)

In addition to the extended energy coverage and improved sensitivity, CTA aims at boosting detection area, angular resolution and field of view as well, as described in Cherenkov Telescope Array Consortium et al. (2017).

In this context, the FlashCam team has developed a camera system for the medium-size telescopes of CTA, implementing a fully-digital readout and trigger processing. Chapter 4 will present an overview of the FlashCam project, in which the University of Tübingen is involved. More specifically, the analysis of the FlashCam prototype camera calibration data will be presented.

Chapter 2

Search for new supernova remnant shells in the Galactic plane with H.E.S.S.

The discovery of Galactic supernova SNRs usually happens through surveys mapping the radio continuum emission of GeV electrons accelerated at their shock-fronts (see e.g., Green (1984) and the subsequent catalogues).

Sources are usually classified as SNR *candidates* based on their shell-like morphology in the waveband in which they are discovered; the *identification* as SNR requires an independent detection in another waveband.

The idea of the work presented in this chapter is therefore to systematically search for new SNR candidates in the sky maps produced for the latest H.E.S.S. Galactic Plane Survey (HGPS), on the basis of their morphological shell-like appearance in the VHE band. Such approach is motivated by the fact that the SNRs which are resolved in the TeV domain (such as e.g., RX J1713.7$-$3946, RX J0852.0-4622 (Vela Jr.), RCW 86, or HESS J1731$-$347) appear to have shell-like morphologies, also at lower energies, i.e. in radio and non-thermal X-rays (H.E.S.S. Collaboration, 2016d; H.E.S.S. Collaboration, 2016b; H.E.S.S. Collaboration, 2016c; H.E.S.S. Collaboration, 2011). Though this methodology is certainly not new in the astrophysical community, it was the first time, to our knowledge, in which it was successfully applied to VHE γ-ray data. The search led to the identification of three new significant shell structures (HESS J1534$-$571, HESS J1614$-$518, HESS J1912+101). One of them (HESS J1534$-$571) could be confirmed as supernova remnant, following the identification with a matching SNR candidate discovered in the radio band.

The work here presented is the result of a joint effort, from members of the H.E.S.S. Collaboration and external partners, and has already been published in H.E.S.S. Collaboration et al. (2018a). As the author of the thesis is also one of the corresponding authors of the above mentioned paper, there is overlap between the paper and the chapter's content; citations in the text taken from H.E.S.S. Collaboration et al. (2018a) are enclosed in quotation marks [1]. The author's main focus was the morphological analysis of the SNR candidates discovered in the systematic search on the Survey maps, as well as the statistical interpretation of the obtained results. The author also contributed to the definition of a possible distance estimate

[1] Credit: H.E.S.S. Collaboration, A&A, 612 (2018) A8, reproduced with permission ©ESO.

for HESS J1534−571, based on multi-wavelength information from the radio domain. Moreover, under the hypothesis of a purely-hadronic emission scenario, the author calculated the fraction of the SNR candidates explosion energy going into accelerated CR protons. Such estimates also set constraints on the possible distances at which the sources are located.

2.1 How to hunt TeV SNRs

In the VHE band there exist no spectral signatures that can help distinguishing SNRs from other types of sources. In this regime, only morphological signatures (i.e., a *shell-like* appearance) can be used. Therefore, a *significant* shell structure is considered as a sufficient criterion to classify a source as *SNR candidate*.

SNR candidates in the VHE band are considered *confirmed SNRs* only if a matching identification in a different waveband is found.

This identification approach has two issues:

- the choice of the region of interest (ROI) where the morphological analysis has to be performed. This issue is related to the fact that it is not always clear how to discern contributions from all the sources in the FOV;
- the appropriate choice of the *null-hypothesis* to which the *shellness* of the source of interest has to be compared.

The first issue can be addressed by adequately modeling the emission from all the sources that appear in the FOV (though not always straightforward, as for example in the case of HESS J1614−518, see subsection 2.1.3).

The second issue stems from the fact that the goodness of the fit cannot be considered as stand-alone criterion for a shell-like source morphology. "Instead, the shell fit quality is compared to a fit result of a simpler default model (referred to as *null hypothesis*) that is chosen to represent a typical Galactic VHE source different from known SNR shell sources. The most abundant identified Galactic source class of this character comprises PWNe, which are usually well described by a centrally peaked morphology. As a default model, a two-dimensional symmetric Gaussian with variable width was chosen, which represents typical PWNe as well as the majority of other known Galactic H.E.S.S. sources (including point-like sources)." (H.E.S.S. Collaboration et al., 2018a)

2.1.1 Shell or not? Comparing non-nested models

"To examine the shell-type appearance of the TeV emission region, a shell morphological model is fit to the data. The model is a three-dimensional spherical shell, homogeneously

emitting between $R_{\rm in}$ and $R_{\rm out}$ and projected onto the sky. The emissivity in Cartesian sky coordinates (x, y) is then

$$M(r) = A \times \begin{cases} \sqrt{R_{\rm out}^2 - r^2} - \sqrt{R_{\rm in}^2 - r^2}, & r < R_{\rm in}, \\ \sqrt{R_{\rm out}^2 - r^2}, & R_{\rm in} < r < R_{\rm out}, \\ 0, & r > R_{\rm out}, \end{cases} \tag{2.1}$$

where $r^2 = (x - x_0)^2 + (y - y_0)^2$ is the (squared) distance to the source centre at (x_0, y_0). Before fitting, the model is convolved numerically with the point spread function (psf) of the H.E.S.S. data set under study, which is derived from Monte Carlo simulations taking the configuration of the array and the distribution of zenith angles into account (Aharonian et al., 2006b). The fitted parameters are $A, x_0, y_0, R_{\rm in}$, and $R_{\rm out}$. During the search and identification procedure, no attempt is made to model deviations from this assumed emission profile, for example azimuthal variations such as the ones that are known from the bipolar morphology of the TeV-emitting SNR of SN 1006 (Acero et al., 2010)."(H.E.S.S. Collaboration et al., 2018a)

As mentioned above, the chosen null-hypothesis model is a two-dimensional symmetric Gaussian with variable width. The Gaussian model is convolved analytically with the H.E.S.S. psf before fitting[2]. The emissivity in Cartesian sky coordinates (x, y) is then

$$M(r) = A \frac{s_1 + s_2 + s_3}{N} \tag{2.2}$$

where $s_{i=1,2,3} = \alpha_i \sigma_i^2 \frac{1}{2\pi(\sigma_i^2+\sigma^2)} e^{-\frac{1}{2}\frac{r^2}{(\sigma_i^2+\sigma^2)}}$, $N = \sum_i \alpha_i \sigma_i^2$, σ = sigma of the fitted Gaussian, σ_i = sigma of the $i-th$ Gaussian of the psf function, α_i = amplitude of the $i-th$ Gaussian of the psf function ($\alpha_1 = 1$, while $\alpha_{2,3}$ are the amplitudes relative to α_1) . The fitted parameters are A, x_0, y_0 and σ.

Figure 2.1 shows a comparison between the 2-dimensional images of a shell and a Gaussian model respectively, constructed with arbitrary parameters. Starting from these images, the *radial profiles* of such models have been built (Figure 2.2), showing the integrated emission from concentric equispaced annuli as a function of the distance from the centre of the picture. As it can be seen, a shell-like source will have a shallower emission in the centre, while peaking towards the inner radius; an opposite behaviour is found for a Gaussian-shaped source.

The employed fitting routines are based on *Sherpa*, the CIAO modeling and fitting application (http://cxc.harvard.edu/sherpa/index.html). Assuming that the counts in the maps are sampled from the Poisson distribution, a likelihood function can be defined in order to assess the quality of the fit

$$\mathcal{L} = \prod_i \frac{M_i^{D_i}}{D_i!} exp(-M_i) \tag{2.3}$$

[2]The H.E.S.S. psf is represented here to sufficient accuracy by a sum of three Gaussians (H.E.S.S. Collaboration et al., 2018b, Sect. 4.3)

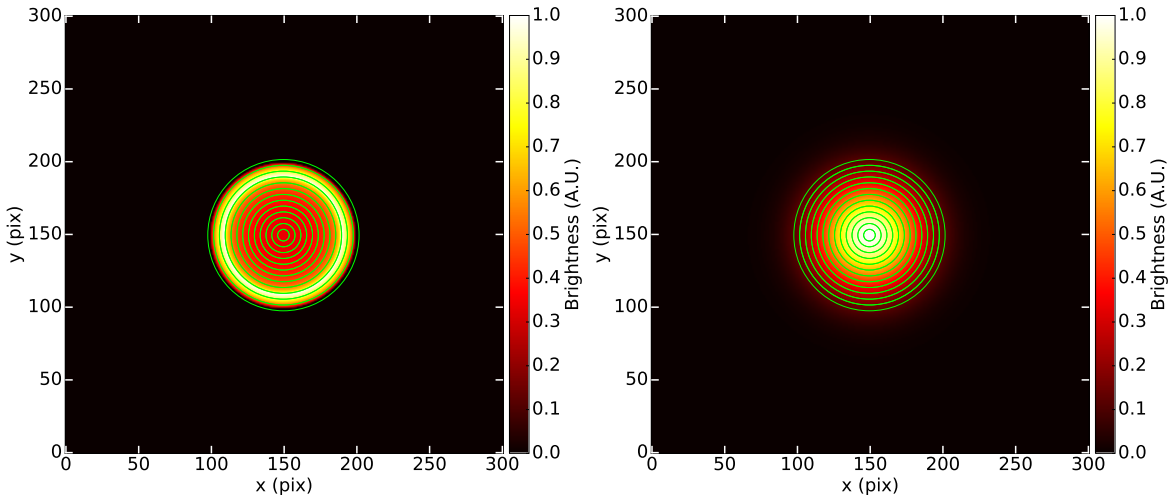

FIGURE 2.1: *Left*: Example of a shell model as described by Equation 2.1 on a map in pixel coordinates, with $R_{in} = 40\,\mathrm{pix}, R_{out} = 50\,\mathrm{pix}$. The colorbar indicates the brightness of the object in arbitrary units. The green annuli have been used to derive the radial profile shown in Figure 2.2; the spacing between each of them is 4 pixels. *Right*: Example of a Gaussian model ($\sigma = 25\,\mathrm{pix}$), used as null-hypothesis morphology to describe the sources of interest. Overlaid in green the annuli that have been used to derive the radial profile shown in Figure 2.2, as for the shell model.

where $M_i = S_i + B_i$ is the sum of the amplitudes for the source and the background model, in the $i-th$ bin, while D_i is the number of observed counts. In the performed morphological analysis, a slightly different function was used, namely the *cstat* implementation of the Cash statistics available in *Sherpa* (http://cxc.harvard.edu/sherpa/statistics/) and here reported:

$$\mathcal{C} = 2\sum_i [M_i - D_i + D_i(\ln D_i - \ln M_i)] \tag{2.4}$$

"Adopting the assumption that the chosen morphological models for shell (H_1) and null hypothesis (H_0) represent the true TeV source populations sufficiently well, the improvement in the fit quality (i.e., the likelihood that the shell model describes the given data set better than the Gaussian model) can be interpreted in a numerically meaningful way"(H.E.S.S. Collaboration et al., 2018a). Usually, following Wilk's theorem, it is assumed that $\Delta\mathcal{C}$ is distributed as a χ^2 with number of degrees of freedom (d.o.f.) equal to the difference in d.o.f. between the tested models (in this case, $\Delta(d.o.f.) = d.o.f._{shell} - d.o.f._{Gauss} = 1$). "However, there is the (purely analytical) issue that the two compared models are *non-nested*, i.e., one cannot smoothly go from H_0 to H_1 with a continuous variation of the parameters"(H.E.S.S. Collaboration et al., 2018a). More precisely, following Eadie, Drijard, and James (1971), two hypothesis belong to a *continuous family* when their probability density functions have the same analytical form; the only difference lies in the specification of the

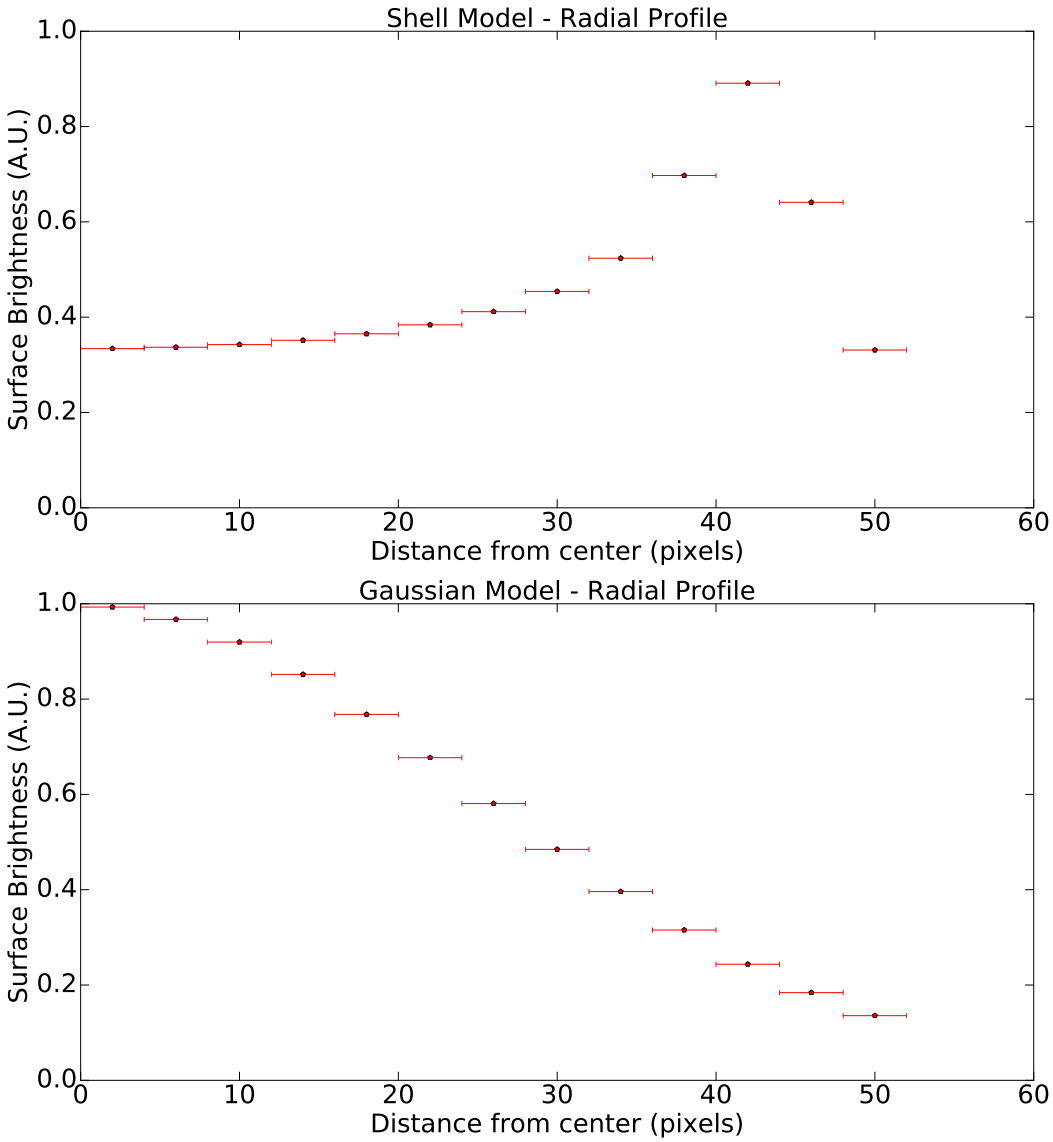

FIGURE 2.2: *Top*: Radial profile of the shell model presented in Figure 2.1. The projected emission peaks towards the inner radius $R_{\rm in}$. *Bottom*: Radial profile of the Gaussian model presented in Figure 2.1; contrary to the shell model, the emission is centrally-peaked.

parameter space, as for example:

$$\begin{aligned} H_0 &: f\left(\mathbf{X}|\theta\right) \text{with } \theta < \theta_0 \text{ is valid} \\ H_1 &: f\left(\mathbf{X}|\theta\right) \text{with } \theta > \theta_1 \text{ is valid} \end{aligned} \tag{2.5}$$

On the other hand, two hypothesis belong to *separate families* when they cannot be deduced from each other by a continuous variation of the parameters.

In the latter case, the above mentioned assumption on $\Delta\mathcal{C}$ does not hold true (Protassov et al., 2002). "One way to overcome this problem is to adopt the *Akaike Information Criterion*

(AIC) (Akaike, 1974). For a given model, AIC is computed as

$$\mathrm{AIC} = 2k - 2\ln\left(\mathcal{L}_{\mathrm{ML}}\right) \tag{2.6}$$

where k is the number of model parameters and $\mathcal{L}_{\mathrm{ML}}$ is the maximum likelihood value for that model. Testing a set of models on the same data set,

$$\mathcal{L}_{\mathrm{AIC},i} = C \cdot \exp\left(-\frac{\mathrm{AIC}_i - \mathrm{AIC}_{\mathrm{min}}}{2}\right) \tag{2.7}$$

gives a likelihood or relative strength of model i with respect to the best available model, i.e., the one found to have the minimum AIC ($\mathrm{AIC}_{\mathrm{min}}$) (Burnham and Anderson, 2002).

In order to quantify if and how $\mathcal{L}_{\mathrm{AIC},H_0}$ translates into a probability that the improvement obtained with the shell fit over the Gaussian model is due to statistical fluctuations, a limited number of simulations has been performed on HESS J1534−571 (the source with the lowest shell over Gaussian likelihood, see Table 2.5)"(H.E.S.S. Collaboration et al., 2018a). Using as an input the Gaussian best-fit parameters of HESS J1534−571, a Gaussian source has been iteratively simulated. At each iteration, the simulated source has been fit both with a Gaussian and a shell model; the test statistics and AIC for each model (as reported in Eq. 2.4 and 2.6, respectively) have been calculated and stored in two different arrays. For each element of the array, the test statistics difference $\Delta\mathcal{C} = \mathcal{C}_{\mathrm{Gauss}} - \mathcal{C}_{\mathrm{shell}}$ and the difference in AICs ($\Delta\mathrm{AIC} = \mathrm{AIC}_{\mathrm{shell}} - \mathrm{AIC}_{\mathrm{Gauss}}$) has been computed, along with the respective probabilities (in the hypothesis that $\Delta\mathcal{C}$ is distributed as $\chi^2\,(1)$ and following 2.7 for $\Delta\mathrm{AIC}$). Given three significance thresholds $(th_0,\ th_1,\ th_2) = (90\%,\ 95\%,\ 99\%)$, the number of false-positives (type I errors), i.e., simulated Gaussians misinterpreted as shells, has been calculated by counting the cases in which $p\,(\Delta\mathcal{C})$ (respectively $\mathcal{L}_{AIC}$) is smaller than $1 - th_i$. With a similar procedure (but using a simulated shell with HESS J1534−571 best-fit parameters), the number of false-negatives (type II errors - i.e., non-detected shells) has been computed.

"As shown in Figure 2.3, the number of type I errors, behaves roughly as a null-hypothesis probability in the relevant $90\,\%$ to $99\,\%$ probability range with C (Eq. 2.7) set to 1, whereas the application of Wilk's theorem produces too many false positives compared to expectation. In turn, $\sim$10 % false-negative (type II) errors, i.e., non-detected shells, are estimated when using $\mathcal{L}_{\mathrm{AIC}}$ for a $99\,\%$ significance threshold, ensuring sufficient sensitivity of the chosen method. In conclusion, the AIC is found to be more reliable even if less sensitive. Table 2.5 also lists $\mathcal{L}_{\mathrm{AIC},H_0}$ for HESS J1614−465 and HESS J1912+101. While the correspondence to a chance probability has not been verified for these two sources with analogous simulations, the resulting values ensure to sufficient degree of certainty a low probability of a chance identification as a shell for these two sources as well"(H.E.S.S. Collaboration et al., 2018a).

2.1.2 The HGPS data set and the systematic grid search

The data set of the latest survey of the Galactic Plane with H.E.S.S. (HGPS) consists of roughly 2700 hours of observations (after quality selection) taken between 2004 and 2013.

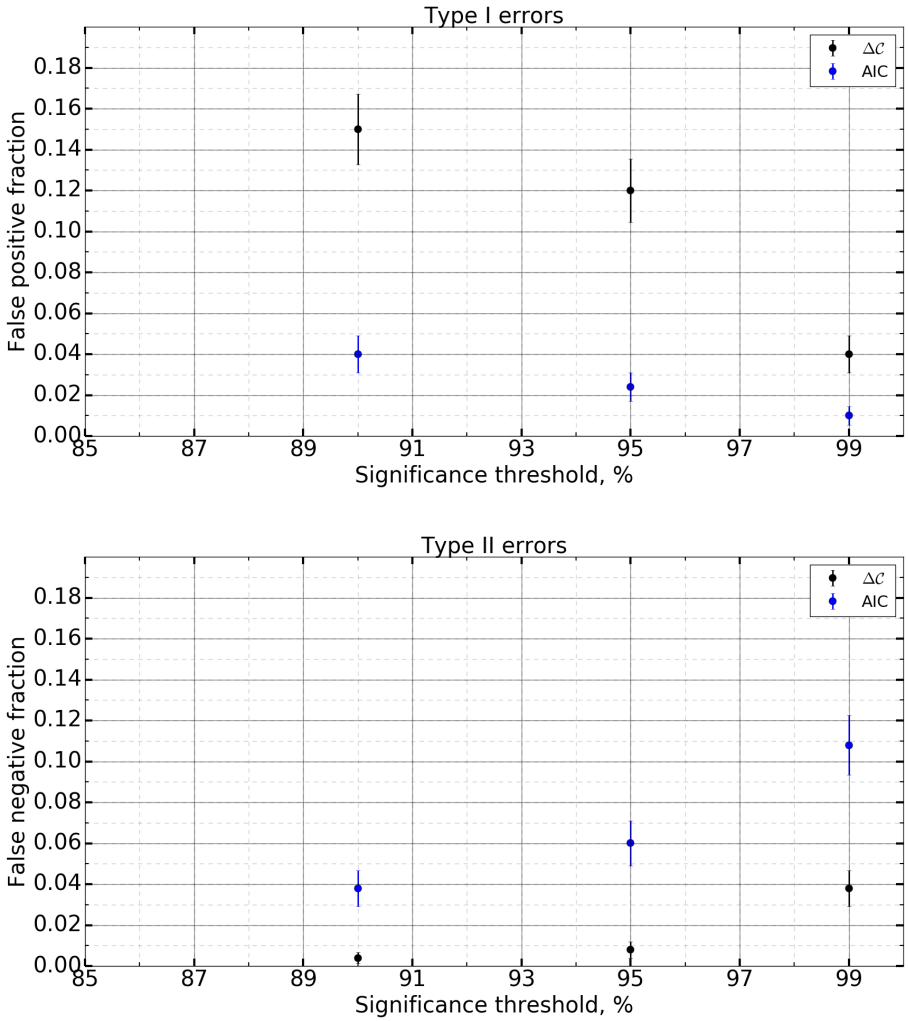

FIGURE 2.3: *Top*: False positive fraction (*true* Gaussians misinterpreted as shells) obtained when applying Wilk's theorem (labeled as $\Delta\mathcal{C}$) and AIC. *Bottom*: False negative fraction (non-detected *true* shells) obtained when applying Wilk's theorem (labeled as $\Delta\mathcal{C}$) and AIC. The *true* Gaussians and shells have been simulated using HESSJ1534-571 best-fit parameters. Results by R. Terrier

It covers the longitude range between $l = 250°$ and $l = 65°$ (including the Galactic center), and the latitudes $|b| \lesssim 3.5°$. Many sources falling into the HGPS have also been observed individually over the survey time span (e.g. H.E.S.S. Collaboration, 2011; H.E.S.S. Collaboration, 2016d; H.E.S.S. Collaboration et al., 2018b; H.E.S.S. Collaboration, 2016a), thus resulting in a non-homogeneous sensitivity across the data set: the average value for point sources in the core survey region is $\lesssim 1.5\%$ of the Crab Nebula flux above $1\,\mathrm{TeV}$ (H.E.S.S. Collaboration et al., 2018b).

For the work presented in this chapter, "only sky map products of the HGPS have been used, namely"(H.E.S.S. Collaboration et al., 2018a):

- a sky map of γ-ray event candidates after image-shape based background rejection
- a sky map of estimated remaining background level

TABLE 2.1: List of tested H_0 and H_1 parameters for the grid search; $w = R_{\rm out} - R_{\rm in}$ is the shell width. Taken from H.E.S.S. Collaboration et al. (2018a).

Shell (H_1) parameters	
$R_{\rm in}$	$0.1°$, $0.2°$, $0.3°$, $0.4°$, $0.5°$, $0.6°$, $0.7°$, $0.8°$
w	$10^{-5} \times R_{\rm in}$, $0.1 \times R_{\rm in}$, $0.2 \times R_{\rm in}$
Gaussian (H_0) parameters	
σ	$0°$, $0.05°$, $0.1°$, $0.2°$, $0.4°$

- an exposure sky map

As a first step, the HGPS area has been divided into a grid of sky coordinates test positions, with equal spacing of $0.02° \times 0.02°$. At each position, a shell (H_1) and a Gaussian model (H_0) have been tested; in order to be computationally efficient, only a limited number of parameters for each of the models have been used, as listed in Table 2.1. The parameters have been chosen so that the known TeV SNR shells are well represented by such models.

For each point of the grid, for each of the shells with the parameters listed in Table 2.1, the test statistics difference between the shell and a pure background model has been calculated:

$$\Delta\mathrm{TS}_{shell} = -\left(\mathcal{C}_{shell} - \mathcal{C}_{bkg}\right) \tag{2.8}$$

with $\mathcal{C}$ defined according to Eq. 2.4. The same has been done for each of the Gaussian models:

$$\Delta\mathrm{TS}_{Gauss} = -\left(\mathcal{C}_{Gauss} - \mathcal{C}_{bkg}\right) \tag{2.9}$$

Afterwards, the difference between the shell and the Gaussian with the highest ΔTS across all parametrized scales has been derived and stored into a sky map:

$$\Delta\mathrm{TS}_{max} = \Delta\mathrm{TS}_{max,shell} - \Delta\mathrm{TS}_{max,Gauss} \tag{2.10}$$

"In such a map, the signature of a shell candidate is an isolated peak surrounded by a broad ring-like artifact"[3], as shown in Figure 2.6. In order to illustrate how the search works, a simplified test has been constructed by the author and presented in the following. Figure 2.4 (left) shows a symmetric 2-dimensional Gaussian source with $\sigma = 20\,\mathrm{pix}$ and peak amplitude arbitrarily fixed to 1. The source is built on top of a constant, flat background with amplitude 1 as well.

At the fixed coordinate $y = 150\,\mathrm{pix}$, a 1-dimensional grid with equal spacing of $1\,\mathrm{pix}$ has been built, ranging from $x = 50\,\mathrm{pix}$ to $x = 150\,\mathrm{pix}$; in Figure 2.4, only the grid centers every $10\,\mathrm{pix}$ are highlighted in green for clarity. At each grid test position, a background+Gaussian model with fixed σ ($\sigma = 5, 10, 20, 40\,\mathrm{pix}$) has been tested against a pure background model

[3] "For this first-step map, a test statistics difference has been used for simplicity, while AIC has been used to derive final likelihood values, in the source-by-source analysis"H.E.S.S. Collaboration et al. (2018a).

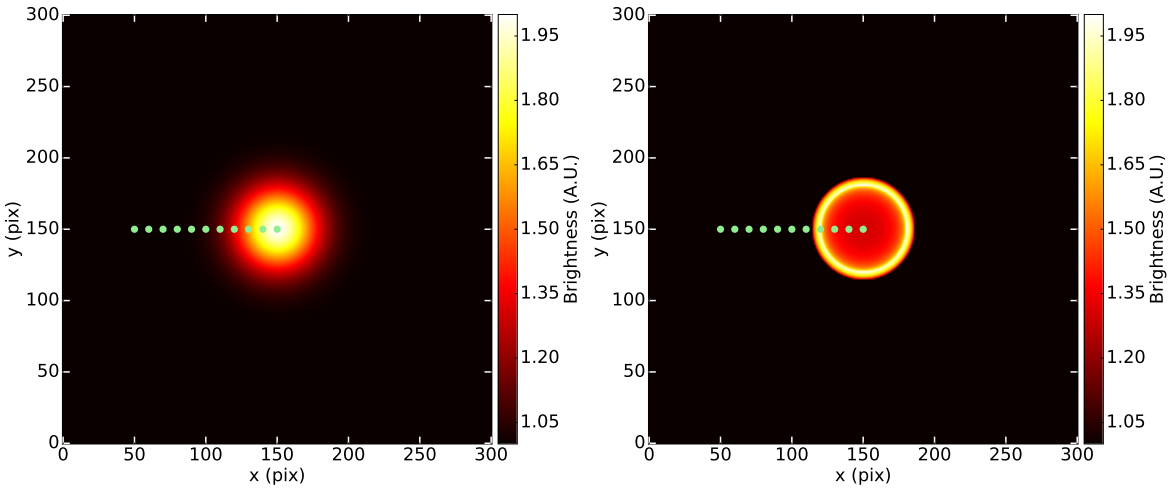

FIGURE 2.4: *Left:* Simulated Gaussian source ($\sigma = 20\,\mathrm{pix}$); the dots highlight the grid points at which a shell model has been tested against a Gaussian model. *Right:* Simulated shell source ($R_{in} = 30\,\mathrm{pix}$); the dots highlight the grid points on which a shell model has been tested against a Gaussian model.

and the maximum difference in test statistics across all σ, as defined in 2.9, has been calculated. The only free parameters are the background and Gaussian model amplitudes. At the same test positions, a background+shell model with $R_{in} = 10, 20, ..., 80\,\mathrm{pix}$ and variable width ($w = 10^{-5} \times R_{in}, 0.1 \times R_{in}, 0.2 \times R_{in}$) has been tested, and the maximum $\Delta\mathrm{TS}$ across all radii and widths, with respect to a pure background model, has been calculated. Afterwards, the difference $\Delta\mathrm{TS}_{max}$ for each grid point has been obtained, according to Equation 2.10. The same procedure has been applied to a shell source with $R_{in} = 30\,\mathrm{pix}$ and width $w = 0.2 \times R_{in}$, shown in Figure 2.4 (right). Figure 2.5 shows $\Delta\mathrm{TS}_{max}$ as a function of the tested positions, for both the Gaussian and shell source. As it can be observed, when a true Gaussian source is present, $\Delta\mathrm{TS}_{max}$ towards the center becomes eventually negative, because $\Delta\mathrm{TS}_{max,shell} < \Delta\mathrm{TS}_{max,Gauss}$. In the case a shell-like source is tested, instead, the TS difference in the center is positive, as the shell model provides a better description of the emission. In conclusion, the shell model assumption creates ring-like artifacts around bright sources, but shell candidates should show peaks within such rings.

Using this method, all the known TeV SNR shells falling into the HGPS region (RX J1713.7−3946, RX J0852.0−4622, HESS J1731−347, and RCW 86) have been re-identified with high confidence. In addition to those, four significant shell structures have been found. Three of them are coincident with already known H.E.S.S. sources: HESS J1023−577 (Aharonian et al., 2007a), HESS J1614−465 (Aharonian et al., 2006c) and HESS J1912+101 (Aharonian et al., 2008a). The results from the grid search are reported in Table 2.2 and 2.3 for the known and *new* TeV SNR shells respectively.

A fourth source at Galactic coordinates $l \sim 323.7°$, $b \sim -1.02°$ has not been published before. It was discovered as *new* source during the latest HGPS: the $\mathrm{TS}_{\mathrm{diff}}$ between a Gaussian and a background-only model for the source is 39, thus above the survey detection threshold $\mathrm{TS}_{\mathrm{diff}} = 30$. The newly discovered source is named HESS J1534−571, corresponding to the centre coordinates of the fitted shell model.

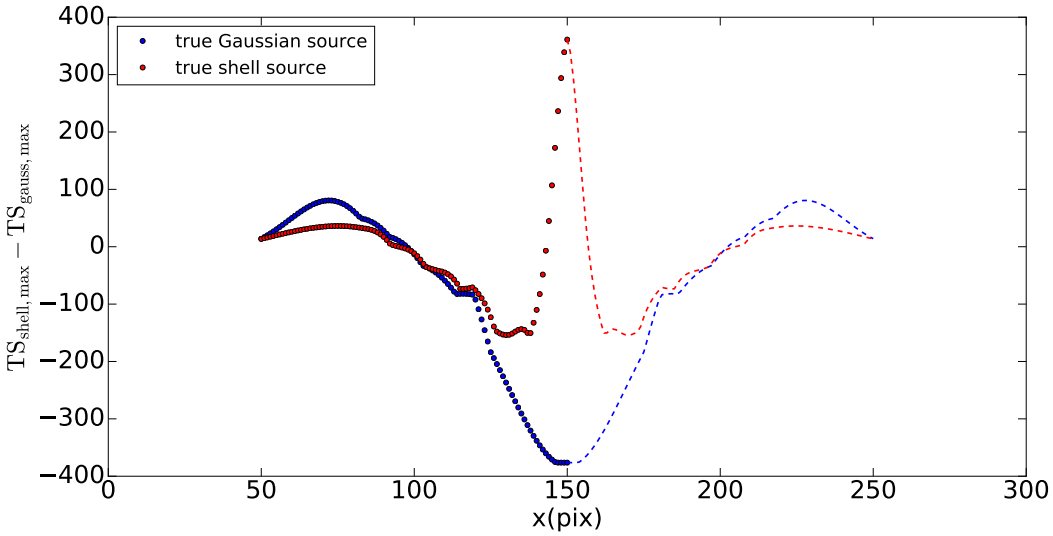

FIGURE 2.5: $\Delta TS_{max} = \Delta TS_{max,shell} - \Delta TS_{max,Gauss}$, as a function of the tested position along x, in the case a true Gaussian (blue dots) or a true shell (red dots) are tested. Exploiting the radial symmetry of the simulated sources, the models have been tested only up to the source center. The dashed lines mirror the obtained results around position x=150.

Though ensuring a relatively unbiased search strategy, the grid set-up has several limitations. First, the limited number of tested models, both concerning the Gaussian null-hypothesis and the shell morphology. Second, the restriction of keeping the same centroid; in both cases, this could result in a non-optimal H_0 fit, thus leading to an overestimation of the shell-over-Gaussian significance for a given test position.

In order to overcome these issues, a source-by-source refined analysis as described in Section 2.1.3 has been performed. After this individual re-analysis, one of the sources (HESS J1023−577) has been removed from the list of TeV SNR candidates, as its morphology has been found to be compatible with a centre-filled shell (i.e., $R_{\rm in} \simeq 0$).

2.1.3 Individual source analysis and main results

Data selection and analysis

Following the identification of the new SNR candidates on the HGPS data-set, final shell parameters and likelihoods have been computed on a source-by-source basis using the method described in the following subsection. The data-sets for the individual source analysis have been processed with the same criteria of the HGPS (in terms of calibration of the raw-data, γ-ray reconstruction and background rejection algorithms). However, some differences due to optimization with respect to a survey are present. For example, the data used to produce the sky maps have been selected to ensure a flat exposure at and around the sources of interest; for the spectral analysis, the choice of the background control regions has been optimized for each of the sources The dataset used for this work is slightly more extended than the Survey one, and includes the observation runs[4] taken between April 2004 and May 2013,

[4]Each observation run consists of a sky-tracking observation lasting typically 28 min

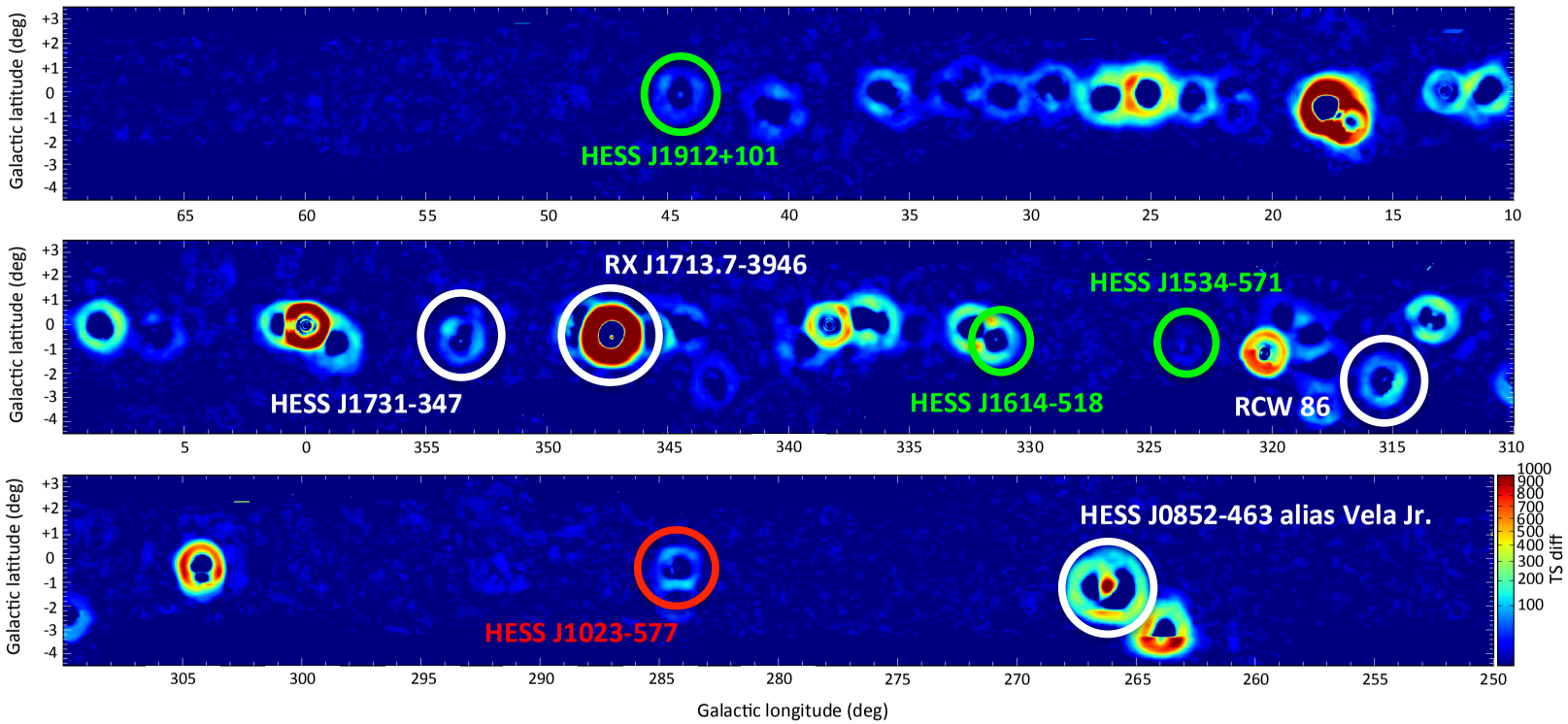

FIGURE 2.6: Test statistics (TS) difference map resulting from the grid search algorithm. At each grid position, the TS difference between the best-fitting shell and the best-fitting Gaussian with the parameters listed in Table 2.1 is filled; the footprint of a shell candidate is an isolated peak surrounded by a broad ring-like artefact. The *white* circles enclose the TeV SNR shells already known before this work, while the *green* ones highlight three of the four SNR shell candidates that show a high TS difference (namely, HESS J1534−571, HESS J1614−518, HESS J1912+101). The *red* circle encloses the fourth SNR shell candidate, HESS J1023−375. After an individual re-analysis its morphology has been found to be compatible with a centre-filled shell (i.e., $R_{in} \simeq 0$). For this reason, it has been removed from the list of TeV SNR candidates. Map by C. Deil and A. Donath (MPIK).

TABLE 2.2: Results from the grid search for the known TeV SNR shells. [a]: Test statistics difference between the best-fitting shell and the best-fitting Gaussian ($TS_{diff,max}$). [b]: (l_0, b_0) are the grid position coordinates (Galactic longitude and latitude respectively) at which $TS_{diff,max}$ has been found. [c]: Sigma of the best-fitting Gaussian at (l_0, b_0) . [d]: Inner radius of the best fitting shell at (l_0, b_0). [e]: Width of the best fitting shell. at (l_0, b_0). Results by C. Deil and A. Donath (MPIK).

.

	Vela Jr.	RCW 86	RX J1713.7−3946	HESS J1731−347
$TS_{diff,max}$ [a]	1778	42	946	68
l_0 [b]	266.21°	315.38°	347.29°	353.56°
b_0 [b]	−1.17°	−2.27°	−0.53°	−0.68°
σ [c]	0.4°	0.2°	0.4°	0.2°
R_{in} [c]	0.8°	0.3°	0.4°	0.2°
w [d]	$0.2 \times R_{in}$	$0.2 \times R_{in}$	$10^{-5} \times R_{in}$	$0.2 \times R_{in}$

TABLE 2.3: Results from the grid search for the *new* TeV SNR shells. [a]: Test statistics difference between the best-fitting shell and the best-fitting Gaussian ($TS_{diff,max}$). [b]: (l_0, b_0) are the grid position coordinates (Galactic longitude and latitude respectively) at which $TS_{diff,max}$ has been found. [c]: Sigma of the best-fitting Gaussian at (l_0, b_0) . [d]: Inner radius of the best fitting shell at (l_0, b_0). [e]: Width of the best fitting shell. at (l_0, b_0). Results by C. Deil and A. Donath (MPIK).

	HESS J1023−577	HESS J1534−571	HESS J1614−518	HESS J1912+101
$TS_{diff,max}$ [a]	24	23	57	50
l_0 [b]	284.19°	323.72°	331.41°	44.45°
b_0 [b]	−0.40°	−0.90°	−0.63°	−0.12°
σ [c]	0.2°	0.2°	0.2°	0.4°
R_{in} [c]	0.2°	0.3°	0.3°	0.3°
w [d]	$0.2 \times R_{in}$	$10^{-5} \times R_{in}$	$0.2 \times R_{in}$	$10^{-5} \times R_{in}$

calibrated using standard H.E.S.S. procedures (Bolz, 2004; Aharonian et al., 2006b). The run selection for each of the sources is based on *quality cuts*, that aim at checking the sanity of hardware-related and atmospheric-related quantities (Aharonian et al., 2006b; Hahn et al., 2014). For example, the effective area lookup tables used in the spectral analysis of a source rely on atmospheric models for the H.E.S.S. site; such models cannot be applied in bad weather conditions (i.e.,: in the presence of clouds or aerosols affecting the transparency of the atmosphere to the Cherenkov light). On the other hand, when aiming at the detection of a source (where no spectrum extraction is needed and the error is dominated by statistics) such quality standard is not required. For this reason, two different sets of cuts were adopted for the morphological and spectral analysis, respectively. For the morphological analysis, runs with a maximum offset of 3° from the center of the source under investigation were selected; the offset was reduced to 1.5° for the spectra extraction. The source positions for the run selection were either taken from previous H.E.S.S. publications (in the case of HESS J1614−518 (Aharonian et al., 2006c) and HESS J1912+101 (Aharonian et al., 2008a)) or from the HGPS pipeline (in the case of HESS J1534−571). Table 2.4 shows the resulting

TABLE 2.4: Acceptance-corrected observation times used in the source-by-source morphological (*Sky maps*) and spectral (*Energy spectra*) analysis. Table taken from H.E.S.S. Collaboration et al. (2018a)

Source	Sky maps	Energy spectra
HESS J1534−571	61.8 h	25.4 h
HESS J1614−518	34.2 h	10.0 h
HESS J1912+101	121.1 h	43.2 h

observation times available for each source, acceptance-corrected (i.e., corrected for dead time, variations of the acceptance depending on the off-axis angle in the field of view and normalized to a standard offset of $0.5°$).

The event reconstruction from the recorded camera images starts with a cleaning procedure, as described in Aharonian et al. (2006b). This procedure aims at selecting only the pixels containing Cherenkov light and rejecting the ones mainly affected by electronic noise and *Night Sky Background* (NSB). A threshold on the number of photo-electrons (p.e.) detected by a given pixel and its neighbors is set: for this study a 5 p.e.-10 p.e. cut is used, i.e., a given pixel is required to be above a 5 p.e. threshold with at least one neighbor above 10 p.e. Afterwards, the camera image is parametrized using Hillas' description (see Subsection 1.4.2); a boosted decision tree method (Ohm, van Eldik, and Egberts, 2009) is then used to select γ-ray-like events and discard hadronic ones. The reconstruction is performed only on events whose images are contained in at least two telescopes, in order to improve both angular and energy resolution. After the γ-hadron separation process, some background at each sky-pixel is still present; such background can be attributed to hadronic, leptonic and possibly diffused γ-ray emission. For the sky-maps used in the morphological study described in the following subsection, the residual background is estimated from a ring around the pixel position (Berge, Funk, and Hinton, 2007), with the application of an adaptive algorithm to optimize the size of the ring (H.E.S.S. Collaboration et al., 2018b). "All results have been cross-checked using an independent calibration and simulation framework, combined with an alternative reconstruction algorithm (de Naurois and Rolland, 2009)"(H.E.S.S. Collaboration et al., 2018a). In this technique, the distribution of the Cherenkov light in a shower is derived from Monte Carlo simulations and parametrized in order to obtain an analytical description of the shower itself; additionally, the noise induced in each pixel by NSB is modeled as well. In this way, the recorded images can be directly compared to the model and the shower parameters obtained after a minimization procedure, without the need for a dedicated image cleaning procedure.

Morphological analysis

Morphological fits have been performed, using a forward folding technique, on uncorrelated *on-counts*[5] sky maps with $5° \times 5°$ size and with $0.01° \times 0.01°$ bin size. The model fit

[5] i.e., maps of γ-candidates after γ-hadron separation, not background-subtracted or flat-fielded

function On_i is constructed as

$$\mathrm{On}_i = A \times \mathrm{Bkg}_i + (\mathrm{psf} * M_i) \times N_{\mathrm{ref},i}. \tag{2.11}$$

"Bkg_i is the estimated background event map derived from the ring-background method (Berge, Funk, and Hinton, 2007), A is a normalization factor that is fitted. $(\mathrm{psf} * M_i)$ is the morphological model (shell or Gaussian) map, folded with the H.E.S.S. psf" (H.E.S.S. Collaboration et al., 2018a); all the model's parameters are freely varying in the fit. $N_{\mathrm{ref},i}$ are the expected γ-ray counts, calculated according to the following equation (H.E.S.S. Collaboration et al., 2018b)

$$N_{\mathrm{ref},i} = \sum_{\mathrm{R}\in\mathrm{runs}} T_R \int_{E_{min}}^{\infty} \phi_{\mathrm{ref}}\left(E_r\right) A_{\mathrm{eff}}\left(E_r, q_R\right) \mathrm{d}E_r \tag{2.12}$$

T_R is the observation live-time, A_{eff} is the effective area, which depends on both the reconstructed energy E_r and a set of run-specific parameters q_R (zenith, azimuth and off-axis angle, optical efficiency and pattern of telescopes participating in the run). $\phi_{\mathrm{ref}} = \phi_0 \left(E/E_0\right)^{-\Gamma}$, with $\Gamma = 2.3$ and normalization $\phi_0 = 1\,\mathrm{TeV}^{-1}\mathrm{m}^{-2}\mathrm{s}^{-1}$. The index i runs over the bins.

For one of the sources (HESS J1614−518) another source is visible in the field of view with high significance (HESS J1616−518, cf. Aharonian et al. (2006c)). This has then been modeled as an additional Gaussian component simultaneously to the source of interest, in order to improve the fit stability.

The employed fitting routines are based on the *cstat* implementation of the Cash statistics (Cash, 1979) available in the *Sherpa* package. To quantify the improvement of the fit quality between the two models, the *Akaike Information Criterion* as discussed in Section 2.1.1 has been used. Table 2.5 lists the results for the three new TeV shells, while figure 2.7 shows their *surface brightness maps*.

Figures 2.8, 2.9 and 2.10 show the steps and outcome of the fitting procedure for each of the SNR remnant candidates. As it can be noticed, a Gaussian fit on a *true* shell structure leaves a ring in the fit residuals, while the shell model ensures an almost flat residual map. It is worth noticing that such *ring* is different from the structures described in 2.1.2. In that case, the ring-like artifacts were created as a consequence of the search method construction, around all bright sources; here, the ring residuals are caused by the Gaussian assumption that leaves the emission between R_{in} and R_{out} uncovered. In all cases, the fitted morphologies have been assumed *azimuthally flat*, meaning that no attempt to model any deviation from a spherical symmetry has been performed. For HESS J1534−571 and especially HESS J1614−518, however, this assumption seems to break. For this reason, the symmetry of the newly identified shell sources has been investigated using azimuthal profiles (see Figure 2.11). A χ^2-test has then been applied as a measure for the *flatness* of the profiles; while HESS J1534−571 and HESS J1912+101 do not show any significant deviation from a spherical symmetry, HESS J1614−518 is clearly breaking such hypothesis. An attempt to model the residual excess visible in the North and South of the shell as additional Gaussian components has therefore been made. Adding a source in the North of the shell indeed improves

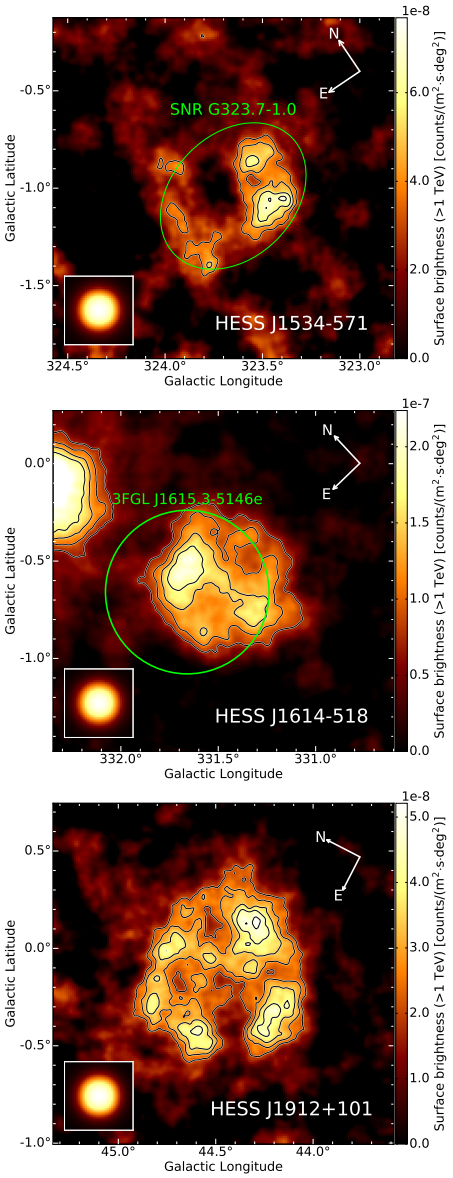

FIGURE 2.7: TeV surface brightness maps of the newly discovered shells in Galactic coordinates. A correlation radius of $0.1°$ was used to produce the maps, together with an additional Gaussian smoothing with $\sigma = 0.01°$ to remove artifacts. The surface brightness is expressed in units of counts above $1\,\mathrm{TeV}$, assuming a power-law with index Γ_{ref}. The inlets show the point spread function, at which the same correlation radius and smoothing has been applied. *Top:* HESS J1534−571, assumed $\Gamma_{\mathrm{ref}} = 2.3$. The green ellipse marks the outer boundary of the SNR G323.7−1.0, discovered in the radio band (Green, Reeves, and Murphy, 2014). The white contours denote 3, 4, 5, 6 σ significance level (correlation radius $0.1°$). *Middle:* HESS J1614−518, assumed $\Gamma_{\mathrm{ref}} = 2.4$. The green circle marks position and extension of the source 3FGL J1615.3−5146e from Acero et al. (2015). The significance contours (correlation radius $0.1°$) are at 5, 7, 9, 11 σ level. *Bottom:* HESS J1912−101, assumed $\Gamma_{\mathrm{ref}} = 2.7$. Contours are 3, 4, 5, 6, 7 σ significance contours (correlation radius $0.1°$). Taken from H.E.S.S. Collaboration et al. (2018a).

TABLE 2.5: Results from the morphological study of the three new TeV shells. [a]: TeV discovery status. [b]: Source detection significance from excess counts $N_{\rm excess}$ detected inside $R_{\rm out}$, following Li and Ma (1983). [c]: Likelihood $\mathcal{L}_{{\rm AIC},H_0}$ as defined in equation 2.7 used as a measure whether the fit improvement of the shell (H_1) over the Gaussian (H_0) is due to fluctuations, using the *Akaike Information Criterion*. [d]: Shell fit results; (l_0, b_0) are the centre coordinates, $R_{\rm in}$ and $R_{\rm out}$ are the inner and outer radii of the homogeneously emitting spherical shell, respectively. Taken from H.E.S.S. Collaboration et al. (2018a)

	HESS J1534−571	HESS J1614−518	HESS J1912+101
Discovery[a]	$\mathrm{TS_{diff}} = 39$	(1)	(2)
Excess[b]	$9.3\,\sigma$	$25.2\,\sigma$	$17.3\,\sigma$
$\mathcal{L}_{{\rm AIC},H_0}$[c]	5.9×10^{-3}	3.1×10^{-6}	1.7×10^{-6}
l_0[d]	$323.70^\circ{}^{+0.02^\circ}_{-0.02^\circ}$	$331.47^\circ{}^{+0.01^\circ}_{-0.01^\circ}$	$44.46^\circ{}^{+0.02^\circ}_{-0.01^\circ}$
b_0[d]	$-1.02^\circ{}^{+0.03^\circ}_{-0.02^\circ}$	$-0.60^\circ{}^{+0.01^\circ}_{-0.01^\circ}$	$-0.13^\circ{}^{+0.02^\circ}_{-0.02^\circ}$
$R_{\rm in}$[d]	$0.28^\circ{}^{+0.06^\circ}_{-0.03^\circ}$	$0.18^\circ{}^{+0.02^\circ}_{-0.02^\circ}$	$0.32^\circ{}^{+0.02^\circ}_{-0.03^\circ}$
$R_{\rm out}$[d]	$0.40^\circ{}^{+0.04^\circ}_{-0.12^\circ}$	$0.42^\circ{}^{+0.01^\circ}_{-0.01^\circ}$	$0.49^\circ{}^{+0.04^\circ}_{-0.03^\circ}$

References. (1) Aharonian et al. (2006c); (2) Aharonian et al. (2008a).

the quality of the fit with respect to a shell-only model; however, "the parameters of the additional Gaussian component are not consistent within statistical errors when modifying analysis configurations or using the cross-check analysis. Also, no consistent significant result could be established using the main and the cross-check analysis when attempting to model the apparent excess in the South of the HESS J1614−518 shell as additional Gaussian component. Therefore, fit results for models including these additional components are not given here"(H.E.S.S. Collaboration et al., 2018a)[6].

In 2014, a new SNR candidate (G323.7−1.0) was discovered in the radio band, as part of the data collected with the Molonglo Observatory Synthesis Telescope (MOST) at a frequency of 843 MHz, for the latest Molonglo Galactic Plane Survey MGPS-2. A quantitative comparison between the TeV and the radio sources has been performed through the extraction of elliptical profiles (see Figure 2.12). Given the good matching between the two shell candidates in TeV and radio, HESS J1534−571 is therefore classified as new TeV SNR.

The flux density of the radio source is (0.49 ± 0.08) Jy and it can be used to give a ballpark estimate of its distance, exploiting the empirical surface brightness-to-diameter ($\Sigma - D$) relation (Case and Bhattacharya, 1998), expressed by Eq. 2.13.

$$\Sigma_{1\,\mathrm{GHz}} = 2.07 \times 10^{-17} \times D\,[\mathrm{pc}]^{-2.38}\ \mathrm{W\,m^{-2}Hz^{-1}sr^{-1}} \tag{2.13}$$

$\Sigma_{1\,\mathrm{GHz}}$ is the surface brightness of the source at frequency $\nu_1 = 1\,\mathrm{GHz}$ (the errors on the parameters in 2.13 are omitted). Moreover, as a first approximation:

$$D = \theta d \tag{2.14}$$

where θ is the angular extension of the source in radians.

[6]The attempt to model the northern and southern residual excesses is shown in more detail in Appendix C

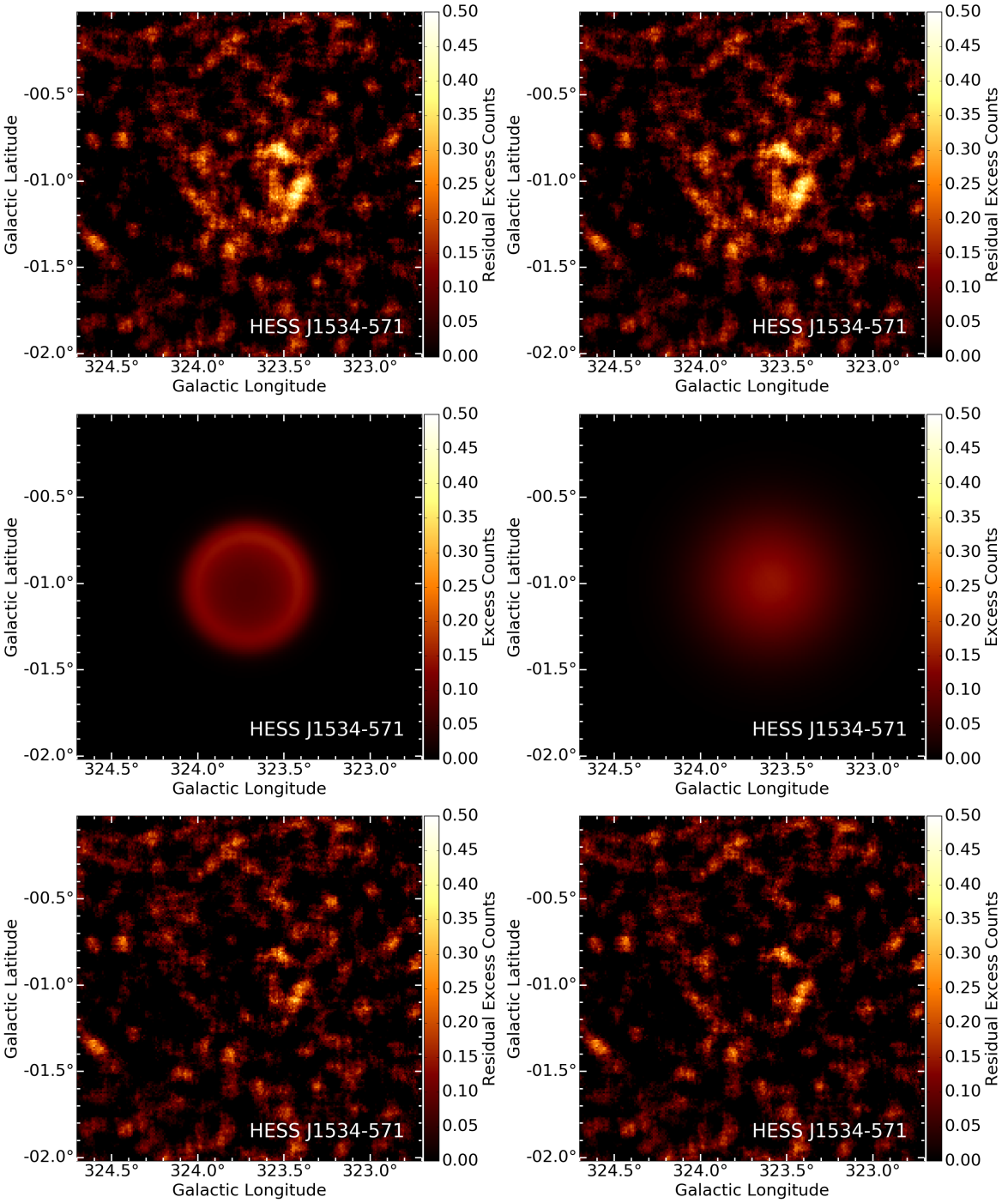

FIGURE 2.8: Results from the morphological fit on the TeV SNR shell candidate HESS J1534−571. *Top:* Residual excess counts after a background only fitting ($\mathrm{On} - A \times \mathrm{Bkg}$), smoothed with a $0.05°$ top-hat filter for visualization. *Middle:* Best-fit shell and Gaussian model (left and right respectively). *Bottom:* Residual excess counts after modelling of the emission region with a background plus shell(Gaussian) model (left and right respectively), smoothed with a $0.05°$ top-hat filter for visualization.

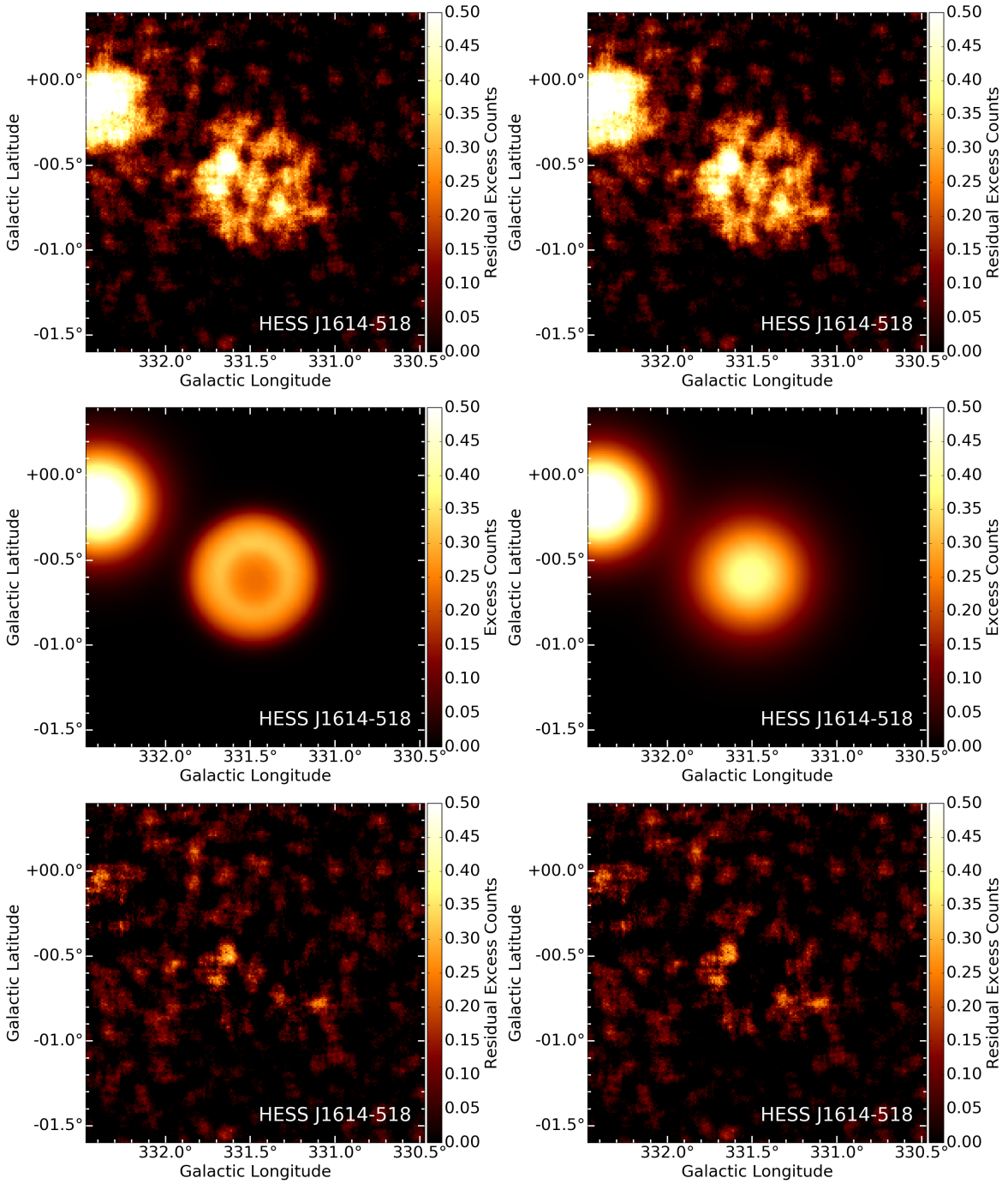

FIGURE 2.9: Results from the morphological fit on the TeV SNR shell candidate HESS J1614−518. *Top:* Residual excess counts after a background only fitting ($\mathrm{On} - A \times \mathrm{Bkg}$), smoothed with a 0.05° top-hat filter for visualization. *Middle:* Best-fit shell and Gaussian model (left and right respectively). The other source appearing in the field of view (HESS J1616−508) has been modelled as additional Gaussian component. *Bottom:* Residual excess counts after modelling of the emission region with a background plus shell(Gaussian) model (left and right respectively), smoothed with a 0.05° top-hat filter for visualization. As it can be noticed, even after subtracting the best-fit shell and Gaussian models, residuals in the northern and southern region of HESS J1614−518 are left. An attempt to further model this *leftover* emission is explained in Appendix C.

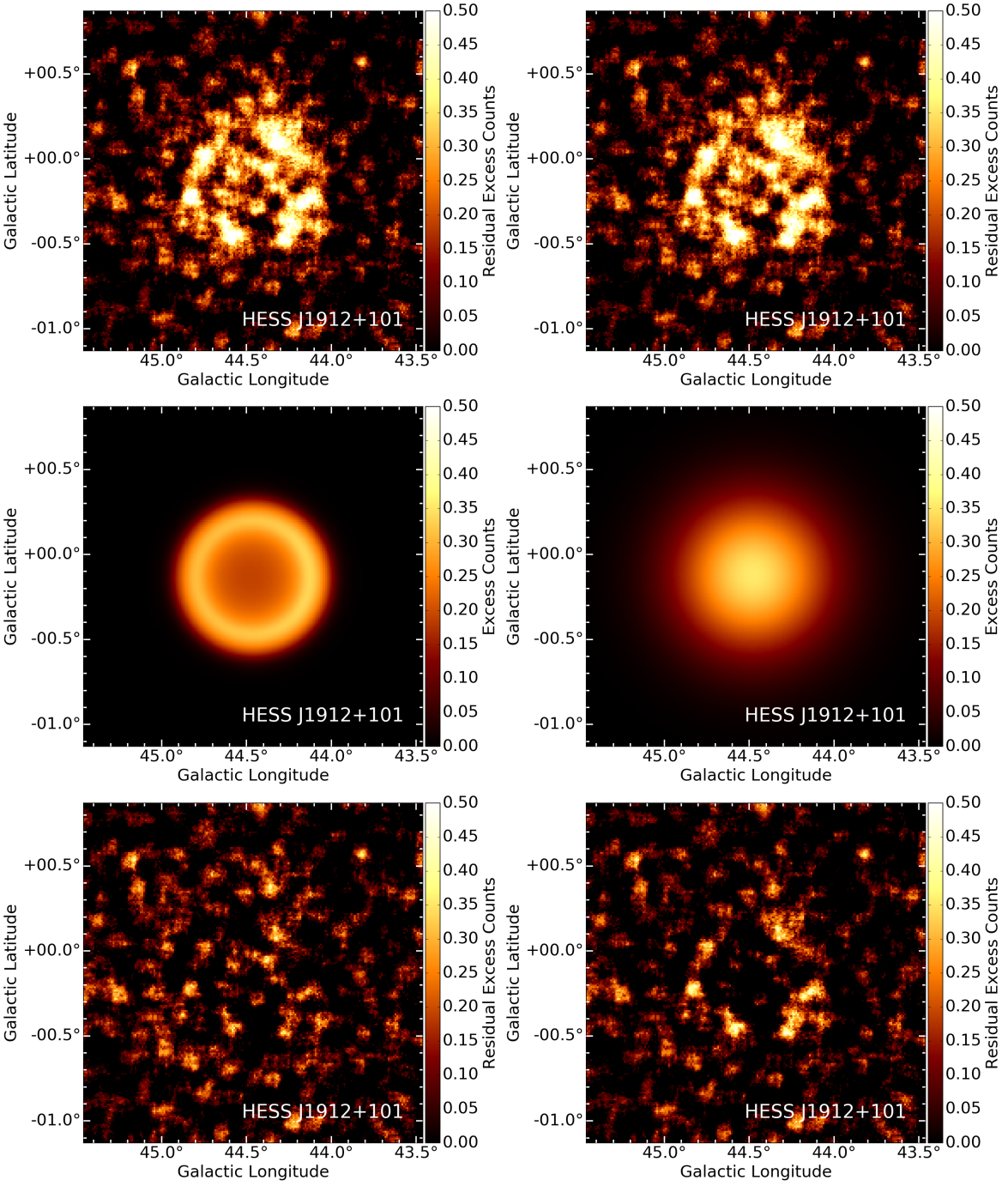

FIGURE 2.10: Results from the morphological fit on the TeV SNR shell candidate HESS J1912+101. *Top:* Residual excess counts after a background only fitting ($\mathrm{On} - A \times \mathrm{Bkg}$), smoothed with a $0.05°$ top-hat filter for visualization. *Middle:* Best-fit shell and Gaussian model (left and right respectively). *Bottom:* Residual excess counts after modelling of the emission region with a background plus shell(Gaussian) model (left and right respectively), smoothed with a $0.05°$ top-hat filter for visualization. Particularly apparent in this last case is the ring-like artefact left after subtraction of the best-fit Gaussian model, in the presence of a possibly *true* shell-like structure; on the other hand, the residuals after subtraction of the best-fit shell model appear to be flat.

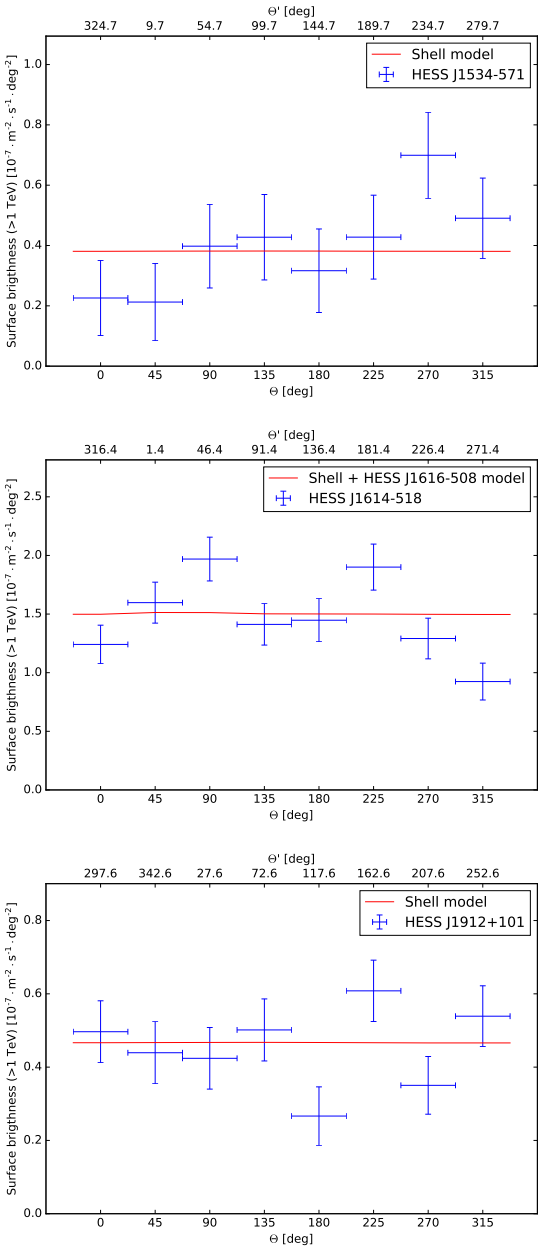

FIGURE 2.11: TeV azimuthal profiles for HESS J1534−571, HESS J1614−518, and HESS J1912+101. To derive the profiles, the sources have been divided into eight wedges of equal size with outer radius $R_{\rm out}$ and inner radius slightly smaller than $R_{\rm in}$ to focus on the bright emission. Θ is the angle with respect to the Galactic latitude. The first wedge is at $\Theta = 0°$, following wedges are added counter-clockwise. Θ' is the angle with respect to North in equatorial coordinates. The shell and Gaussian models are from fits to the data. Taken from H.E.S.S. Collaboration et al. (2018a).

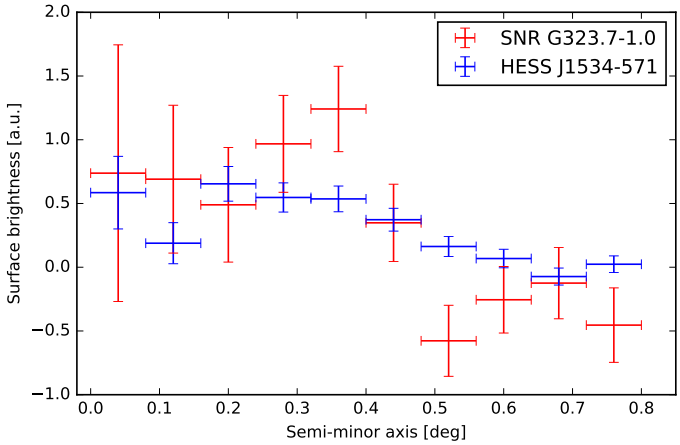

FIGURE 2.12: Radial profile of HESS J1534−571 and G323.7−1.0, obtained using elliptical annuli. The angle of the major axis with respect to North has been estimated from the radio map to be $100°$. The radio image has been convolved with the H.E.S.S. point spread function before extraction of the profile, in order to obtain the same angular resolution as for the TeV map. Both profiles were normalized to have the same integral value. Taken from H.E.S.S. Collaboration et al. (2018a).

The surface brightness at a given frequency ν can be calculated from the following definition:

$$\Sigma_\nu = 1.505 \times 10^{-19} \times \frac{S_\nu\,[\mathrm{Jy}]}{\theta^2}\,\mathrm{W\,m^{-2}Hz^{-1}sr^{-1}} \tag{2.15}$$

where S_ν is the flux density at frequency ν and θ is expressed in arcminutes. Therefore, knowing $S_{1\,\mathrm{GHz}}$ and θ, the source distance can be easily estimated. In this case, $S_{1\,\mathrm{GHz}}$ has to be derived from $S_{843\,\mathrm{MHz}}$, assuming that $S \propto \nu^{-\alpha}$ with $\alpha \approx 0.5$ (see e.g,: (Reynolds, 2011)).

Considering the known flux density at $843\,\mathrm{MHz}$, the estimated distance is $\sim 20\,\mathrm{kpc}$. As further discussed in Section 2.2, however, such a far distance would imply a luminosity in the $1 - 10\,\mathrm{TeV}$ band substantially greater than the typical values for the known SNR shells, even more than 10 times (see Table 2.6 for a detailed comparison).

It has to be considered that the distances estimated through the $\Sigma-D$ relation are affected by typical errors of 40% (Case and Bhattacharya, 1998). In addition to that, as discussed in Green, Reeves, and Murphy (2014), the MOST telescope does not fully resolve structures with a scale larger than $\sim 25'$; as a consequence, the flux densities for large sources such as G323.7−1.0 (having an extension of $\sim 48'$) are underestimated. Even assuming a two times higher flux density, however, the estimated distance ($\sim 15\,\mathrm{kpc}$) would still imply a oddly high TeV luminosity for HESS J1534−571.

Another possibility would be that HESS J1534−571 belongs to the class of shell-type SNRs with very faint radio emission, along with e.g, RX J1713.7−3946 (Lazendic et al., 2004) and Vela Jr (Aschenbach (1998), Slane et al. (2001)). Under this hypothesis, the distance derived through the $\Sigma - D$ relation would be largely overestimated. In the case of RX J1713.7−3946, a commonly accepted distance is $1\,\mathrm{kpc}$ (Fukui et al., 2003). However, considering a flux density of $\sim 25\,\mathrm{Jy}$ (Acero et al., 2009) would lead to a distance of $\sim 3\,\mathrm{kpc}$,

TABLE 2.6: Parameters of known TeV SNR shells. For each of the sources, diameter and $L_{\gamma,1-10\,\mathrm{TeV}}$ are calculated based on the parameters quoted in the respective papers. Where power laws with cutoffs better fit the spectra and have been used to compute luminosities, the corresponding fit values are also reported (Simple cutoff power-law models are described by the following equation: $\mathrm{d}N/\mathrm{d}E = N_0(E/E_0)^{-\Gamma}e^{-E/E_{cut}}$, where E_{cut} is the cutoff energy). The distance to HESS J1731−347 is debated in the literature (see e.g, Fukuda et al., 2014; Klochkov et al., 2015), the values reported in the table correspond to the two most probable distance solutions. Flux errors are dominated by their systematic errors of typically 20%, but luminosity errors are dominated by the distance uncertainties and are therefore of the order of 30% or more. Spectral indices have statistical errors of $\Delta\Gamma \approx 0.2$ or better. Taken from H.E.S.S. Collaboration et al. (2018a)

Source name	Dist. [kpc]	Diameter [pc]	Age [kyr]	$L_{\gamma,1-10\,\mathrm{TeV}}$ [$10^{33}\mathrm{erg\,s^{-1}}$]	$\Gamma_{\gamma,\mathrm{PLfit}}$	$\Gamma_\gamma/E_{\mathrm{cutoff}}$ -/[TeV]
RX J0852.0−4622[(1)]	0.75	26.2	$1.7-4.3$	5.7	2.3	1.8/6.71
RX J1713.7−3946[(2)]	1	20.2	≈ 1	7.2	2.3	2.1/12.92
HESS J1731−347[(3)]	3.2/5.2	30.2/49	≈ 2.5	8.5/22.4	2.3	
RCW 86[(4)]	2.5	≈ 30	≈ 1.8	6.3	2.3	1.6/3.5
SN 1006 (NE)[(5)]	2.2	22.3	≈ 1	0.46	2.4	
SN 1006 (SW)[(5)]				0.31	2.3	

References. (1) Aharonian et al. (2007b) and H.E.S.S. Collaboration (2016b); (2) Aharonian et al. (2006a) and H.E.S.S. Collaboration (2016d); (3) H.E.S.S. Collaboration (2011) and Klochkov et al. (2015); (4) H.E.S.S. Collaboration (2016c); (5) Acero et al. (2010).

according to Equation 2.13. In other terms, a higher radio flux density (of a factor of ~ 25) would bring the SNR at the *right* distance.

Assuming that a similar situation holds for HESS J1534−571, the SNR could in fact be located at a distance of $\sim 5\,\mathrm{kpc}$. In this case, the TeV luminosity of the source would be in a better agreement with the ones of the known TeV shells.

Search for X-ray emission with *Suzaku* from HESS J1534−571 and physical implications of a confirmed non-detection.

Over the last decades, SNRs have been widely studied by the astrophysical community. One of the main reasons behind this interest, is the belief that they can significantly contribute to the generation of Galactic CRs up to the knee in the CR particle spectrum. In this view, the search for counterparts in the X-ray and radio bands, as well as an estimate of the source distance, are essential to determine what fraction of the supernova ejecta energy goes into thermal plasma (typically X-ray emitting) and what fraction goes into non-thermal relativistic leptons and hadrons.

An extensive search for multiwavelength counterparts for the three TeV shells, as well as possible distance estimates, is thoroughly treated in H.E.S.S. Collaboration et al., 2018a.

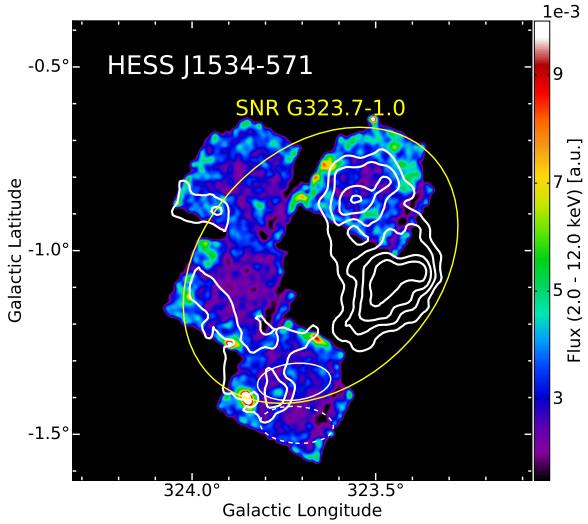

FIGURE 2.13: *Suzaku* XIS mosaic of the pointings towards HESS J1534−571, in a hard band of 2-12 keV, using the XIS0 and XIS3 detectors. Point sources have not been removed from the image. Contours denote the TeV surface brightness. The large solid ellipse denotes the outer boundary of the radio SNR. The small solid ellipse is the extraction region to derive an X-ray upper limit estimate from the SNR, the dashed ellipse is the corresponding background extraction region. Taken from H.E.S.S. Collaboration et al. (2018a).

In the following, only the most significant results are reported.

A search for X-ray emission from the SNR HESS J1534−571 was performed with *Suzaku* XIS (Mitsuda et al., 2007; Koyama et al., 2007); after the initial four pointings, new observations aiming at completing the coverage of the source had been approved, but could not be performed due to the satellite's failure.

From the performed observations, no significant X-ray emission could be detected. Nonetheless, a flux upper limit has been estimated from an absorbed power-law model, assuming two different photon indices Γ. The fluxes are $2.4 \times 10^{-11}\,\mathrm{erg\,cm^{-2}\,s^{-1}}$ in the $2 - 12\,\mathrm{keV}$ band for $\Gamma = 2$ and $1.9 \times 10^{-11}\,\mathrm{erg\,cm^{-2}\,s^{-1}}$ in the same band for $\Gamma = 3$. Since the spectral parameters have been obtained from a region smaller than the whole remnant, the flux has been accordingly scaled to the area of the entire radio SNR (see Figure 2.13).

In young to middle-aged SNRs, synchrotron X-ray emission from relativistic leptons is expected. Following the arguments in Yamazaki et al. (2006), one can define the ratio

$$R = \frac{F_\gamma\,(1 - 10\,\mathrm{TeV})}{F_X\,(2 - 10\,\mathrm{keV})} \tag{2.16}$$

between the γ- and X-ray fluxes in specific energy bands. For young SNRs (with ages up to $\sim 10^3\mathrm{yr}$), non-thermal X-rays are dominated by the synchrotron emission from primary electrons, while TeV γ-rays are dominated by π^0-decay, and R is expected to be significantly lower than 2. On the other hand, R is ~ 2 if the SNR age is $\sim 10^4\mathrm{yr}$. For older SNRs (with ages $\sim 10^5\mathrm{yr}$), the acceleration of high energy protons is still efficient enough and can lead to the production of γ-rays via π^0-decay, while the generation of X-rays is dominated by synchrotron emission from secondary electrons; in this case R can be significantly higher

than 2 (as high as $\sim 10^2$). For such sources, the X-ray spectrum is expected to be dominated by secondary electrons, which are however not energetic enough to explain the VHE γ-ray emission (dominated by π^0-decay instead). In this sense, if the TeV emission stems from relativistic electrons, non-thermal X-rays above $\sim 2\,\mathrm{keV}$ are expected and their non-detection could be advocated to favor hadronic scenarios.

If the upper limit found in X-rays can be applied to the whole HESS J1534−571 shell, $R \geqslant 0.25$. A detection with currently operating satellites should be achievable, even though challenging because of the large extension of the source.

Finally, if such upper limit were confirmed, HESS J1534−571 would be the first TeV SNR without an X-ray counterpart at current satellite sensitivity.

Further multiwavelength counterparts to the new TeV shells

In addition to HESS J1534−571, also HESS J1614−518 has an identified counterpart in a lower waveband, which is listed in the LAT source catalogues, namely 3FGL J1615.3−5146e / 2FHL J1615.3−5146e. Contrary to HESS J1534−571, however, this identification does not bring any additional information to improve the astrophysical classification of the object.

2.2 Proton scenarios: energy content in accelerated Cosmic Rays

"Assuming that the γ-ray emission seen in the TeV regime is purely due to hadronic processes, an estimate of the fraction of the SNR explosion energy going into accelerated CR protons can be given.

In the delta-function approximation (Kelner, Aharonian, and Bugayov, 2006), γ-ray photons of energy E_γ are produced by protons with energy $E_\mathrm{p} = 10 \times E_\gamma$. Following the arguments in Aharonian et al. (2006a), the total energy in accelerated protons in the $10 - 100\,\mathrm{TeV}$ range can be estimated from the γ-ray luminosity in the range $1 - 10\,\mathrm{TeV}$, using

$$W_\mathrm{p}^\mathrm{tot}\,(10 - 100\,\mathrm{TeV}) \approx \tau_{\mathrm{pp}\to\pi^0} L_\gamma\,(1 - 10\,\mathrm{TeV})\,. \tag{2.17}$$

$$\tau_{\mathrm{pp}\to\pi^0} \approx 4.5 \times 10^{15} \left(\frac{n}{\mathrm{cm}^{-3}}\right)^{-1} \mathrm{s} \tag{2.18}$$

is the characteristic cooling time of protons by π^0 production and

$$L_\gamma(1 - 10\,\mathrm{TeV}) = 4\pi d^2 \int_{1\,\mathrm{TeV}}^{10\,\mathrm{TeV}} E_\gamma \frac{\mathrm{d}N_\gamma}{\mathrm{d}E} \mathrm{d}E, \tag{2.19}$$

where d is the distance to the source and $\mathrm{d}N_\gamma/\mathrm{d}E = N_{0,1\,\mathrm{TeV}}\,(E/1\,\mathrm{TeV})^{-\Gamma}$. $N_{0,1\,\mathrm{TeV}}$ and Γ are derived from the fit to the TeV data as presented in Table 2.7" (H.E.S.S. Collaboration et al., 2018a).

TABLE 2.7: Spectral fit results from the power-law fits to the H.E.S.S. data. Both statistical and systematic errors are given for the fit parameters. The systematic uncertainties result from deviations from the nominal parameters of the simulations of the instrument, non-optimized observation strategy, and the large size of the sources which lead to substantial susceptibility of the spectral results to potential errors in the background estimation (cf H.E.S.S. Collaboration et al. (2018a), Sect. 2.2.2), and are estimated to 30% for N_0 and energy flux and to 0.2 for Γ, respectively. To simplify a comparison between the sources, the normalization at 1 TeV, $N_{0,1\,\mathrm{TeV}}$, and the energy flux from 1 TeV to 10 TeV are given as well. Taken from H.E.S.S. Collaboration et al. (2018a)

Source	E_0	N_0	Γ
HESS	[TeV]	[$\mathrm{cm^{-2}\,s^{-1}\,TeV^{-1}}$]	
J1534−571	1.40	$(1.29 \pm 0.12_{\mathrm{stat}} \pm 0.39_{\mathrm{syst}}) \times 10^{-12}$	$2.51 \pm 0.09_{\mathrm{stat}} \pm 0.20_{\mathrm{syst}}$
J1614−518	1.15	$(5.86 \pm 0.34_{\mathrm{stat}} \pm 1.76_{\mathrm{syst}}) \times 10^{-12}$	$2.42 \pm 0.06_{\mathrm{stat}} \pm 0.20_{\mathrm{syst}}$
J1912+101	2.25	$(4.82 \pm 0.43_{\mathrm{stat}} \pm 1.45_{\mathrm{syst}}) \times 10^{-13}$	$2.56 \pm 0.09_{\mathrm{stat}} \pm 0.20_{\mathrm{syst}}$

Source	$N_{0,1\,\mathrm{TeV}}$	energy flux (1 − 10 TeV)
HESS	[$\mathrm{cm^{-2}\,s^{-1}\,TeV^{-1}}$]	[$\mathrm{erg\,cm^{-2}\,s^{-1}}$]
J1534−571	$(2.99 \pm 0.30_{\mathrm{stat}} \pm 0.90_{\mathrm{syst}}) \times 10^{-12}$	$(6.5 \pm 0.7_{\mathrm{stat}} \pm 2.0_{\mathrm{syst}}) \times 10^{-12}$
J1614−518	$(8.33 \pm 0.49_{\mathrm{stat}} \pm 2.50_{\mathrm{syst}}) \times 10^{-12}$	$(2.0 \pm 0.2_{\mathrm{stat}} \pm 0.6_{\mathrm{syst}}) \times 10^{-11}$
J1912+101	$(3.89 \pm 0.45_{\mathrm{stat}} \pm 1.17_{\mathrm{syst}}) \times 10^{-12}$	$(8.1 \pm 0.7_{\mathrm{stat}} \pm 2.4_{\mathrm{syst}}) \times 10^{-12}$

"Knowing $W_{\mathrm{p}}^{\mathrm{tot}}(10 - 100\,\mathrm{TeV})$ and assuming a power-law spectrum for the accelerated protons ($\mathrm{d}N_{\mathrm{p}}/\mathrm{d}E = N_{\mathrm{p}}E^{-\alpha}$, with $\alpha = \Gamma$ and N_{p} a normalization factor), $W_{\mathrm{p}}^{\mathrm{tot}}$ can be calculated in an arbitrary proton energy range. It is assumed that the proton energy spectrum can be described by a broken power law with a break energy at 10 TeV,

$$\frac{\mathrm{d}N_{\mathrm{p}}}{\mathrm{d}E} = \begin{cases} N_{\mathrm{p},1}E^{-2} & 1\ \mathrm{GeV} \leq E_{\mathrm{p}} \leq\ 10\ \mathrm{TeV} \\ N_{\mathrm{p},2}E^{-\alpha} & 10\ \mathrm{TeV} < E_{\mathrm{p}} \leq\ 100\ \mathrm{TeV} \end{cases} \tag{2.20}$$

which is roughly compatible with the TeV spectra of all three new shell sources and the GeV spectrum of the *Fermi*-LAT source associated with HESS J1614−518.

To illustrate the possible energy contents in accelerated protons, three scenarios are given in Table 2.8 for each source. The first one is a generic case with a distance of 1 kpc and a target gas density of $1\,\mathrm{cm^{-3}}$. The other two are derived from the possible gas association scenarios" as discussed in H.E.S.S. Collaboration et al. (2018a), "with error ranges propagated from the estimated ranges of gas densities. The table lists both the energy contents of the protons in the TeV-emitting energy range and for an extrapolated spectrum down to 1 GeV. The latter values show that the available data are compatible with the expected energy content of 10% of $10^{51}\mathrm{erg}$ for assumed nearby distances of $\sim$1 kpc and for moderate distances of $\sim$3 kpc. Distances at a $8 - 10$ kpc scale and beyond are disfavoured in hadronic emission

scenarios"(H.E.S.S. Collaboration et al., 2018a).

2.3 Conclusions

The study presented in this chapter has demonstrated the potential of current-generation IACTs to discover new SNRs, based on their morphological appearance in the TeV band. During this work, three significant shell structures could be identified in the data of the latest survey of the Galactic Plane with H.E.S.S.: HESS J1534−571, HESS J1614−518 and HESS J1912+101. Given the presence of a morphologically matching radio counterpart, HESS J1534−571 could be classified as *new* SNR. For the other two sources, no compelling multiwavelength counterpart could be found; for this reason, they are at present considered SNR *candidates*.

For HESS J1534−571, the apparent lack of non-thermal X-rays from the source region seems to point towards a hadronically-dominated TeV emission. However, no confirmed upper limit at current satellite sensitivity could be derived to constrain this hypothesis. In general, a hadronic scenario is plausible for all the new TeV shells, provided that their distances are not too high. Moreover, such high distances would set the sources apart from the known class of $1 - 10\,\mathrm{TeV}$ SNR shells, in terms of luminosity in the $1 - 10\,\mathrm{TeV}$ band and physical dimensions.

To our knowledge, it was the first time that a morphological search criterion could be successfully applied to identify new TeV-selected SNRs. The next-generation IACT (CTA) is expected to improve the sensitivity to detect such objects, though the problem of source confusion may occur more frequently than in the analysis presented in this chapter.

TABLE 2.8: Parameters of the new TeV SNR candidates, assuming a generic $1\,\mathrm{kpc}$ distance and two other distances coming from possible association scenarios. The gas parameters are derived from HI and CO(1-0) emission, from circular regions towards HESS J1534−571, HESS J1614−518 and HESS J1912+101 in the respective velocity ranges; the centres and extensions of these regions are the best fit centres and R_{out} presented in Table 2.5 as derived from the morphological study of the TeV sources. The resulting total encircled gas mass is given in $M_{\mathrm{HI+H2}}$. Density ranges are calculated by assuming that the line of sight thickness is between a value equal to the SNR diameter (upper limit) and the approximate thickness of a Galactic arm ($0.5\,\mathrm{kpc}$ lower limit) (see H.E.S.S. Collaboration et al. (2018a), appendix A for a more detailed description). $n_{\mathrm{p,HI}}$, $n_{\mathrm{p,H2}}$ indicate the estimated gas density coming from atomic (HI) and molecular (H2) gas contributions, respectively. W_{p}^{*} gives the energy content of relativistic protons in the range $10-100\,\mathrm{TeV}$, that emit gamma-rays in the range $1-10\,\mathrm{TeV}$; the proton spectral index is the same as the photon index Γ in the TeV range (see Table 2.7). W_{p}^{**} assumes a proton spectral index equal to the TeV photon index from $10-100\,\mathrm{TeV}$ and an index of 2 from $10\,\mathrm{TeV}$ down to $1\,\mathrm{GeV}$ in proton energy. Taken from H.E.S.S. Collaboration et al. (2018a)

HESS source name	distance [kpc]	velocity [$\mathrm{km\,s^{-1}}$]	diameter [pc]	$L_{\gamma,1-10\,\mathrm{TeV}}$ [$1\times10^{33}\,\mathrm{erg\,s^{-1}}$]	$M_{\mathrm{HI+H2}}$ [$\mathrm{M_\odot}$]	$n_{\mathrm{p,HI}}$ [$\mathrm{cm^{-3}}$]	$n_{\mathrm{p,H2}}$ [$\mathrm{cm^{-3}}$]	$n_{\mathrm{p,HI+H2}}$ [$\mathrm{cm^{-3}}$]	$W^{*}_{\mathrm{p,10\,TeV-100\,TeV}}$ [$1\times10^{51}\,\mathrm{erg}$]	$W^{**}_{\mathrm{p,1\,GeV-100\,TeV}}$ [$1\times10^{51}\,\mathrm{erg}$]
HESS J1534−571	1.0		14.0	0.78				1	0.004	0.03
	3.5	−55..−45	48.9	9.6	3.0×10^{4}	3..29	1..10	4..39	0.01..0.001	0.08..0.009
	8	−88..−78	111.7	50	6.4×10^{4}	1..6	0.3..1	1.3..7	0.17..0.03	1.34..0.25
HESS J1614−518	1.0		14.7	2.4				1	0.01	0.08
	1.5	−30..−12	22	5.3	4.9×10^{3}	3..71	0	3..71	0.008..0.0003	0.06..0.002
	5.5	−110..−80	80.6	71	3.7×10^{5}	5..33	12..77	17..110	0.02..0.003	0.14..0.02
HESS J1912+101	1.0		17.1	0.97				1	0.004	0.04
	4.5	45..73	77.0	19.6	4.7×10^{5}	7..44	21..134	28..178	0.003..0.0005	0.03..0.004
	10	5..15	171.0	97	2.2×10^{5}	3..6	1..2	4..8	0.11..0.05	0.88..0.44

Chapter 3

The supernova remnant HESS J1731−347 and its surroundings: a TeV-gas correlation study

SNRs are believed to be responsible for the production and efficient acceleration of the bulk of Galactic CRs at their shock fronts, up to energies that reach the *knee* of the CR particle spectrum (Zirakashvili and Ptuskin, 2008).

If particle acceleration is in fact ongoing at young SNRs shock-fronts, unbroken VHE spectra with indices $\Gamma = 2$, up to energies of $\sim 100\,\mathrm{TeV}$, are expected. However, such direct observational evidence is still lacking, as all spectra of young TeV-SNRs show either *soft* indexes ($\Gamma > 2$) and (or) cutoffs.

A possible explanation could be that the TeV emission is dominated by IC scattering from relativistic electrons off low-energy ambient photons. On the other hand, SNRs are expected to accelerate multi-PeV protons only when they are relatively young, at the end of the free expansion phase/beginning of the Sedov phase (Gabici and Aharonian, 2007). After that period, the shock slows down, the maximum energy of the CRs that can be confined reduces, and the higher energy particles can escape the accelerator region. This causes the high-energy cutoff in the CRs spectrum (and hence in the γ-ray one) to move towards lower energies, and the spectrum itself to become rather steep ($\Gamma \approx 3$) above the cutoff. In this case, the X-ray synchrotron radiation from electrons and the π^0 decay-dominated VHE TeV emission would show a different morphology: the latter would be more extended. Such effect could even be more apparent when dense gas clouds serve as target material for the production of neutral pions.

This chapter focuses on the shell-type TeV SNR HESS J1731−347. Part of the work presented herein was published by the author in Capasso et al. (2017); citations in the text taken from this paper are enclosed in quotation marks. HESS J1731−347 shows similar parameters to the known TeV shells in terms of physical size and luminosity in the $1 - 10\,\mathrm{TeV}$ band (see Table 2.6). As RX J1713.7−3946 and Vela Jr., HESS J1731−347 is found to be spatially coincident with a faint radio SNR (G353.5−0.7, Tian et al. (2008)) and displays non-thermal X-ray emission (H.E.S.S. Collaboration (2011), Bamba et al. (2012), Doroshenko et al. (2017)); moreover, a central compact object (CCO) is found at the centre of the remnant, suggesting a possible origin from a massive progenitor. "Hadronic and leptonic scenarios (or a blend

of both) are discussed in the literature to explain the TeV emission from the object (see e.g.,: Fukuda et al. (2014), Doroshenko et al. (2017))" (Capasso et al., 2017).

The distance of the source from Earth is widely debated as well. Three possible scenarios are discussed in several works, namely:

- **near-distance solution ($\sim 3.2\,\mathrm{kpc}$):** "By comparing the interstellar absorption derived from X-rays and the one obtained from ^{12}CO and HI observations, a lower limit on the source distance of $\sim 3.2\,\mathrm{kpc}$ (Scutum-Crux arm) is derived in H.E.S.S. Collaboration (2011)." "Klochkov et al. (2015) use numerical spectral models for carbon and hydrogen atmospheres to fit the spectrum of the central compact object (CCO) located towards the geometrical centre of the SNR, supporting the possibility of the source located in the Scutum-Crux arm" (Capasso et al., 2017). Analysing XMM-*Newton* observations that cover the entire shell for the first time, Doroshenko et al. (2017) use a similar argument to place a lower limit to the source of $\sim 3.2 - 4\,\mathrm{kpc}$. Maxted et al. (2017) argue that the X-ray absorption column densities derived from the source X-ray emission are consistent with the ones derived using X-factors from the cumulative HI+CO column densities at a distance of $\sim 3.2\,\mathrm{kpc}$.

- **mid-distance solution ($\sim 4.5\,\mathrm{kpc}$):** the second arm crossing the line of sight at HESS J1731−347 Galactic longitude ($l = 353.5°$) is the Norma-arm. As discussed in H.E.S.S. Collaboration (2011), this association would place the remnant at a distance of $\sim 4.5\,\mathrm{kpc}$.

- **far-distance solution ($\sim 5 - 6\,\mathrm{kpc}$):** Fukuda et al. (2014) argue that the TeV γ-ray emission and the interstellar protons at a distance of $\sim 5.2\,\mathrm{kpc}$ show a significant correlation, placing the SNR in the $3\,\mathrm{kpc}$ expanding arm.

As noted in (H.E.S.S. Collaboration, 2011), farther distances (beyond the Galactic Centre) would lead to a γ-ray luminosity and a physical size at odds with the ones of the known TeV shells, and are thus disfavoured. Figure 3.1 shows a face-on view of the Galaxy, as obtained from Vallée's 2014 model (Vallée, 2014), with the possible locations of HESS J1731−347 along the line of sight.

In addition to HESS J1731−347, another γ-ray excess was also found in the neighbourhood of the source, namely HESS J1729−345 (H.E.S.S. Collaboration, 2011). "In a recent paper, Cui, Pühlhofer, and Santangelo (2016) demonstrate that, assuming HESS J1731−347 is located at a distance of $3.2\,\mathrm{kpc}$, it is possible that the emission seen in TeV from HESS J1729−345 is produced by CRs escaping from the SNR and illuminating nearby molecular clouds (MCs)" (Capasso et al., 2017).

In this chapter, results of an updated analysis obtained with the meanwhile available additional H.E.S.S. data are presented. "Beyond HESS J1731−347, the analysis reveals the morphology of the emission in-between the two sources in greater detail. The results permit to correlate the TeV emission outside the SNR with molecular gas tracers, and to confront the data with scenarios in which the TeV emission outside the SNR is produced by escaping CRs" (Capasso et al., 2017). More specifically, a correlation study between the TeV emission

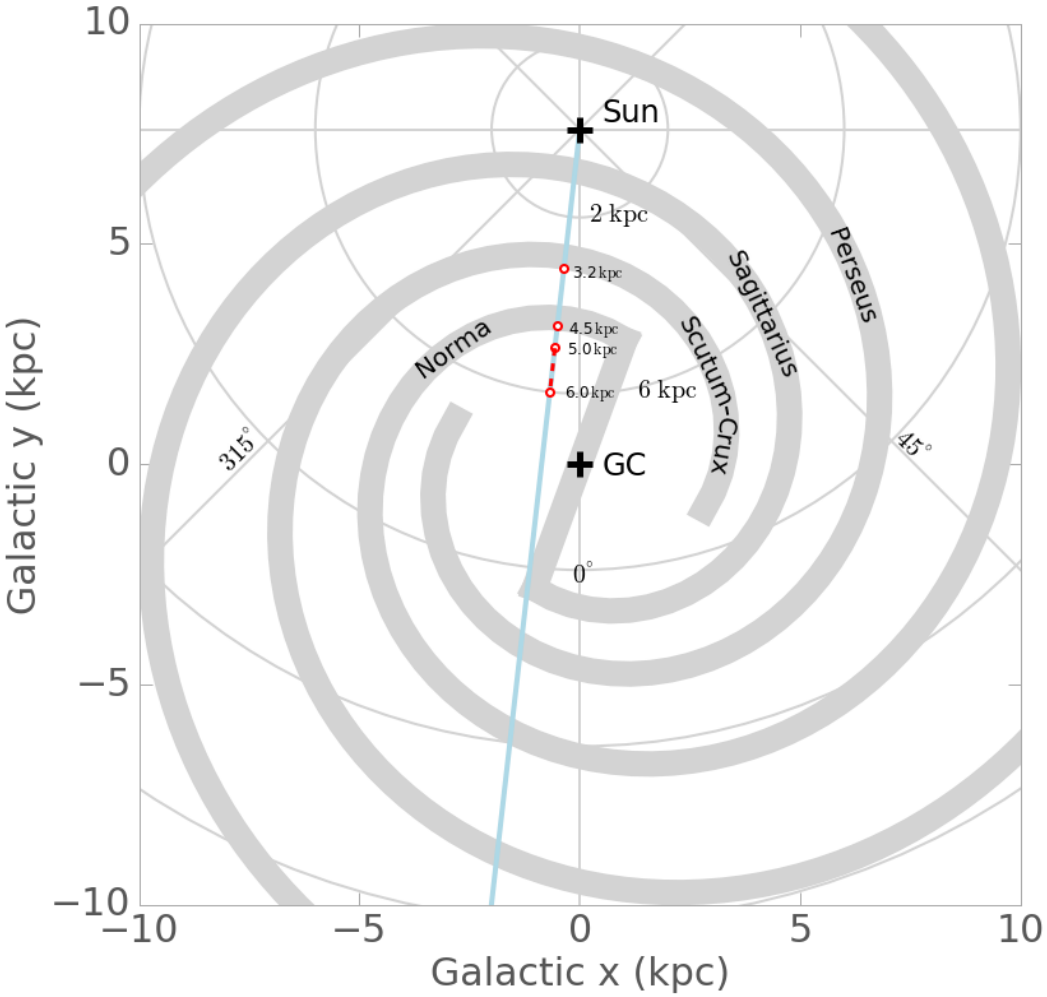

FIGURE 3.1: Galactic spiral arms, as obtained from Vallée (2014). The positions of the Sun and of the Galactic Centre are marked with black crosses. The blue line indicates the Galactic longitude of HESS J1731−347 centroid ($l_0 = 353.5°$). The three possible locations of the source along this line of sight are marked with red circles; the far-distance solution between 5 and 6 kpc is indicated with a dashed line. The size of the Galactic arms is arbitrarily chosen for illustrative purposes. This plot was realized with the aid of Gammapy routines, as presented in Donath et al. (2015)

.

from SNR's region and the CS and CO radio line emission from recently available Mopra[1] data is carried out.

3.1 Available datasets

In the following section, a brief overview of the available TeV and radio datasets is given. The correlation study presented in Section 3.3 has been performed on sky map products derived from processing of these data.

3.1.1 VHE γ-rays from H.E.S.S.

Observations

HESS J1731−347 was first discovered in VHE γ-rays with H.E.S.S. as extended unidentified source (Aharonian et al., 2008b). Following the discovery of the radio shell-type SNR G353.6−0.7 (Tian et al., 2008), spatially coincident with the unidentified TeV object, additional H.E.S.S. observations were carried out up to 2009. The data revealed a significant TeV shell morphology with outer radius $R_{\rm out} = 0.27^\circ \pm 0.02^\circ$ and a flat azimuthal profile within statistical errors (H.E.S.S. Collaboration, 2011). Up to June 2013, new observations were carried out on HESS J1731−347; table 3.1 summarizes the available observation time on the source. The quoted time is corrected for the variation of the system acceptance (i.e., the variation of the sensitivity to γ-rays with the off-axis angle in the field of view) and for instrument dead-time.

TABLE 3.1: Acceptance-corrected H.E.S.S. observation time on HESS J1731−347.

up to 2007	up to 2009	up to 2013
14 h[(1)]	59 h[(2)]	79.8 h[(3)]

References. (1) Aharonian et al. (2008b); (2) H.E.S.S. Collaboration (2011); (3) Current work.

The TeV results presented in this chapter have been obtained from the analysis of the data collected with the 12 m-diameter telescopes of the H.E.S.S. array up to 2013. Further observations including the 28 m-diameter telescope (CT5) have been taken and analyzed, though no significant emission from the source region has been detected, as expected due to the very limited ($\sim$ 5 h) observation time.

Data analysis

Event direction and energy reconstruction is performed using a moment-based Hillas analysis as described in Aharonian et al. (2006b). "γ-ray like events are selected based on the image shapes with a boosted decision tree method (Ohm, van Eldik, and Egberts, 2009)" (Capasso et al., 2017). The residual background (from hadrons, electrons, and potentially from diffuse γ-ray emission in the Galactic plane) is estimated from source-free regions

[1] https://www.narrabri.atnf.csiro.au/mopra/

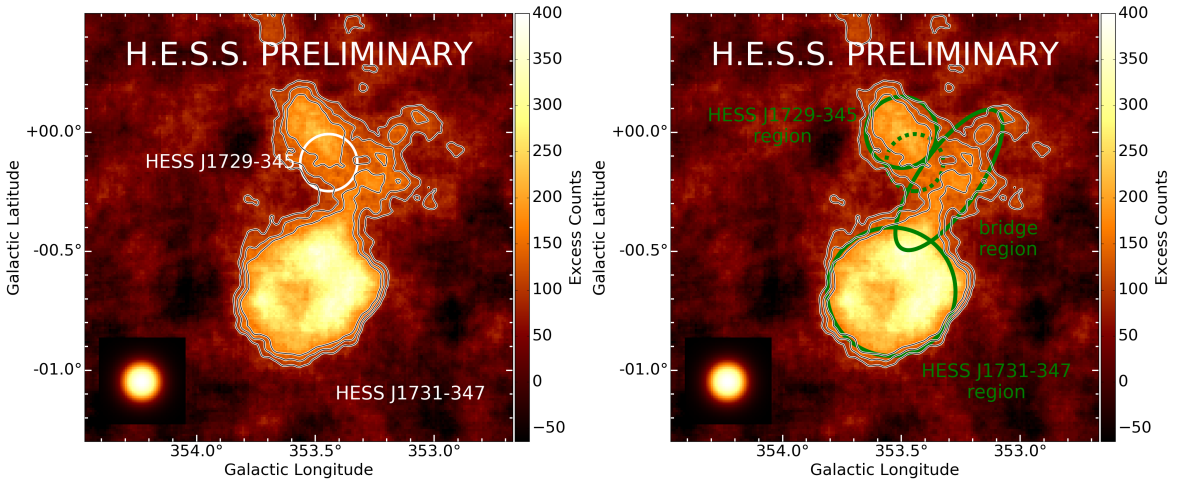

FIGURE 3.2: γ-ray excess counts map of HESS J1731−347 and its surroundings (*left*), correlated with a circular filter with $0.1°$ radius. Overlaid: 3,4,5 sigma significance contours, calculated following Li and Ma (1983); the white circle shows the position and extension of HESS J1729−347 as reported in H.E.S.S. Collaboration (2011). The inlet on the bottom left shows the average PSF for this data set. *Right:* Same as left, with three different emission regions highlighted in green. Except HESS J1731−347, the identification is arbitrary and meant as an *eye-guide* for the discussion presented in this chapter. Excess counts map taken from Capasso et al. (2017)

in the vicinity of the studied sources. For sky maps and the morphological studies using these maps, the background at each sky pixel is estimated from a ring around the pixel position (Berge, Funk, and Hinton, 2007). An adaptive algorithm is applied "to optimize the size of the ring, blanking out known sources or excesses above a certain significance level from the rings (requiring thus an iterative/bootstrapping process) (H.E.S.S. Collaboration et al., 2018b)" (Capasso et al., 2017). Figure 3.2 shows the γ-ray excess counts map of HESS J1731−347 and its surroundings, as derived from the latest available dataset. Enclosed in green are three different regions that can be identified (by eye) on this map:

- **HESS J1731−347 region**. It marks the emission from the SNR: it is centered on the remnant's coordinates reported in H.E.S.S. Collaboration (2011) and has the extension of the outer radius of the best-fit shell ($0.27°$).

- **HESS J1729−345 region**. The analysis presented in this chapter reveals a structure which is slightly off-centered and more extended with respect to the one reported in H.E.S.S. Collaboration (2011). Due to the differences in datasets and analysis softwares, it is not straightforward to demonstrate if and how the two regions are related; nonetheless, the naming is kept for consistency reasons.

- **Bridge region**. In-between HESS J1731−347 and HESS J1729−345 a *new* region can be identified, seemingly linking the two objects. The center and extension of the ellipse enclosing this *bridge* are arbitrary and meant as an *eye-guide* only.

3.1.2 Mopra CO and CS line data

As previously mentioned, it is not easy to clearly attribute the origin of the VHE γ-rays observed from Galactic SNRs to either leptonic or hadronic processes. To this regard, surveys mapping the interstellar medium (ISM) can be exploited to locate the target material where Galactic hadronic CRs could potentially produce GeV-TeV γ-rays. For the work presented in this chapter, CO and CS radio line data collected using the Mopra telescope in Australia are used. More specifically, the sky maps on which the TeV-gas correlation study is performed are integrated intensity maps obtained from spectral data of the J=1-0 transition of ^{12}CO and CS molecules. Details on the observation strategy and data reduction can be found in Maxted et al. (2018), Burton et al. (2013).

3.2 Method description

Figure 3.3 shows integrated intensity maps in the HESS J1731-347 region for the three different velocity ranges in which a signal from CS and CO is detected. At first glance there seems to be a reasonably good spatial correspondence between the CO and CS emission seen at $3.2\,\mathrm{kpc}$ and the TeV emission in the bridge region connecting HESS J1731−347 and HESS J1729−345, i.e., excluding HESS J1729−345 and the SNR itself. On the other hand, while the gas emission of the two other distance ranges falls inside the TeV emission region, the overall correspondence between gas and TeV is less clear and may even be absent.

It is also possible that the morphology observed in γ-rays (from both the bridge and HESS J1729−345) is caused by a superposition of gas-related emission from different distances. However, CS is a tracer of regions with very high particle densities ($\sim 10^4/\mathrm{cm}^3$): the probability that the TeV emission comes from chance superposition of gas at different distances along the line of sight is (at least qualitatively) very low.

If an association of the TeV bridge with the gas emission at $3.2\,\mathrm{kpc}$ could be confirmed, it would support the argument that the SNR is indeed located at a distance of $3.2\,\mathrm{kpc}$ and "that the TeV emission observed in the surroundings of the source could be explained by cosmic ray particles that escape from the SNR and illuminate a nearby molecular cloud" (Capasso et al., 2017).

The aim of this study is to try and quantify numerically the potential correlation of the TeV bridge and the gas emission at $3.2\,\mathrm{kpc}$, or eventually the correlation of other TeV emission regions with other gas portions.

3.2.1 Linear correlation on a grid

The idea is to try and see if there exists a linear correlation between the integrated emission from the points taken on an equispaced grid that encompasses both the TeV and the gas regions of interest, as shown in figure 3.4 for the near-distance solution. Namely, the procedure for a given region of interest is:

1. Take the TeV map and place a grid on it

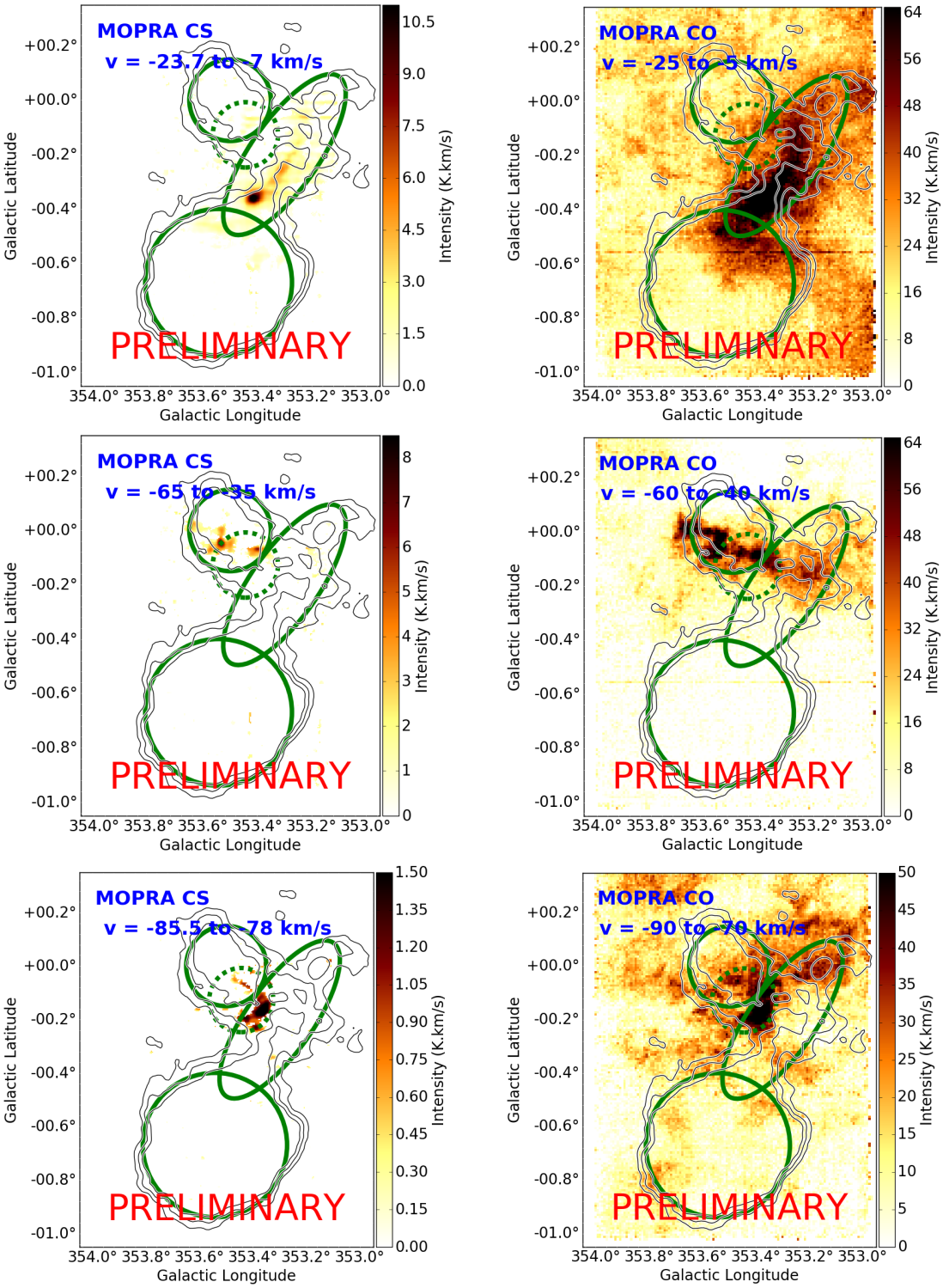

FIGURE 3.3: Integrated intensity maps in the HESS J1731-347 region for the three different velocity ranges in which a signal from CS (*Left*) and CO (*Right*) is detected *Top*: Near-distance solution (3.2 kpc) *Middle*: Mid-distance ($\sim$ 4.5 kpc) *Bottom*: Far-distance solution ($\sim$ 5 $-$ 6 kpc). Overlaid 3,4,5 significance contours from the H.E.S.S. analysis of the source presented in this work. The green circles identify the three TeV emission regions described in 3.1.1; the dashed one marks the position and extension of HESS J1729−345 (H.E.S.S. Collaboration, 2011). CS maps elaborated from Capasso et al. (2017). CO maps obtained by N. Maxted (Maxted et al., 2018).

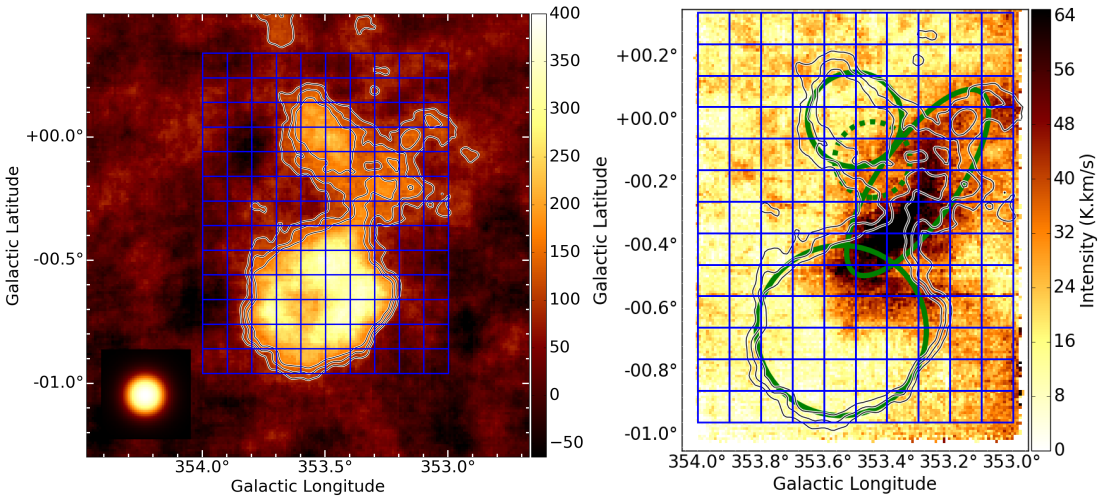

FIGURE 3.4: *Left:* TeV γ-ray excess map from the latest analysis of the source region, smoothed with a Gaussian kernel with size 0.05° for visualization. *Right:* Mopra CO integrated intensity map for the near-distance solution ($\sim 3.2\,\mathrm{kpc}$). Overlaid in blue the $1.3^\circ \times 1.0^\circ$ grid on which the correlation has been tested (0.1° spacing, 13×10 boxes). Excess counts map taken from Capasso et al. (2017). CO maps obtained by N. Maxted (Maxted et al., 2018)

2. Take the Gas map and place the same grid on it

3. Integrate the emission from inside each box on the grid

4. Calculate the correlation coefficient (r) and corresponding p-value (p) for the gas and TeV arrays obtained with the procedure described above. This has been done using Pearson's linear correlation coefficient (Press et al., 1992).

Pearson's coefficient is calculated according to the following formula

$$r = \frac{\sum_i (x_i - \overline{x})(y_i - \overline{y})}{\sqrt{\sum_i (x_i - \overline{x})^2}\sqrt{\sum_i (y_i - \overline{y})^2}} \tag{3.1}$$

where x_i and y_i are the integrated emission from each box taken on the TeV and the gas sky map respectively. $\overline{x}$ is the mean of the x_i's, $\overline{y}$ is the mean of the y_i's.

r can range from -1 to +1, in the ideal case of a *complete negative correlation* and a *complete positive correlation* respectively.

However, r alone is not sufficient to make a clear statement on the strength of the correlation between x and y, as it holds no information on their individual distributions. For this reason, any value of r should be given together with an estimate of the probability p (*p-value*) that a *truly* correlated system could produce a dataset with a value of r at least as extreme. In other words, the lower p is, the more unlikely would be for an uncorrelated set of x and y to produce by chance a value of r at least as *good*.

For this specific study, the case that would *prove* a correlation between the TeV and one (or more) gas emission regions, would be the one with r as close as possible to 1 and low p.

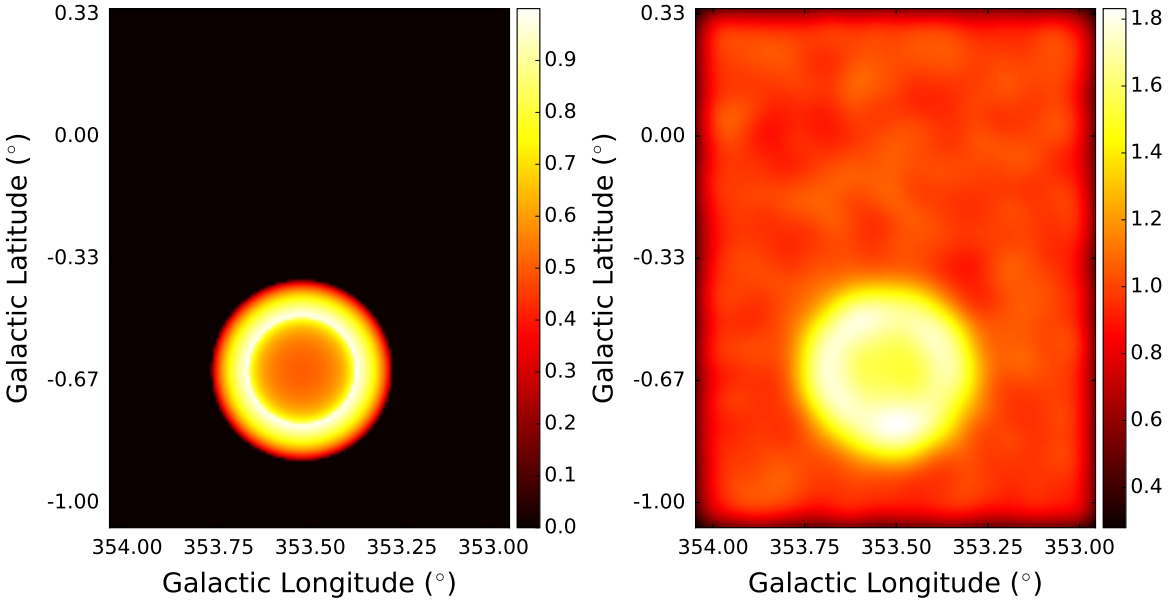

FIGURE 3.5: *Left*: Sky map of the shell model on which the correlation method is tested. The shell center coordinates (l_0, b_0) and $R_{\rm in}$, $R_{\rm out}$ are HESS J1731−347 best-fit parameters; the peak amplitude is arbitrarily set to 1. *Right*: Sky map of the shell model, after Poisson noise is added to each bin, according to the *background-acceptance* per pixel. The map is smoothed with a Gaussian kernel of $0.05°$ for visualization.

3.2.2 Validation of the method

In order to check whether the method would be effective to detect a correlation (in case present) some tests have been conducted. The idea is to produce maps which are *truly* correlated, add *some* noise to them and see what happens when the correlation on a grid is probed as described above.

As test case, a shell model (as described by equation 2.1) is considered. The shell center coordinates (l_0, b_0) and $R_{\rm in}$, $R_{\rm out}$ are HESS J1731−347 best-fit parameters; the peak amplitude is arbitrarily set to 1. Figure 3.5 (left panel) shows the sky map of the built model; this sky map represents the ideal case in which only *true* γ-rays from the source of interest are detected. In order to mimic a more realistic situation, noise is added to each bin of the map; the noise value is randomly extracted from a Poissonian distribution with mean λ_i, where i runs over the bins. λ_i is set according to the *background-acceptance* per pixel, i.e., the background events mis-identified as γ-rays at pixel i (see Figure 3.5, right panel).

In order to study the influence of the grid choice on the correlation test outcome (i.e., on r and p), the following procedure is applied. Starting from the bottom of the map and moving towards the top, grid rows are sequentially added until the entire map is covered (the side of a single grid box is $0.1°$). For each of these grids, the correlation between pairs of maps is tested; while the underlying source model stays the same, the noise component is randomly sampled and thus different in each map. Figure 3.6 shows three examples of grids on which the correlation between two maps is sampled.

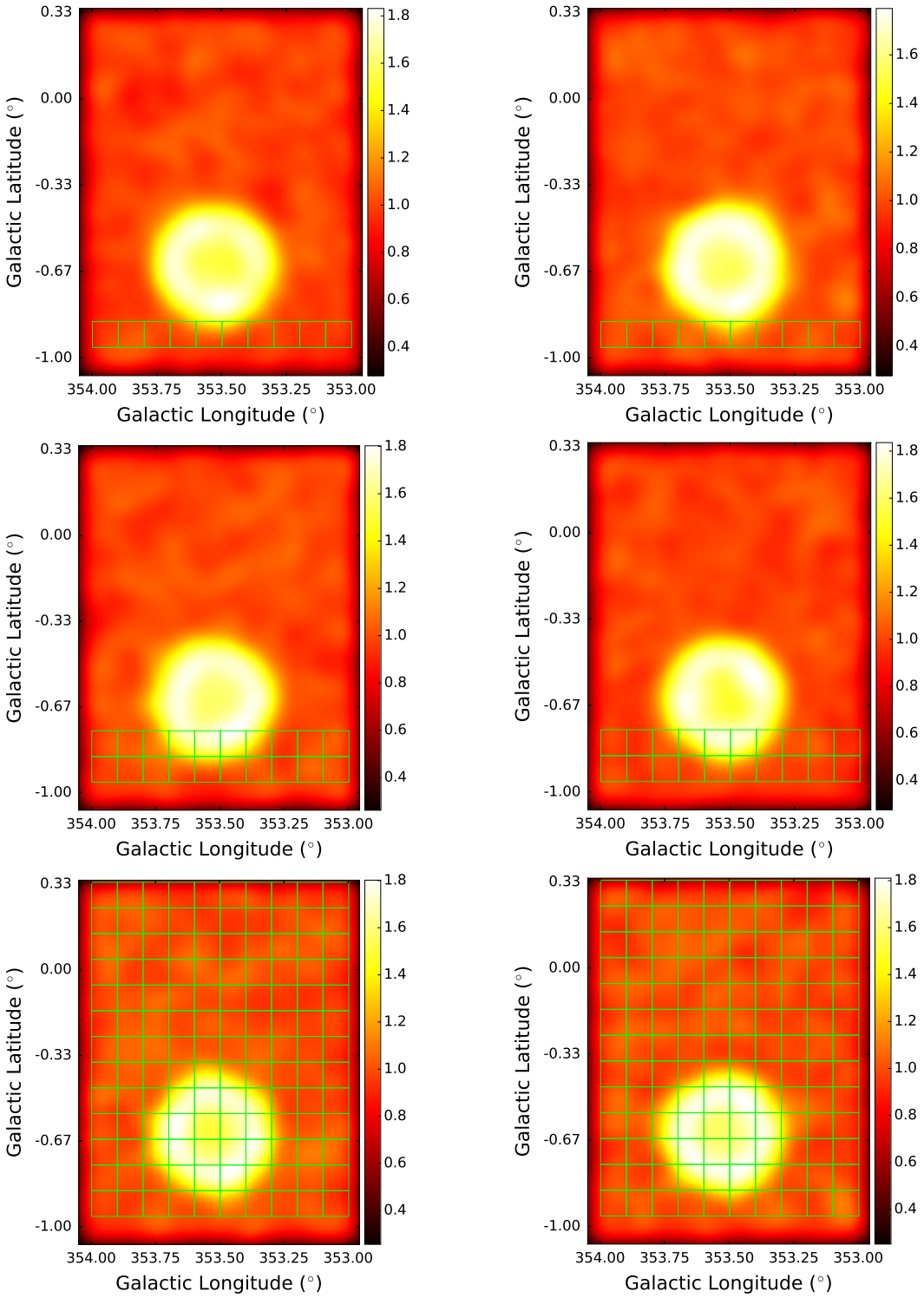

FIGURE 3.6: Examples of grids on which the correlation is tested; the side of each grid box is $0.1°$. *Top*: 1×10 grid. *Middle*: 2×10 grid. *Bottom*: 13×10 grid. Each of the maps has a different noise, randomly sampled from a Poisson distribution that follows the *background-acceptance* per pixel; a Gaussian kernel of $0.05°$ is applied for visualization.

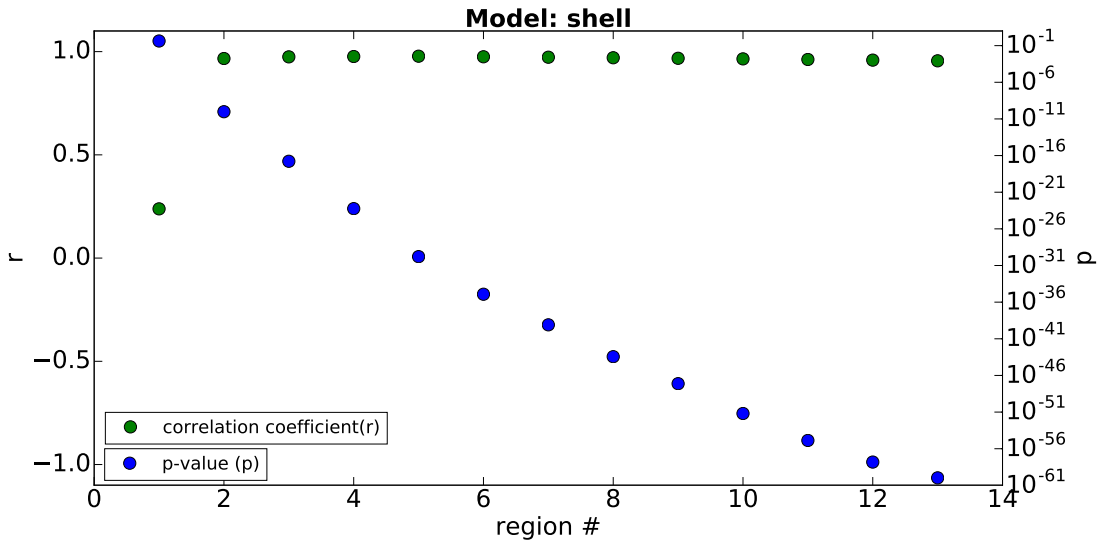

FIGURE 3.7: Correlation coefficient (r) and null-hypothesis probability (p) for the shell model (mean over 5000 iterations).

TABLE 3.2: Correlation coefficient (r) and null-hypothesis probability (p) for the shell model (mean over 5000 iterations).

region #	region size	r	p
1	1×10	2.38e-01	4.30e-01
2	2×10	9.67e-01	9.67e-11
3	3×10	9.75e-01	1.66e-17
4	4×10	9.76e-01	5.77e-24
5	5×10	9.78e-01	1.62e-30
6	6×10	9.75e-01	1.20e-35
7	7×10	9.73e-01	8.05e-40
8	8×10	9.70e-01	3.64e-44
9	9×10	9.68e-01	7.55e-48
10	10×10	9.65e-01	6.41e-52
11	11×10	9.62e-01	1.34e-55
12	12×10	9.59e-01	1.51e-58
13	13×10	9.56e-01	1.06e-60

This procedure is repeated over 5000 pairs of maps, each having a different noise generation. The average correlation coefficient r and respective p-value per grid are then extracted. The results are reported in Table 3.2 and plotted in Figure 3.7.

As it can be noted, in case an underlying *true* correlation is present, the highest value of the correlation coefficient is reached when the source is completely contained inside the grid (region 5×10). Adding more grid points slightly worsens r, but the p-value decreases: this might be due to the fact that noise grid points artificially boost the strength of the correlation in a limited ROI, although they provide no additional information on the correlation itself (i.e., on r) Having this limitation in mind, it is important to observe that, if the emissions in the two maps were really correlated, this method would be able to detect it.

Cut on correlation grid points

As previously mentioned, after having reached the maximum value of r, it seems unnecessary to further add test grid points. Moreover, the optimal r seems to be obtained when the source region is completely covered by the grid on which the correlation is tested. One way to avoid the *artificial* decrease of the p-value could then be to cut on the noise-to-noise correlation points by setting a threshold on the integrated emission from the boxes. In order to verify this hypothesis, the following test is conducted:

- as starting point, the grid covering the whole sky area is selected. This choice is motivated by the trivial observation that any correlation (if present) must be within the available map.
- on the first of the maps with noise, the maximum value of the integrated emission from the grid boxes is evaluated; then, grid points in which the integrated emission is below 60% of the maximum are discarded (the threshold is arbitrarily set, see Figure 3.8, right panel).
- the mean r and p on the reduced grid are calculated and compared to the ones obtained on the whole 13×10 grid.

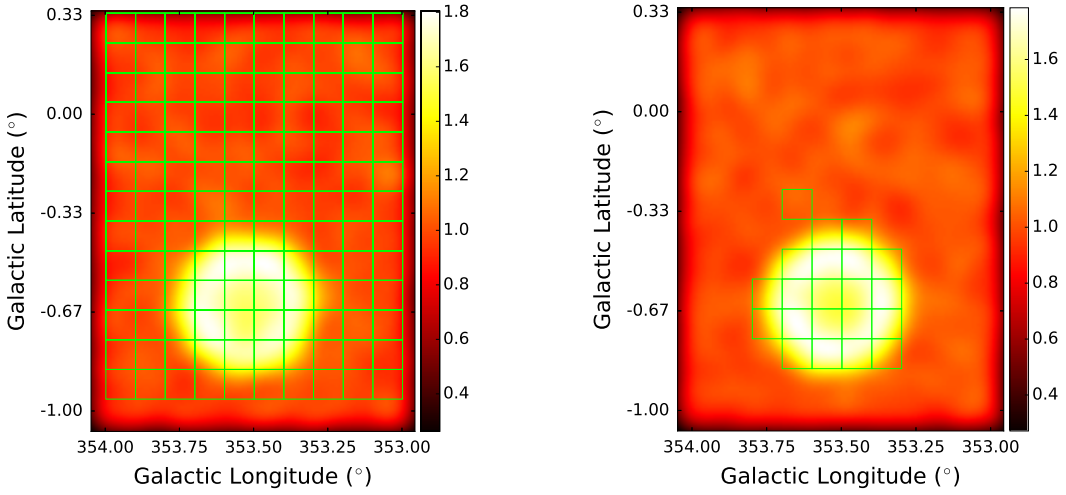

FIGURE 3.8: *Left:* 13×10 grid overlaid on the simulated shell sky map. *Right:* Grid boxes in which the integrated emission is above 60% of the maximum; this choice allows to still cover the source, while reducing the amount of noise-to-noise grid points.

For the correlation tested on the reduced grid, the obtained mean values of r and p are 9.6×10^{-1} and 1.37×10^{-10} respectively. By looking at the corresponding results for the 13×10 grid, it can be observed that r is almost unaffected by the cut and the correlation is still correctly identified (though the p-value is dramatically increased). For this reason, the studies performed in the following sections have been conducted on a reduced grid, after a cut on the integrated gas emission.

3.3 Correlation results and physical interpretation

As discussed e.g., in Acero et al. (2013), massive molecular clouds are of great interest in the astrophysical community, as they provide the target material where CRs can interact and eventually produce γ-rays as a result of hadronic interactions. In this sense, MCs can be exploited to locate the potential accelerators of Galactic CRs.

The aim of the study presented in this chapter is to try and quantify numerically a possible correlation between the TeV *bridge* and the gas emission at $3.2\,\mathrm{kpc}$. If proven, such correlation would lend support to the picture proposed in Cui, Pühlhofer, and Santangelo (2016), where CRs accelerated at HESS J1731−347 shock-fronts reach the nearby MC and illuminate it.

On the other hand, there is the possibility that the TeV γ-rays *outside* the remnant are the result of hadronic interactions taking place between background CRs (i.e., with no nearby accelerator) and MCs along the line of sight. In this case, such MCs are called *passive*.

In the following sections, both scenarios are considered and discussed; the correlation study between TeV and CO maps is presented.

3.3.1 Background Cosmic Rays illuminating passive molecular clouds

In order to probe the passive MCs illumination scenario, under the assumption of a constant sea CRs density, one needs to check whether the TeV emission (excluding the remnant) correlates with the integrated gas intensity along that direction. First, the emission from HESS J1731−347 has been modeled with a shell uniformly radiating between inner and outer radius and subtracted, as shown in Figure 3.9.

Then, the gas emission from the three distance solutions has been stacked. Finally, following the procedure described in Section 3.2.1 and 3.2.2, the linear correlation between the residual TeV and gas maps has been probed on the grid shown in Figure 3.10.

Figure 3.11 shows the correlation plot between the SNR-subtracted TeV and the stacked gas emission: both r (0.54) and p (1.5×10^{-5}) seem to indicate a good matching. Since the gas is at different distances, such a correlation could indeed support the hypothesis of passive MCs illumination.

3.3.2 Escaping Cosmic Rays illuminating nearby molecular clouds

A schematic representation of the nearby MC illumination is depicted in Figure 3.12. In this scenario, the *bridge* geometry results from a superposition of gas-related emission from CRs escaping the remnant shock-front. In order to probe such scenario, the correlation between the TeV and gas emission from the nearest distance ($3.2\,\mathrm{kpc}$) is tested on the grid shown in Figure 3.13.

As it can be noted from the plot in Figure 3.14, also in this case there seems to be a good correlation between the two emissions ($r = 0.4$, $p = 2.4 \times 10^{-3}$), though slightly weaker in terms of p-value. It should be remarked that the VHE γ-rays seen from the remnant's region

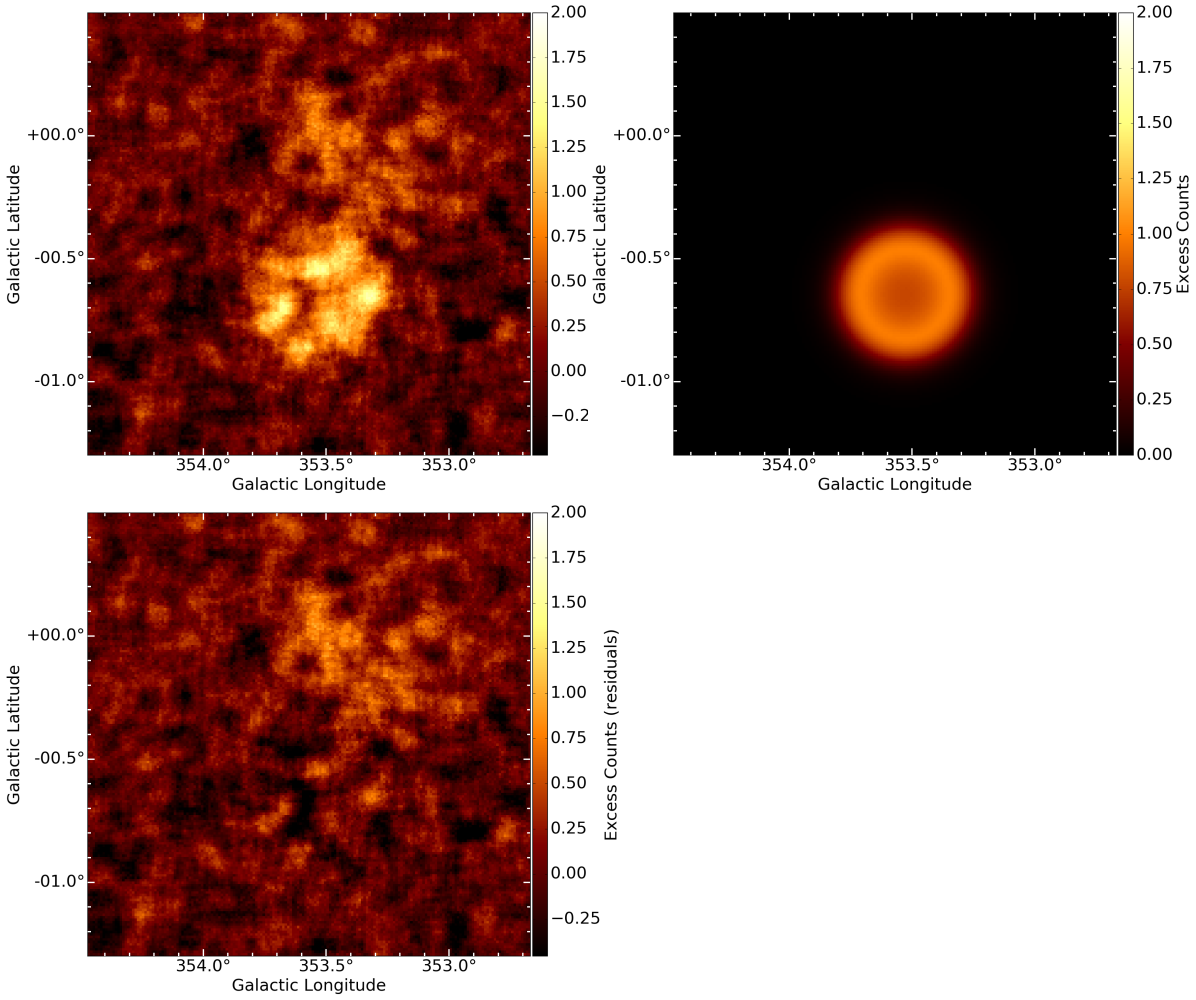

FIGURE 3.9: *Top left:* Residual TeV excess counts after background-only fitting of HESS J1731−347 sky region, smoothed with a top-hat filter with 0.05° radius for visualization. *Top right:* HESS J1731−347 shell model. *Bottom left:* Residual TeV excess counts after subtraction of the modeled emission from HESS J1731−347, smoothed with a top-hat filter with 0.05° radius for visualization.

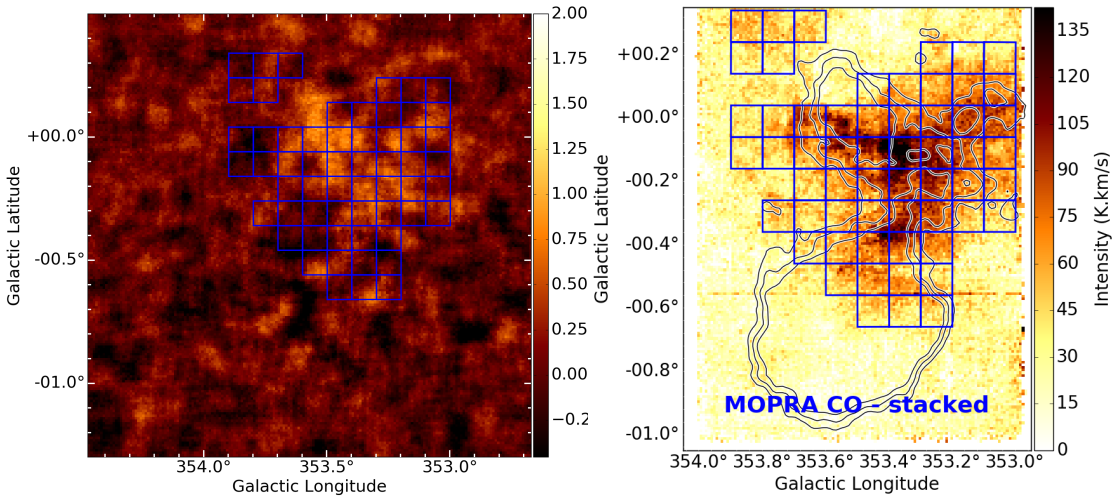

FIGURE 3.10: *Left:* TeV excess-count map from the latest source analysis, after subtraction of the modeled emission from HESSJ1731-347, smoothed with a top-hat filter with size 0.05° for visualization. *Right:* Mopra stacked CO emission. Overlaid in blue the grid on which the correlation has been tested for this particular case ($0.1^\circ \times 0.1^\circ$ boxes, > 30% maximum gas emission). CO maps obtained by N. Maxted (Maxted et al., 2018).

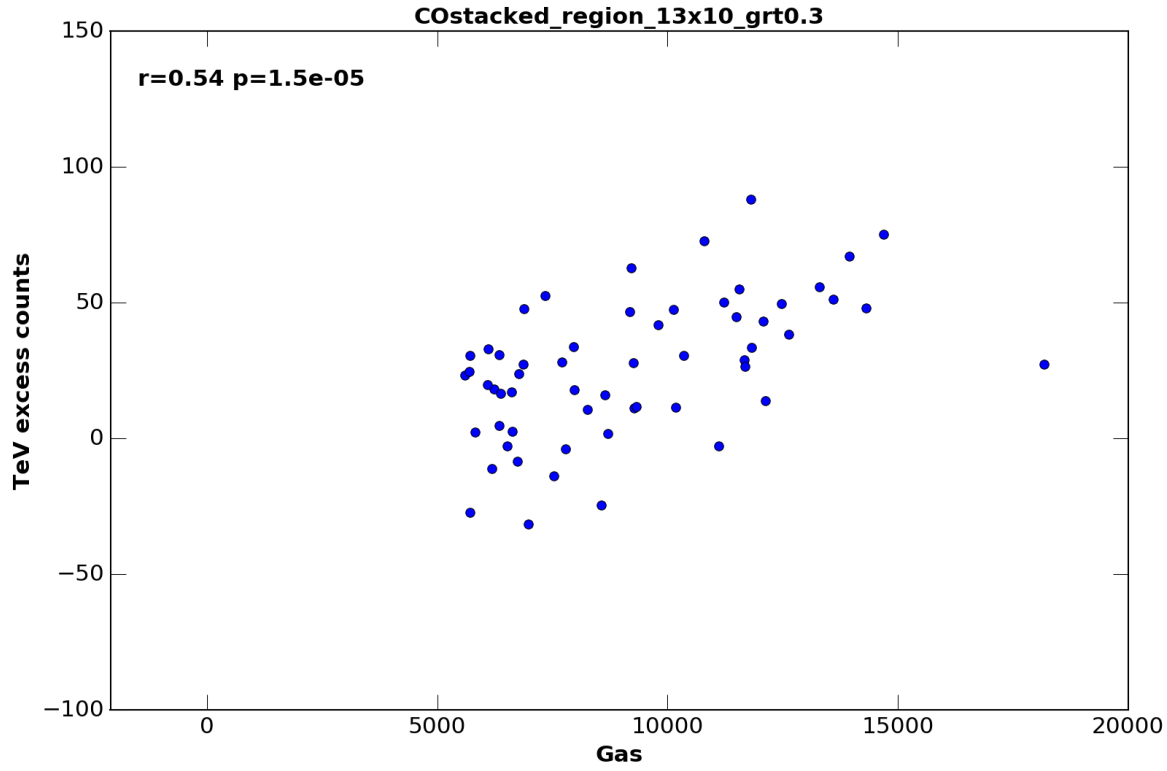

FIGURE 3.11: Integrated gas (x) and TeV (y) emission from the grid boxes shown in Figure 3.10.

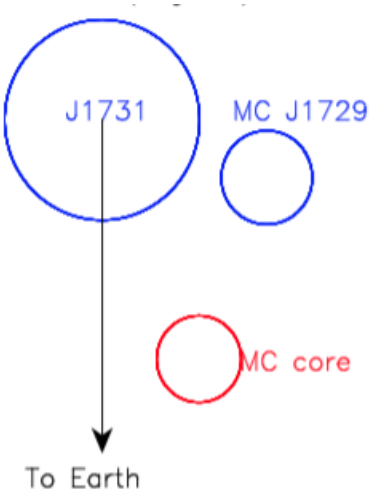

FIGURE 3.12: Schematic view (from above the Galactic Plane) of the nearby MC illumination scenario. Picture taken from Cui, Pühlhofer, and Santangelo (2016).

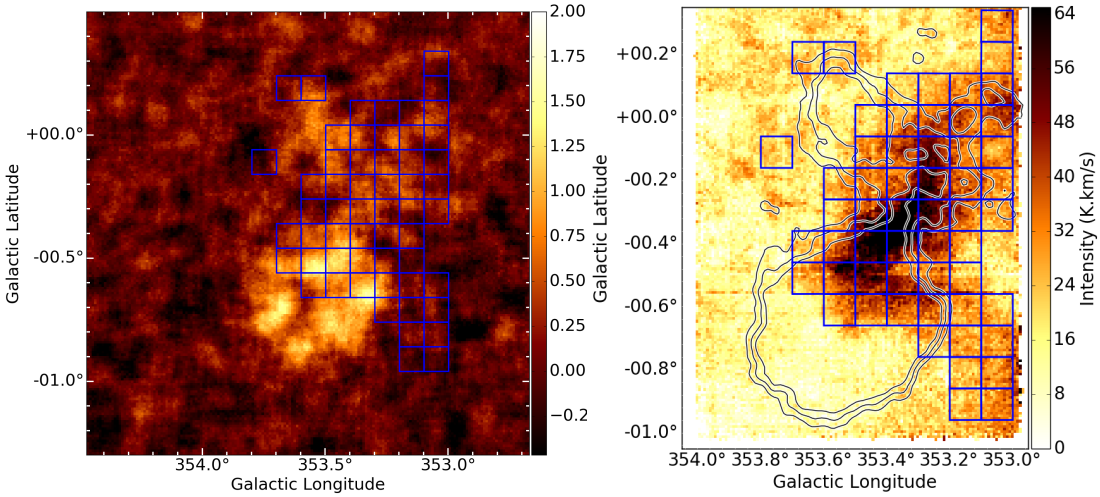

FIGURE 3.13: *Left:* TeV excess-count map from the latest H.E.S.S. analysis, smoothed with a top-hat filter with size $0.05°$ for visualization. *Right:* Mopra integrated intensity map for the near ($\sim 3.2\,\mathrm{kpc}$) distance solution. Overlaid in blue the grid on which the correlation has been tested for this particular case ($0.1° \times 0.1°$ boxes, > 30% maximum gas emission). CO map obtained by N. Maxted (Maxted et al., 2018).

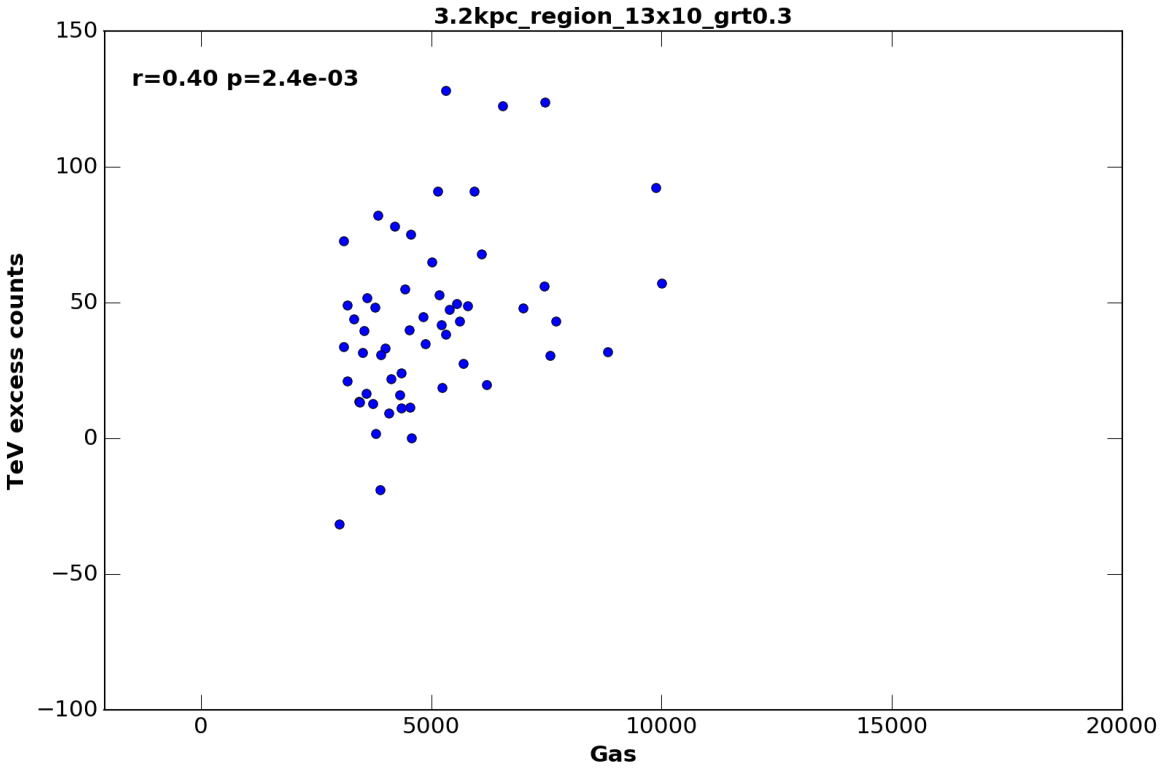

FIGURE 3.14: Integrated gas (x) and TeV (y) emission from the grid boxes shown in Figure 3.13.

TABLE 3.3: Correlation coefficient (r) and null-hypothesis probability (p) for the grid tested at different distances

distance	r	p
stacked	0.54	1.5×10^{-5}
$3.2\,\mathrm{kpc}$	0.40	2.4×10^{-3}
$4.5\,\mathrm{kpc}$	0.37	7.6×10^{-2}
$5-6\,\mathrm{kpc}$	0.19	1.8×10^{-1}

could be a blend of both hadronic (from the interaction with the gas) and leptonic processes. The method outlined in this chapter does not take into account this possibility.

Table 3.3 summarizes the results of the correlation study for the other distance solutions: for the gas seen at $4.5\,\mathrm{kpc}$ and $5-6\,\mathrm{kpc}$ there is no strong numerical indication of correspondence between gas and TeV.

3.3.3 Expected γ-ray flux: a hadronic scenario

Starting from the available gas maps, it is possible to estimate the expected γ-ray flux from hadronic processes only; in this way, the local accelerator scenario and the one where passive MCs are illuminated by background CRs can be compared.

Following the arguments proposed in Kelner, Aharonian, and Bugayov (2006), the γ-ray flux from π^0-decay after $p-p$ interactions, can be calculated with the equation

$$\Phi_\gamma\left(E_\gamma\right) = cn_H \int_0^1 \sigma_{inel}\left(E_\gamma/x\right) J_p\left(E_\gamma/x\right) F_\gamma\left(x, E_\gamma/x\right) \frac{dx}{x} \tag{3.2}$$

where

- c is the speed of light
- n_H is the column density of ambient hydrogen, which can be derived from the CO intensity using the conversion factor proposed in (Nakanishi and Sofue, 2006): $X = 1.4 \times 10^{20} e^{(R/11\,\mathrm{kpc})} \left[\mathrm{cm^{-2}K^{-1}km^{-1}s}\right]$ (R being the distance to the Galactic Center.)
- $x = E_\gamma/E_p$ is the ratio between the observed γ-ray and the incident proton
- σ_{inel} is the inelastic cross-section of $p-p$ interactions
- F_γ represents the total spectrum of γ-rays, as expressed by Eq. 58 in Kelner, Aharonian, and Bugayov (2006).

J_p is the proton flux measured at the top of Earth's atmosphere, below $10^6\mathrm{GeV}$. In this approximation, the flux at any location in the Galaxy (with no nearby accelerator) is assumed to be the same as the local one.

By integrating Equation 3.2, one can build an expected integral γ-ray flux map starting from a known CO distribution; figure 3.15 shows the result of this exercise for the CO integrated intensity maps at different distances, and for the stacked case. As it can be observed, the fluxes that one would derive from the interaction of background CRs with the observed MCs are rather low, about one order of magnitude lower than the minimum detected flux in the HESS J1731−347 region ($\sim 10^{-9}\mathrm{m^{-2}s^{-1}}$). Also, since $F_\gamma \propto d^{-2}$ (being d the distance to the observer) it is clear that, in the stacked case, most of the contribution comes from the gas at $3.2\,\mathrm{kpc}$.

However, in the presence of a nearby accelerator (like e.g., HESS J1731−347) it is reasonable to assume an enhancement of the expected γ-ray flux from hadronic interactions up to the observed values.

3.3.4 Conclusions

The work presented in this chapter has proposed a simple method for the numerical quantification of the correlation between emission profiles at different wavelengths. More specifically, the aim of the study was to try and calculate the correlation between the TeV emission from the SNR HESS J1731−347 and its surroundings and the emission from gas clouds at different distances.

Two main scenarios have emerged:

- the VHE emission from outside the remnant could be caused by the interaction between background CRs and MCs at different distances. Despite being the most significant possibility from the presented method's point of view ($\mathrm{r} = 0.54$ $\mathrm{p} = 1.5 \times 10^{-5}$),

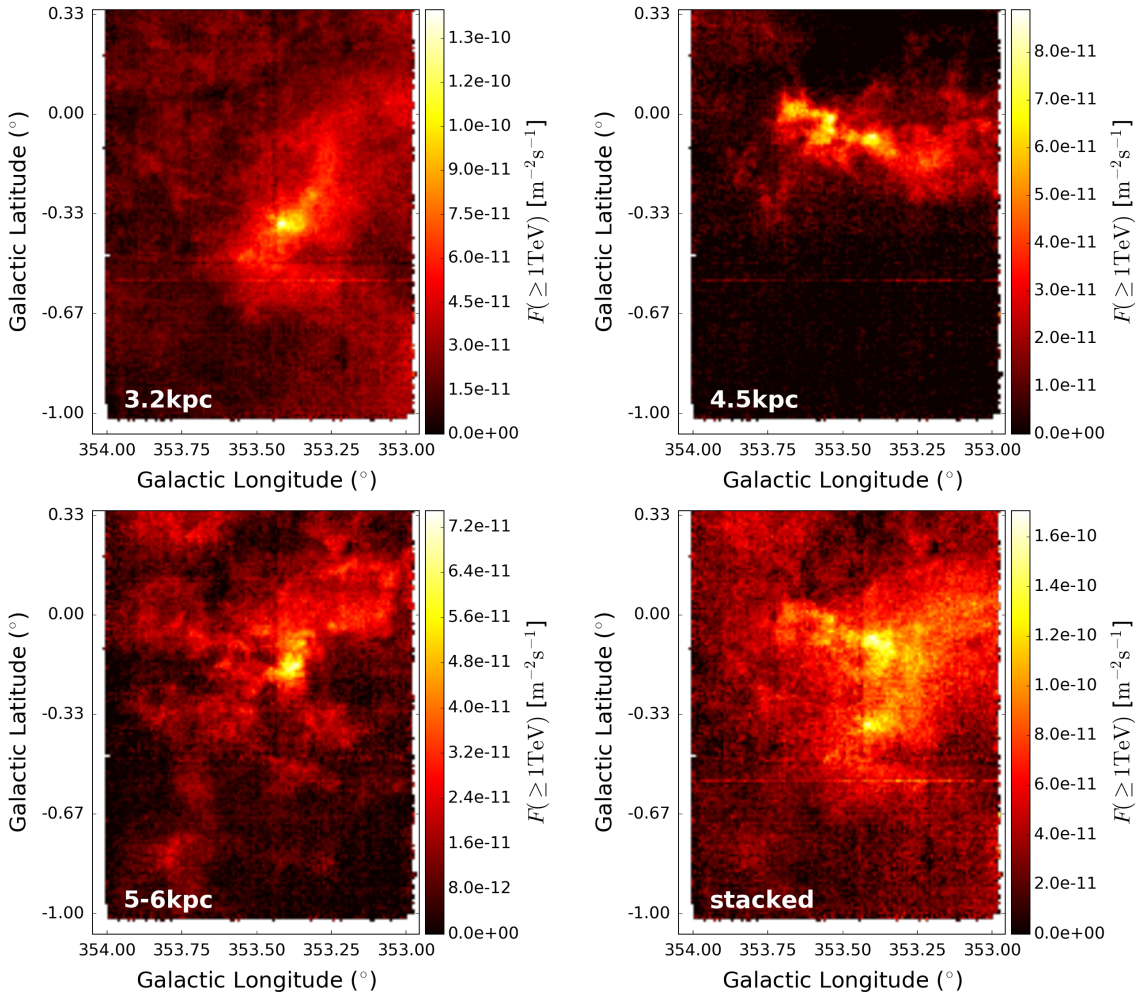

FIGURE 3.15: Expected γ-ray flux maps, obtained from the CO gas emission at different distances, under the assumption of illumination from background CRs.

the expected γ-ray flux from such interactions is not high enough to justify the actually observed one

- the VHE emission from the TeV *bridge* shows a good correlation with the gas seen at $3.2\,\mathrm{kpc}$; though being weaker than the previous correlation in terms of p-value ($\mathrm{p} = 2.4 \times 10^{-3}$), it lends support to the picture where CRs escape from the remnant's shell and illuminate nearby MCs, as proposed in Cui, Pühlhofer, and Santangelo (2016), but the improvement of p-value when looking at the entire map is unexplained.

Therefore, none of the two scenarios could be firmly confirmed by the presented analysis; nonetheless, the method itself should be able to detect a *true* correlation, in case present. New TeV observations of the source region, possibly with more powerful instruments like CTA, could help in the future to shed light on the actual origin of the VHE emission from the remnant region; also, an X-ray map highlighting the synchrotron radiation from HESS J1731−347 could be used as template to correlate the TeV photons to leptonic emission scenarios.

Chapter 4

FlashCam: a fully digital Cherenkov camera for CTA

4.1 Towards the future of ground-based γ-ray astronomy: the Cherenkov Telescope Array

As briefly outlined in Chapter 1, the Cherenkov Telescope Array will be the next-generation IACT system to probe the VHE Universe, in the energy range from $20\,\mathrm{GeV}$ to about $300\,\mathrm{TeV}$.

It will consist of two arrays of IACTs located in two different sites:

- CTA *North* will be hosted by the Observatorio del Roque de los Muchachos in Villa de Garafia on the Canary Island of La Palma
- CTA *South* will be located about $10\,\mathrm{km}$ southeast of European Southern Observatory's (ESO) in the Atacama Desert in Chile.

The overall array system will consist of telescopes with three dish sizes, giving access to different bands of the energy range covered by CTA:

- Large-Sized Telescopes (LSTs), to cover the lowest energies accessible to CTA (below $100\,\mathrm{GeV}$)
- Medium-Sized Telescopes (MSTs), for the core energy range
- Small-Sized Telescopes, aimed at catching the highest energy (supra-TeV) photons.

Figure 4.1 shows the proposed layouts for the northern and southern arrays. The northern array will cover an area of about $600\,\mathrm{m}^2$, featuring 4 LSTs and 15 MSTs that will focus on the low- and mid-energy ranges, from $20\,\mathrm{GeV}$ to $20\,\mathrm{TeV}$. On the other hand, the southern array will deploy 4 LSTs and 25 MSTs, and will additionally feature 70 SSTs, thus spanning CTA's entire energy range.

Among the most significant technical goals, CTA aims at improving the sensitivity of current VHE instruments by an order of magnitude at $1\,\mathrm{TeV}$, enlarge the detection area to access higher photon rates for probing short-timescale phenomena, improve imaging capabilities of extended sources by increasing angular resolution and field of view.

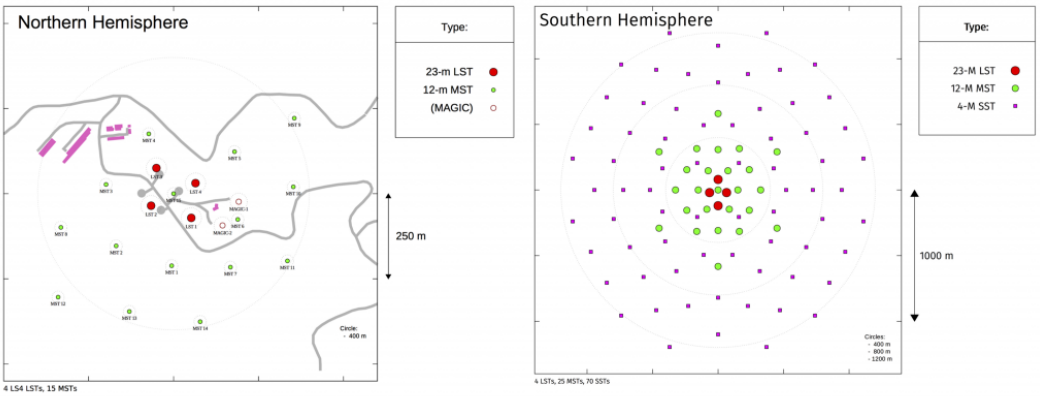

FIGURE 4.1: Proposed telescope layouts for CTA's northern and southern arrays. *Source*: https://www-cta-observatory.org/science/cta-performance

Concerning the science topics that CTA envisages to address, understanding the origin of Cosmic Rays plays a crucial role. As already outlined in the previous chapters, the current-generation GeV-TeV instruments have demonstrated their capability to locate the most powerful Galactic accelerators, providing evidence for the origin of the γ-ray emission from some of them (Ackermann et al., 2013).

However, the question whether Galactic SNRs can account for the bulk local CRs, as well as the question about the possible location of Pevatrons, are still lacking a definitive answer.

To this aim, surveys of the Galactic Plane in VHE γ-rays are of strategic importance to perform a census of particle accelerators and precision measurements of archetypal sources (like e.g. RX J1713.7−3946). As demonstrated in Chapter 2, the surveying capabilities of current-generation IACTs allowed the discovery of new SNRs in the Galactic Plane. With the potential of the full CTA array, a factor of 10-20 in improved sensitivity will be possibly achieved, leading to many hundreds (∼300-500 in the Galactic Plane) of detected sources. Figure 4.2 shows a simulated image of the possible outcome of CTA's Galactic Plane Survey, in the region from $l = 90°$ to $270°$.

Other key science topics for CTA include the investigation of extreme environments such as black holes and jets, the relativistic outflows from neutron stars and the search for Dark Matter. A complete review of CTA's science goals can be found in Cherenkov Telescope Array Consortium et al. (2017).

Within CTA, two camera concepts for the MSTs are currently in development: the NectarCAM (Glicenstein and Shayduk, 2017) and the FlashCam, in which the University of Tübingen is involved.

In the following sections, a brief overview of the FlashCam project (Puehlhofer et al., 2015) will be introduced, along with the results from a preliminary analysis of calibration data from a prototype camera.

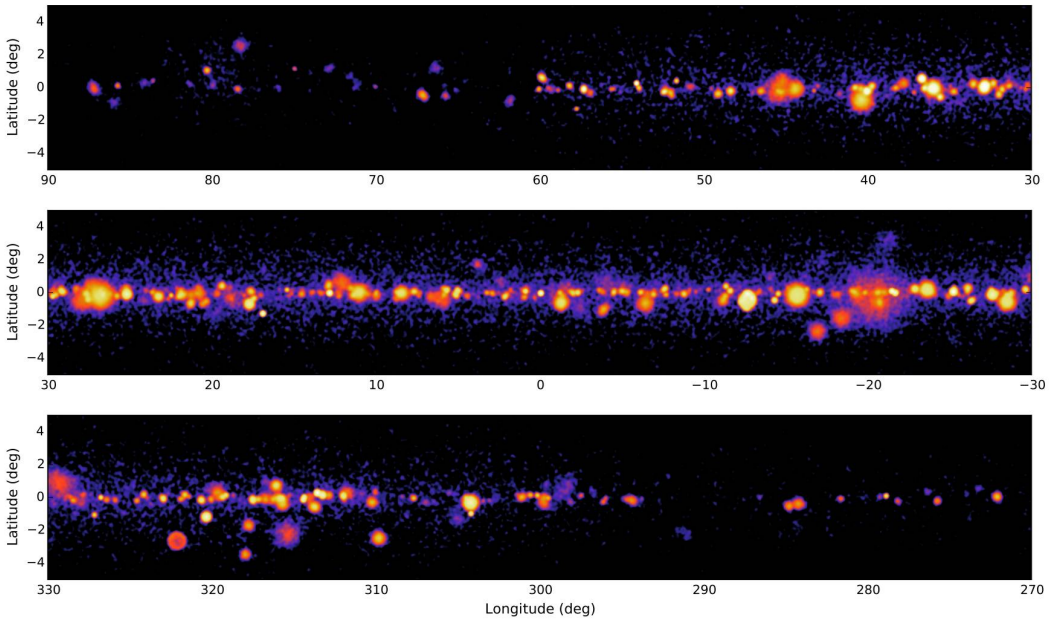

FIGURE 4.2: Simulated image of the CTA Galactic Plane Survey, in the region from $l = 90°$ to 270°. The adopted source model includes both PWNs and SNRs (the most populated source classes in current VHE surveys) and diffuse emission. *Source*: https://www-cta-observatory.org/science/cta-performance

4.2 The FlashCam concept

FlashCam is the first prototype of a Cherenkov camera implementing a fully-digital readout and triggering processing. It develops over a modular architecture, as schematically depicted in Figure 4.3.

FlashCam's three main building blocks are:

- the Photo Detection Plane (PDP)
- the Readout System (ROS)
- the camera server for data acquisition (DAQ)

The PDP consists of 1764 pixels, organized in modules with 12 PMTs each, arranged in a hexagonal structure with $50\,\mathrm{mm}$ spacing. Every module is equipped with high voltage (HV) supply, preamplifiers and a CAN bus interface for slow control and safety purposes.

FlashCam runs in two different regimes, according to the amount of light impinging on the camera. Up to a few hundred photoelectrons, the amplifiers' response is linear with respect to the signal amplitude; above ∼250 p.e., the signal is clipped in a controlled way, i.e., the integral of the signal grows logarithmically with the input charge (Werner et al., 2017; Gadola, 2013). In this configuration, the dynamic range can be extended up to ~ 3000 p.e. without the need for a second, low-gain channel.

The analog signals from the modules are transmitted to the ROS via cat. 6 cables and continuously sampled with 12-bit FADCs at $250\,\mathrm{MS/s}$. The acquired samples are buffered

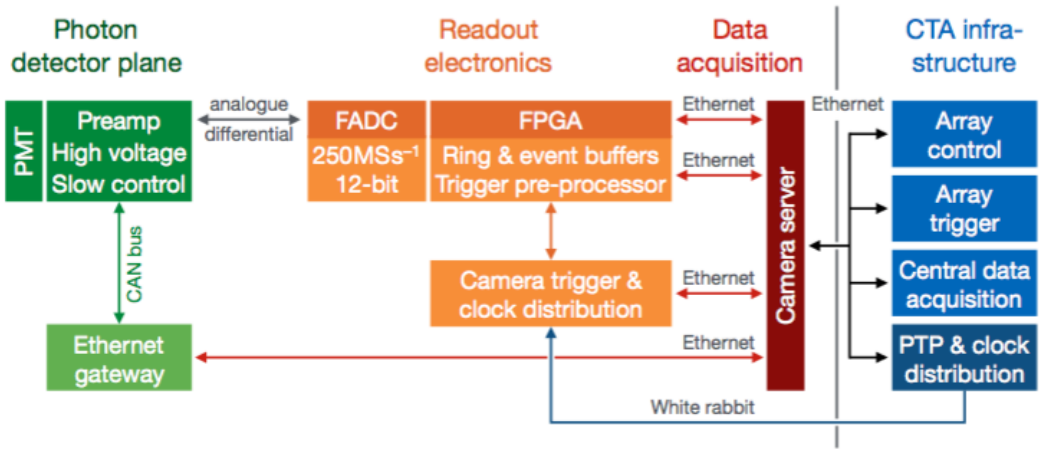

FIGURE 4.3: Schematic view of FlashCam's building blocks (Werner et al., 2017).

in FPGAs and can be processed according to configurable triggering schemes. The data are then sent to the camera server via Ethernet cables and processed.

The following section will present a preliminary verification of FlashCam 720-pixels prototype's performances in the linear amplification regime.

4.3 Study of the 720-pixel prototype calibration data

During the summer 2016, an extensive measurement campaign on the 720-pixels FC prototype was carried out at the Max-Planck-Institut für Kernphysik (MPIK) in Heidelberg. The aim was to verify the camera's performances under realistic operational circumstances, e.g. under pulsed light illumination and varying temperature. In this section, a preliminary analysis of the collected data is outlined; more specifically, the baseline, gain and timing drift with temperature, at different light intensities, are investigated.

A schematic representation of the measurement setup is shown in Figure 4.4. The light source consists of a $355\,\mathrm{nm}$ laser, operated in pulsed mode. The laser is equipped with a programmable OD4 filter wheel; the light intensity (i.e., the number of photons per pulse shone on the camera) can be adjusted by changing the position of the wheel. The acquisition is performed synchronously to each laser pulse: for every cycle, 10000 $\sim 2\,\mu\mathrm{s}$-long waveforms are read-out from the active pixels. Each cycle is repeated over 31 temperatures in the range $5 - 35\,^{\circ}\mathrm{C}$, at a fixed position of the filter wheel (640, 896, 1472, 1856, 2240)

The camera was equipped with 60 photo detector plane (PDP) modules with 12 PMTs each. In this configuration, two PMT variants were still under testing: Hamamatsu R12992-100 with 7 dynodes and Hamamatsu R11920-100 with 8 dynodes, evenly distributed on the detector plane.

The analogue signal from each pixel is sampled with 12-bit FADCs with a rate of $250\,\mathrm{MS\,s^{-1}}$[1] and post-processed off-line in order to extract all the needed parameters. An example of the off-line analysis chain is shown in Figure 4.5: first, the digitized signal (black

[1] $512\,\mathrm{S/trace} \times 4\,\mathrm{ns/S} = 2048\,\mathrm{ns/trace}$

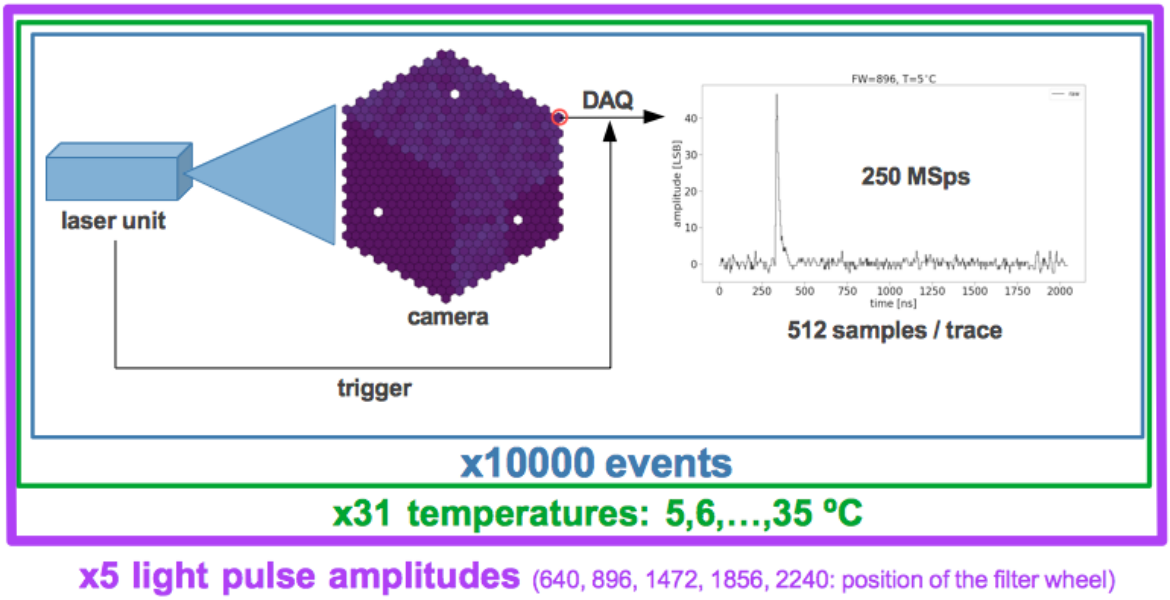

FIGURE 4.4: Schematic representation of the experimental setup used for testing the 720-pixel FC prototype.

solid line) is up-sampled from $250\,\mathrm{MS\,s^{-1}}$ to $1\,\mathrm{GS\,s^{-1}}$ and smoothed with a sliding moving average (SMA) filter of 4 samples (blue stars). The long tail following the peak is caused by the PMT's load resistor; in order to eliminate it, the signal is differentiated. Such operation introduces an undershoot, which is then compensated by adding a portion of the original signal to the differentiated one, as analytically described by the following formula:

$$g\left(t\right) = \frac{\mathrm{d}f\left(t\right)}{\mathrm{d}t} + p \times f\left(t\right) \tag{4.1}$$

where p ranges between 0 and 1. A detailed description of the post-processing algorithm is provided in Gadola (2013). The results presented in this section are extracted from the post-processed waveforms.

4.3.1 Baseline stability

As previously mentioned, for a fixed filter wheel position and temperature, a measurement cycle consists of 10000 acquisitions triggered by a laser pulse. For a given channel, the baseline before each pulse is evaluated and placed in an histogram; an example of the resulting distribution is shown in Figure 4.6, for three different temperatures; the mean and sigma after a Gaussian fit to the data are then extracted. Afterwards, the shift with respect to the mean at $20\,^{\circ}\mathrm{C}$ is estimated. Figure 4.7 shows the drift with temperature of the baseline shift at a fixed position of the filter wheel, for one of the camera's channels and for all the active channels (*top* and *bottom* respectively).

Finally, the baseline drift of each channel (expressed in LSB/K) is estimated as the slope of a linear fit to the data shown in Figure 4.7. As illustrated in Figure 4.8, 7- and 8-dynodes PMTs show comparable performances.

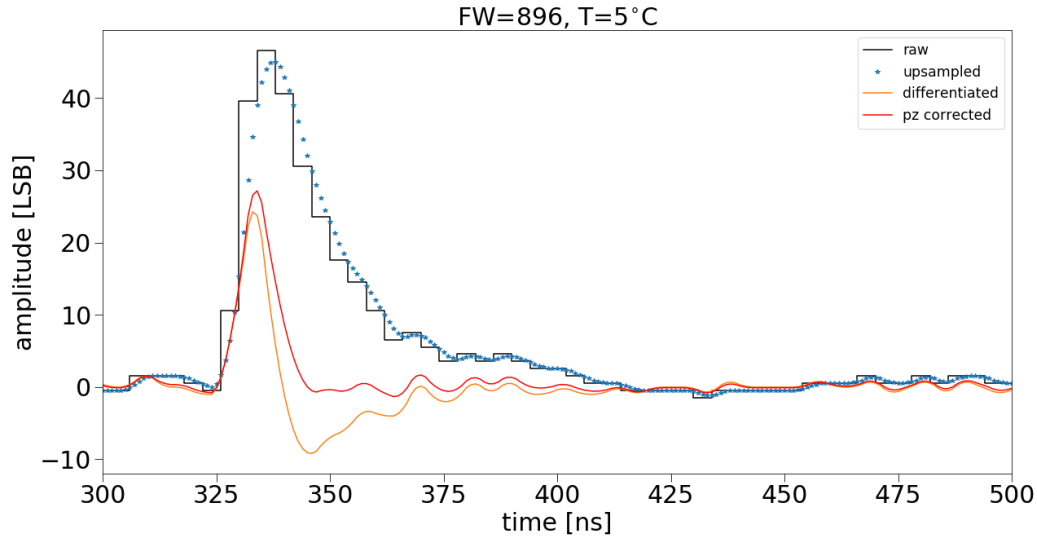

FIGURE 4.5: Baseline-corrected signal from one of the camera's pixels, at a fixed position of the filter wheel (896) and temperature (5 °C). *Black solid line*: digitized waveform, with 4 ns resolution. *Blue stars*: up-sampled and smoothed signal. *Orange solid line*: differentiated signal. *Red solid line*: pole-zero corrected signal.

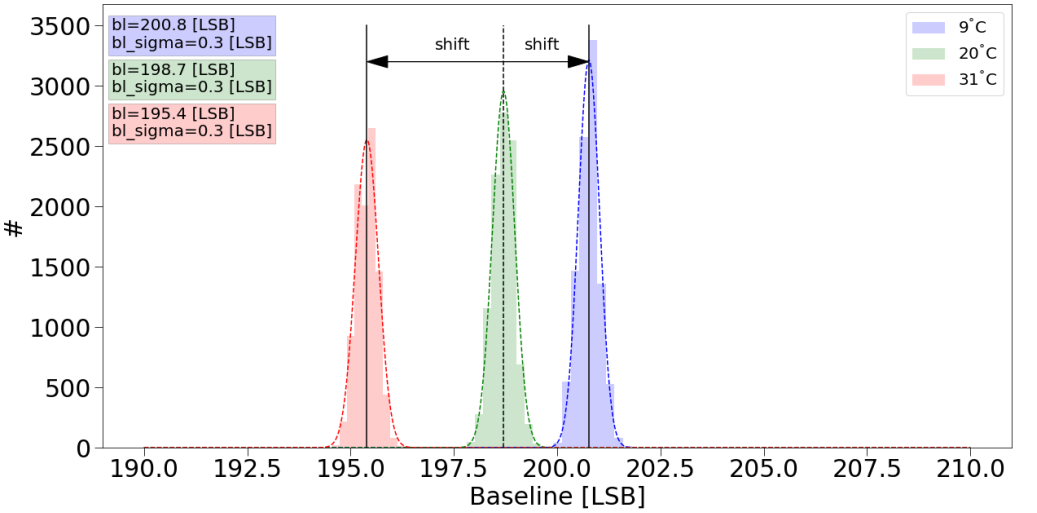

FIGURE 4.6: Baseline histogram for one of the camera's pixels, at a fixed position of the filter wheel (1472). *Green*: baseline histogram at 20 °C, *blue*: baseline histogram at 9 °C, *red*: baseline histogram at 31 °C. Solid dashed lines: Gaussian fits to the distributions. The baseline shift is calculated with respect to the mean value at 20 °C

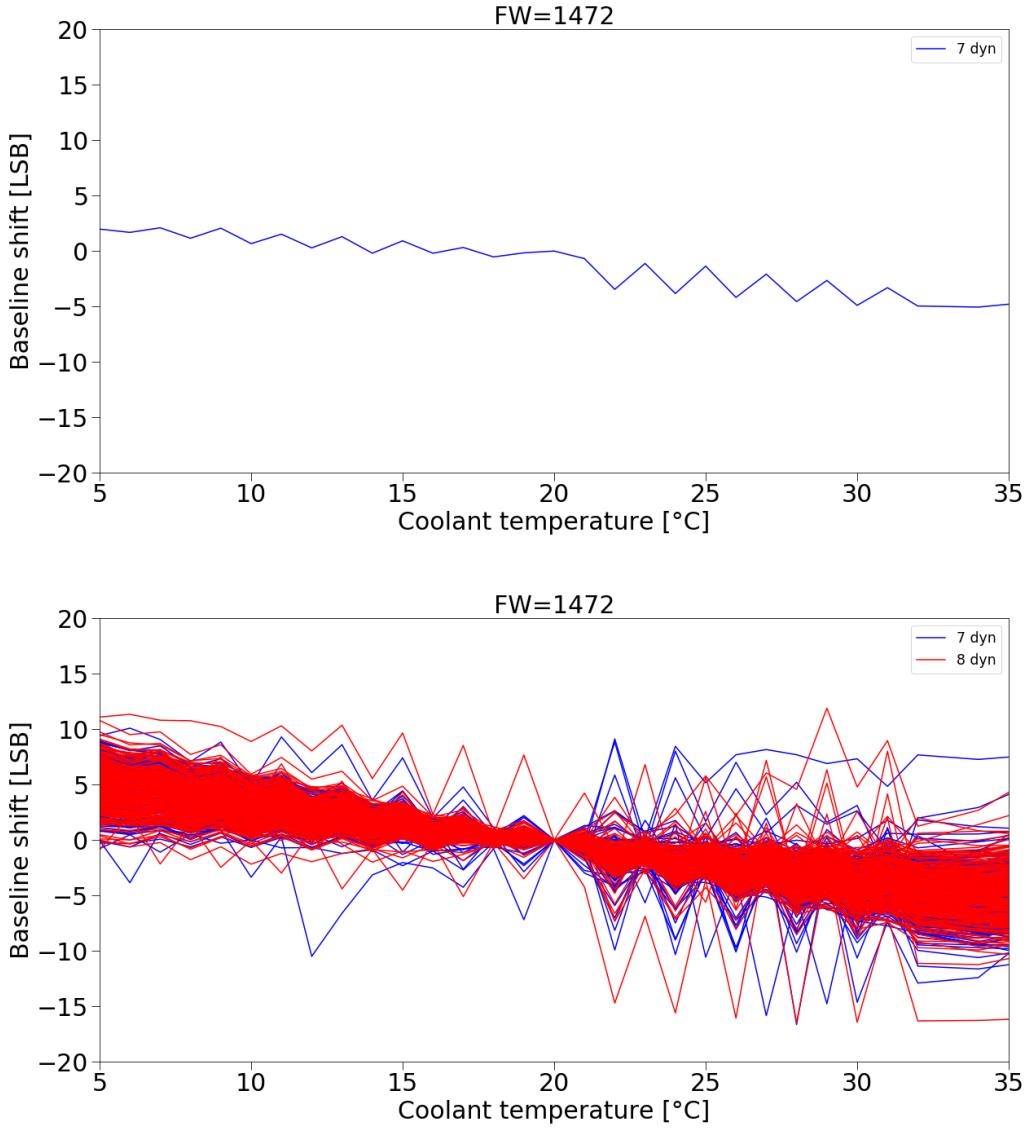

FIGURE 4.7: *Top:* drift with temperature of the baseline shift with respect to 20 °C, for one of the camera's channels, at a fixed position of the filter wheel (1472). *Bottom:* drift with temperature of the baseline shift for all the active channels.

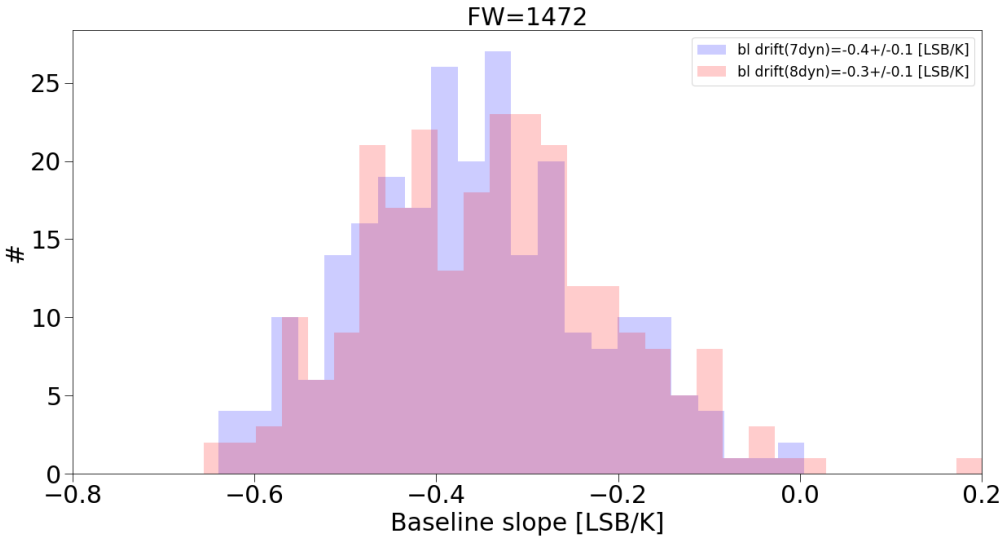

FIGURE 4.8: Baseline drift distribution, at a fixed position of the filter wheel (1472). *Blue*: 7-dynodes PMTs, *red*: 8-dynodes PMTs.

Consistent results have been obtained across all the tested filter wheel positions and are reported for completeness in table 4.1; such predictable behavior enables a reliable calibration of the baseline at different temperatures of operation, which can be used during event reconstruction using a lookup table.

TABLE 4.1: Average baseline drift with temperature of the camera's pixels, at different positions of the filter wheel.

	FW: 640	FW: 896	FW: 1472	FW: 1856	FW: 2240
7-dyn drift [LSB/K]	-0.4±0.1	-0.4±0.1	-0.4±0.1	-0.4±0.1	-0.4±0.1
8-dyn drift [LSB/K]	-0.3±0.1	-0.3±0.1	-0.3±0.1	-0.3±0.1	-0.3±0.1

4.3.2 Gain stability

The output signal of each camera's pixel is proportional to the number of photo-generated carriers which are multiplied through the dynode stages of the PMT. For a generic PMT, the gain (expressed in number of carriers) can be described by the following equation (Knoll, 2000):

$$G = fR^N. \tag{4.2}$$

R is the multiplication factor for each dynode, i.e., the ratio between the number of emitted secondary electrons and the primary incident electron; N is the number of stages of the PMT and f is the fraction of all photoelectrons collected by the multiplier structure.

As a consequence, the distribution of the peak amplitudes in a time window around the laser trigger will reflect the source photon distribution. Depending on the gain of the PMT, quantized pulses with different amplitudes will be produced, as illustrated in Figure 4.9.

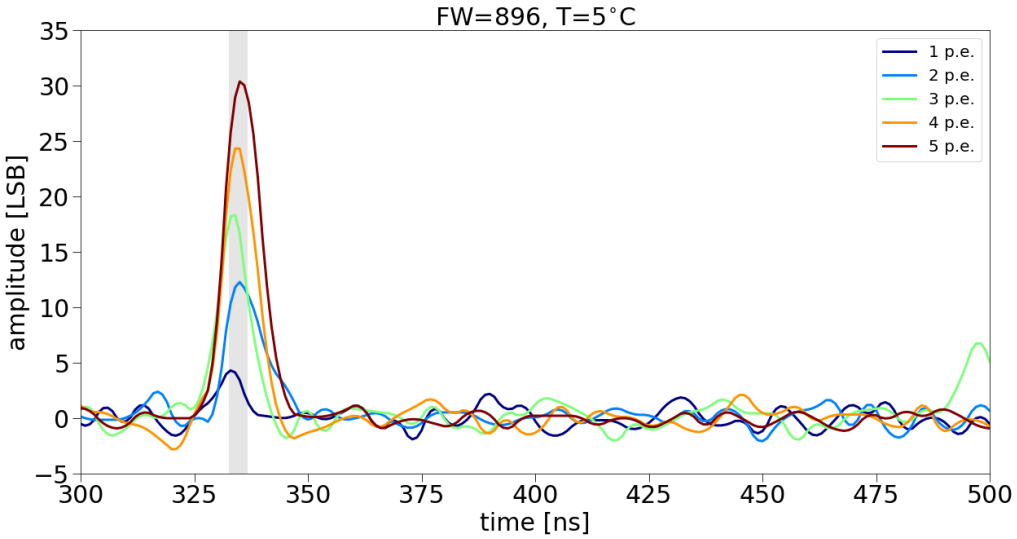

FIGURE 4.9: Post-processed waveforms from one of the camera's pixels, at a fixed position of the filter wheel (896) and temperature (5 °C). The gray box highlights the time window in which the maximum amplitude is searched; the selected waveforms correspond to signals generated from different number of photons impinging on the pixel.

At low illumination rates (i.e., for positions of the filter wheel 640 and 896) it is possible to give an estimate of each pixel's gain from its single photoelectron (SPE) distribution.

The SPE response of a PMT can be parametrized following the arguments proposed in Bellamy et al. (1994), which are here briefly summarized. Given the mean number of photons impinging on the photocatode (m) and the photocatode quantum efficiency (q), $\mu = mq$ represents the mean number of collected photoelectrons.

Therefore, $p\,(n, \mu)$ is the probability to observe n photoelectrons, which follows a Poisson distribution:

$$p\,(n, \mu) = \mu^n \frac{e^{-\mu}}{n!}. \tag{4.3}$$

Assuming large R and f close to 1, the charge distribution at the end of a PMT's multiplication system can be described by a Gaussian distribution:

$$g_n = \frac{1}{\sigma_1 \sqrt{2\pi n}} e^{-\frac{(x - n q_1)^2}{2 n \sigma_1^2}}; \tag{4.4}$$

$q1$ and σ_1 are mean and Gaussian sigma of the first photoelectron peak, respectively.

The response of an ideal PMT (without taking into account possible noise sources) will therefore be the convolution of the distributions 4.3 and 4.4:

$$\begin{aligned} S_{ideal} &= p(0,\mu) \times \delta(x) \\ &+ p(1,\mu) \times g_1 \\ &+ ... \\ &+ p(n,\mu) \times g_n \end{aligned} \tag{4.5}$$

where $\delta(x)$ is the delta function.

In a real PMT, the *pedestal* peak (i.e., the peak corresponding to $p(0,\mu)$) has a finite width and can be approximated with a gaussian distribution as well

$$g_0 = \frac{1}{\sigma_0\sqrt{2\pi}} e^{-\frac{(x-q_0)^2}{2\sigma_0^2}}. \tag{4.6}$$

Moreover, some background signals caused e.g., by photoemission from the focusing electrodes and dynodes, can further modify the output spectrum; if the amplitude of such signals decreases exponentially, the pedestal peak distribution can be approximated by the following equation:

$$S_{pedestal} = p(0,\mu) \times (w \times emg(x, q_0, \sigma_0, \alpha) + (1-w) \times g_0) \tag{4.7}$$

where

$$emg(x, q_0, \sigma_0, \alpha) = \frac{1}{2\alpha} e^{\frac{1}{2\alpha}\left(2q + \frac{\sigma_0^2}{\alpha} - 2x\right)} erf\left(\frac{\mu + \frac{\sigma_0^2}{\alpha} - x}{\sqrt{2}\sigma}\right) \tag{4.8}$$

and w is the weight of the pedestal component affected by the exponential noise.

The overall PMT response function under realistic operational circumstances will therefore be

$$\begin{aligned} S &= p(0,\mu) \times (w \times emg(x, q_0, \sigma_0, \alpha) + (1-w) \times g_0) \\ &+ p(1,\mu) \times g_1 \\ &+ ... \\ &+ p(n,\mu) \times g_n. \end{aligned} \tag{4.9}$$

An example of a PMT output spectrum is shown in figure 4.10, for a fixed position of the filter wheel and temperature. Before operation, the camera has been gain flat-fielded, i.e., the bias of each PMT has been tuned in order to have a uniform gain across the different pixels. As a consequence, the shown amplitude distributions exhibit a very good overlap.

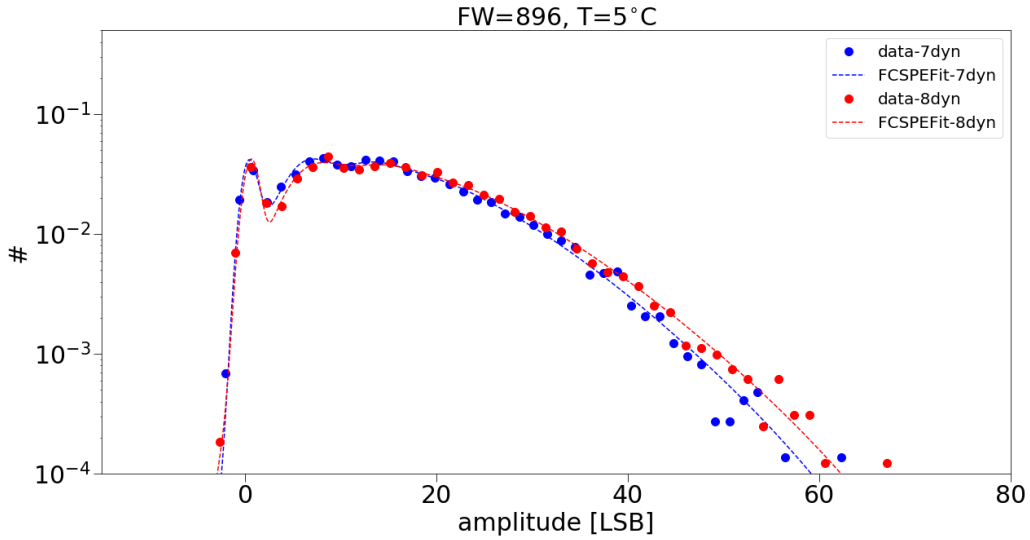

FIGURE 4.10: SPE distribution for one 7-dynode (*blue*) and one 8-dynode (*red*) PMT of the camera, at a fixed position of the filter wheel (896) and temperature (5 °C). Dashed lines: fit to the data, according to 4.9 Before operation, the camera has been gain flat-fielded, as it can be deduced by the good overlap of the PMTs' distributions.

The PMT gain (expressed in LSB), can be calculated as the difference between the mean of the first photoelectron and the the mean of the pedestal peak

$$G = q_1 - q_0. \tag{4.10}$$

In order to estimate the gain stability, a procedure similar to the one described in 4.3.1 has been followed. For each channel, at a fixed temperature T, the ratio between the gain at T and the one at 20 °C has been calculated. Figure 4.11 illustrates the temperature drift of the gain ratio for all the camera's pixels under study.

The gain drift of each channel (expressed in %/K) is estimated as the slope of a linear fit to the data shown in Figure 4.11 (filter wheel position 896).

Figure 4.12 shows the resulting gain-drift distributions for the 7- and the 8-dynode PMTs respectively, at a fixed position of the filter wheel. As it can be observed, the 8-dynode PMTs suffer from a slightly higher temperature dependence, probably because of the higher number of dynode stages.

Consistent results have been obtained for the lowest tested illumination rate (i.e., for position 640 of the filter wheel). It is important to notice that, independently from the PMT gain (at least in a linear amplification regime), the electronics of the FlashCam suffers from a negligible influence of external parameters, such as the temperature. The relative gain variations over a wide range of conditions are well below the percent level (about -0.2%/K for the 7-dynodes and about -0.6%/K for the 8-dynodes): such a stable and reproducible behavior implies relatively minor adjustments to the HV of the PMTs (in case needed).

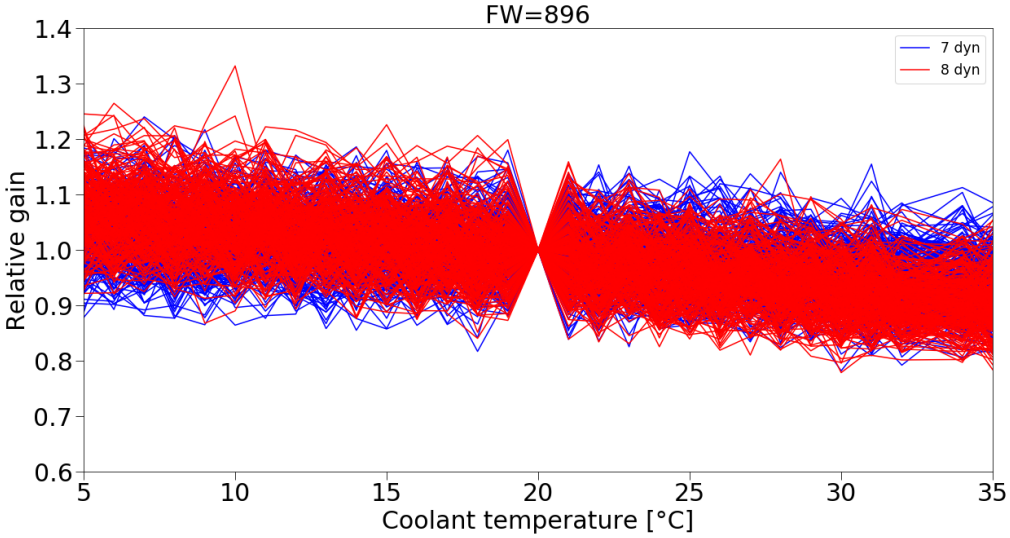

FIGURE 4.11: Drift with temperature of the pixels' gain; *blue*: 7-dynode PMTs, *red*: 8-dynode PMTs.

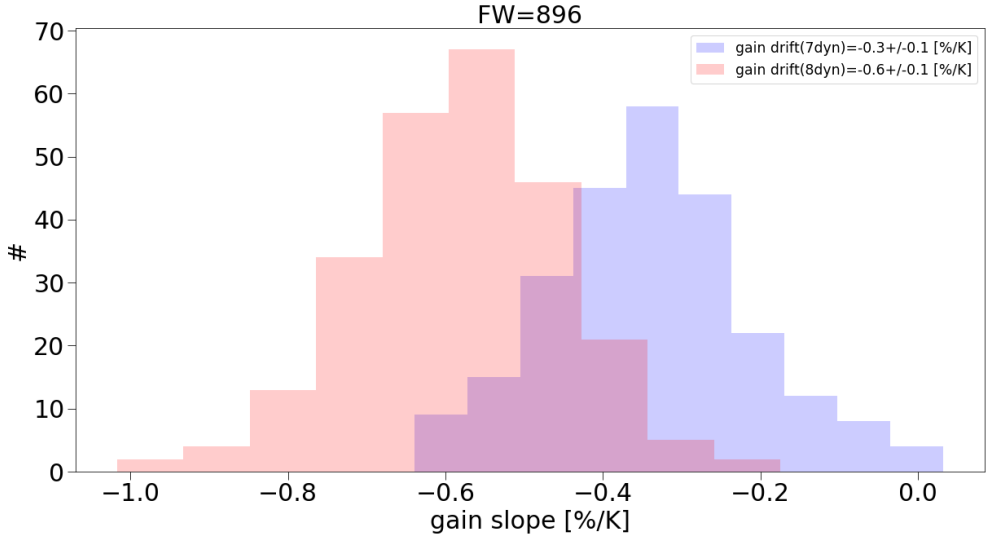

FIGURE 4.12: Gain drift distribution, at a fixed position of the filter wheel (896). *Blue*: 7-dynodes PMTs, *red*: 8-dynodes PMTs.

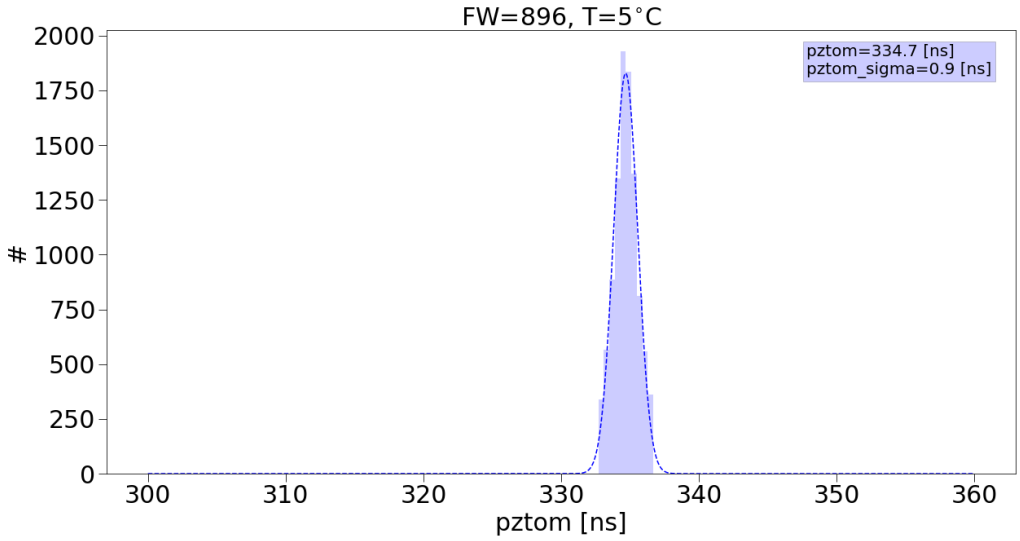

FIGURE 4.13: Time of maximum distribution for one of the camera's pixels, at a fixed temperature (5 °C) and position of the filter wheel (896).

4.3.3 Time of maximum

Similarly to what previously done for baseline and gain, the stability with temperature of the measured arrival times of light pulses can be estimated. The results presented in this section concern the acquisition cycles at FW position 896.

For each channel, at a fixed temperature, the position of the peak signal in a pre-defined time window around the laser trigger is searched (e.g., in the grey window in Figure 4.9). An example of the time-of-maximum distribution for one of the camera's channels, at a fixed temperature, is illustrated in Figure 4.13; the mean and sigma after a Gaussian fit to the data are then extracted. Afterwards, the shift with respect to the mean at 20 °C is estimated.

Figure 4.13 shows the temperature drift of the time of maximum for each channel, with respect to the value at 20 °C.

The time-of-maximum drift, expressed in ps/K, is estimated as the slope of a linear fit to the data shown in Figure 4.13. As illustrated in Figure 4.14, the 8-dynode PMTs exhibit a slightly higher temperature drift due to the higher number of dynodes; in both cases, anyway, the average drift is relatively small (up to less than 10 ps) and can be corrected by a proper adjustment of the PMTs' HV.

4.3.4 Conclusions

The prototype FlashCam long-term performances have been probed in the linear amplification regime, showing a reproducible behavior over a wide range of temperatures; the baseline, gain and timing drifts can therefore be corrected using lookup tables (or, in the case of timing and gain, by properly adjusting the PMTs' bias). Further tests and measurements at higher signal amplitudes (> 250 p.e.) are required to better characterize the stability of the camera's performances in the non-linear regime.

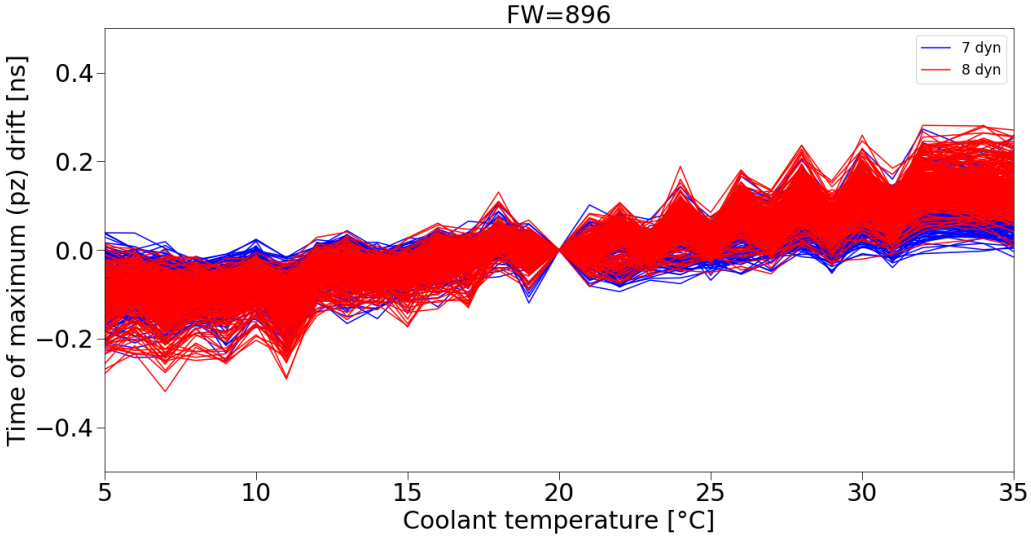

FIGURE 4.14: Drift with temperature of the pixels' time of maximum; *blue*: 7-dynode PMTs, *red*: 8-dynode PMTs.

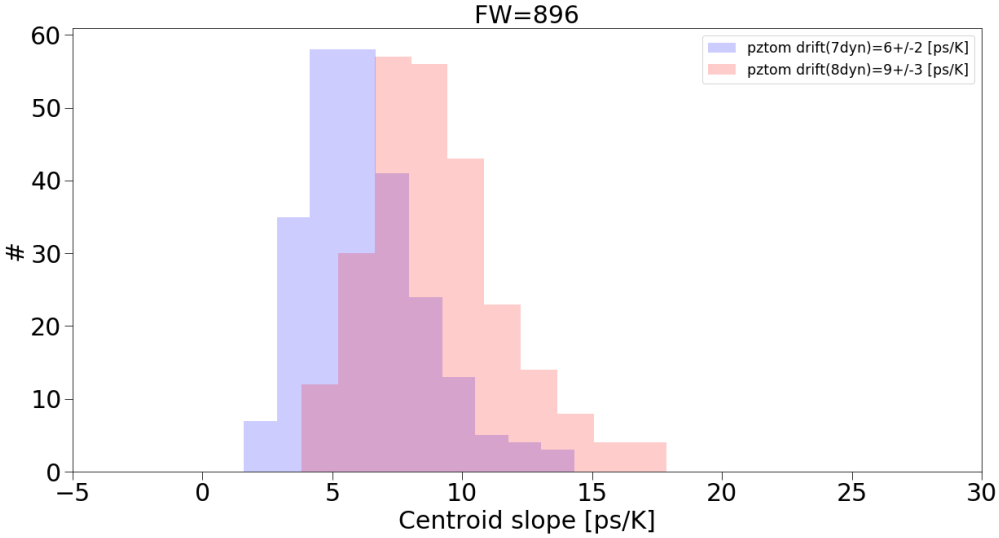

FIGURE 4.15: Time of maximum drift distribution, at a fixed position of the filter wheel (896). *Blue*: 7-dynodes PMTs, *red*: 8-dynodes PMTs.

Conclusions

Over the last decades, γ-ray astronomy has proven to be an important tool to investigate the non-thermal Universe. In this field, IACTs play a crucial role in understanding the most energetic astrophysical phenomena in the farthest accessible γ-ray band, around and above $1\,\mathrm{TeV}$.

Within our Galaxy and outside it, several objects are known to emit HE to VHE γ-rays; among the Galactic emitters, pulsar wind nebulae and supernova remnants represent the most populated source classes. SNRs are the remnants of violent star explosions, whose blast wave can accelerate cosmic rays in the surrounding medium up to very high energies (possibly up to $\sim 10^{15}\mathrm{eV}$ in our Galaxy). One of the reasons that make SNRs of prime interest in the astrophysics community is indeed the fact that they could explain the origin of cosmic rays. The motivations are two-fold: first of all, it can be shown that the power required to supply Galactic CRs could be satisfied by a core-collapse SN explosion every 30 years, ejecting about 10 solar masses with a velocity of approximately $5 \times 10^8 \mathrm{cm\,s^{-1}}$, with an efficiency of few percent. Second, it can be demonstrated that particle acceleration at a strong shock wavefront (as the one observed in SN explosions) naturally leads to a power-law spectrum with index close to the one observed for local CRs.

Most Galactic SNRs have been discovered through radio continuum surveys, i.e., through the synchrotron emission of GeV electrons accelerated at their shock-fronts. The classification criterion is usually based on their morphology in the waveband of discovery: highly significant shell-like structures are classified as SNR candidates, and confirmed as SNRs in case an independent detection in another waveband is available. The idea of the study presented in Chapter 2 is to systematically search for new SNR candidates in the TeV band. The sky maps on which the search has been conducted are the ones produced for the latest survey of the Galactic Plane with one of the leading IACTs currently operating: the High Energy Stereoscopic System (H.E.S.S.). Between 2004 and 2013 the H.E.S.S. experiment has collected roughly 2700 hours of high quality observations, leading to an updated catalog of the Galactic Plane which includes roughly 80 sources of VHE γ-rays. Within the collaboration, a method to systematically search for shell-like structures on a grid of sky coordinates was developed. The search led to the identification of three new significant TeV shells (HESS J1534$-$571, HESS J1614$-$518, HESS J1912$+$101); as a follow-up study, a source-by-source analysis was carried out. The author's main focus was the morphological analysis of the single sources, with particular consideration of the statistical implications of comparing non-nested models for the assessment of the *shellness* of a given object. One of the three sources (HESS J1534$-$571) could be classified as new SNR, given the presence of a morphologically matching radio counterpart; for the other two (HESS J1614$-$518 and

HESS J1912+101), no compelling multiwavelength counterpart could be found; for this reason they are at present considered SNR candidates. For all the three objects, an estimate of the fraction of the SNR explosion energy going into accelerated CRs has been given by the author, for different distances and target gas densities: provided that the distances are not too high, a hadronic emission scenario is plausible for all the new TeV shells.

The presented study has demonstrated the potential of current-generation IACTs to identify new SNRs, based on their shell-like appearance in the TeV band: to our knowledge, it was the first time that a morphological search criterion could be successfully applied to identify new TeV-selected SNRs. The results of the study are also published in H.E.S.S. Collaboration et al. (2018a).

Chapter 3 focuses on the shell-type SNR HESS J1731−347, which belongs to the TeV-resolved SNRs known to date. It shows similar parameters to the other prominent TeV shells in terms of physical size and luminosity in the $1-10\,\mathrm{TeV}$ band; as RX J1713.7−3946 and Vela Jr. it is found to be spatially coincident with a faint radio SNR and displays non-thermal X-ray emission. The distance to the source is currently matter of debate in the literature, where three possible solutions are suggested: near ($\sim 3.2\,\mathrm{kpc}$), intermediate ($\sim 4.5\,\mathrm{kpc}$) and far ($5-6\,\mathrm{kpc}$). One reason that makes HESS J1731−347 particularly interesting is the nearby γ-ray source HESS J1729−345. In a recent work (Cui, Pühlhofer, and Santangelo, 2016), it has been demonstrated that, for the nearest distance solution, it is plausible that the emission seen from this source is caused by CRs escaping from the SNR and illuminating nearby molecular clouds (MCs).

The study carried out in Chapter 3 presents the results of an updated H.E.S.S. analysis performed by the author, with the additional data available since the work published in 2011 (H.E.S.S. Collaboration, 2011). The analysis has revealed the morphology of the emission in-between HESS J1731−347 and HESS J1729−345 in greater detail, highlighting an interesting visual correspondence between the TeV γ-rays and the radio emission from a dense molecular gas tracer (CS) seen with the Mopra telescope at $3.2\,\mathrm{kpc}$. Starting from such visual indication, a method to try and quantify numerically the correlation between TeV and gas at $3.2\,\mathrm{kpc}$ (or at other distances) has been devised and applied for the first time. Two main scenarios have emerged:

- the VHE emission from outside the remnant could be caused by the superimposition of the TeV γ-rays produced in the interaction between background CRs and MCs at different distances or
- the emission from part of the remnant and the bridge region linking HESS J1731−347 to HESS J1729−345 could be caused by escaping CRs illuminating nearby MCs at $3.2\,\mathrm{kpc}$.

The first scenario is the most significant according to the employed correlation method (linear correlation coefficient $r = 0.54$ with p-value $p = 1.5 \times 10^{-5}$), though being disfavored in terms of expected γ-ray flux (about one order of magnitude lower than the observed one, in a purely-hadronic emission scenario). None of the two hypothesis could be firmly

confirmed by the presented analysis; nonetheless, the outlined correlation method should be able to detect a true correlation, in case present, possibly with deeper observations carried out by next-generation instruments like CTA.

Chapter 2 and 3 have highlighted both the capabilities and the limitations of the currently operational IACTs. The next-generation instrument of this kind, CTA, is expected to improve significantly the technical performance in terms of accessible energies and sensitivity. Within CTA, the University of Tübingen is part of the FlashCam team, which has developed a camera concept based on a fully-digital readout and triggering processing. Chapter 4 gives an overview of the results obtained from the long-term tests performed during summer 2016, on a partially-equipped (720 PMTs over 1764) prototype camera. At the time of data-taking, two PMT variants (7- and 8-dynodes) were still under testing. The test campaign has spanned a large range of temperatures ($5 - 35\,^{\circ}\mathrm{C}$) and different illumination conditions, probing the linear (up to $\sim$ 250 p.e.) and the non-linear (> 250 p.e.) amplification regimes of the electronics. The results presented in Chapter 4 mainly focus on the linear regime, and more specifically investigate the baseline, gain and timing performance of all the channels for the entire temperature range. Despite their preliminary nature, the obtained results show the robustness of FlashCam's signal chain against temperature changes, which ideally translates into a more reliable operation and less down-time. The observed drifts of the baseline (~ -0.4 LSB/K), gain ($\sim -0.6\%$/K for the 8-dynode and $\sim -0.3\%$/K for the 7-dynode variants) and timing ($\sim 9\,\mathrm{ps}$/K and $\sim 6\,\mathrm{ps}$/K for the 8- and 7-dynode PMTs respectively) are reproducible and can be easily accounted for by using lookup tables during event reconstruction (e.g., for the baseline) and by proper adjustment of the PMT's bias (for gain and timing). Further tests at higher illuminations (> 250 p.e.) are ongoing to better characterize the camera's performance in the non-linear regime.

Appendix A

Effective Area of a Cherenkov Telescope

In the following, an estimate of the effective area needed by a Cherenkov telescope for the detection of a prototype source of VHE $\gamma-$rays will be given.

As a consequence of the acceleration mechanisms that take place at the source location, the resulting $\gamma-$ray energy flux can be described, in most of the cases, with a power-law model in the form

$$\frac{\mathrm{d}N_\gamma}{\mathrm{d}E} = N_0 \left(\frac{E_\gamma}{E_0}\right)^{-\Gamma}. \tag{A.1}$$

Equation (A.1) represents the so-called *differential photon flux* and is often measured in units of $\mathrm{TeV}^{-1}\,\mathrm{cm}^{-2}\,\mathrm{s}^{-1}$. N_0 is a normalization factor at energy E_0; Γ is commonly referred to as *differential spectral index* and, for most of the VHE γ-ray sources, it has values ranging between 2 and 3.

Having this in mind, one can calculate what is the effective area a $\gamma-$ray telescope needs to have in order to detect 50 photons in 100 hours from a source with 10% of the flux of RX J1713.7-3946 (a very famous Galactic SNR) above $1\,\mathrm{TeV}$. One can assume that the source photon spectrum continues with a power law E^{-2} up to $100\,\mathrm{TeV}$; for the sake of simplicity one can additionally assume that all the photons that are to be detected have an energy of $100\,\mathrm{TeV}$ and that the resolution at this energy is 10% (in other words one can actually count photons between $90\,\mathrm{TeV}$ and $110\,\mathrm{TeV}$).

Finally, one can assume the following parameters for RX J1713.7-3946: $N_{0,1713} = 2.02 \times 10^{-11}\mathrm{TeV}^{-1}\mathrm{cm}^{-2}\mathrm{s}^{-1}$, $E_{0,1713} = 1\,\mathrm{TeV}$ and $\Gamma_{1713} = 2.32$[1]

[1] RX J1713.7–3946 spectrum is actually better described by an *exponential cut-off power-law* (ECPL) model https://arxiv.org/pdf/1609.08671v2.pdf ($\mathrm{d}N_\gamma/\mathrm{d}E = N_0\,(E/E_0)^{-\Gamma}\,e^{-E/E_{cut}}$ with $\Gamma_{1713} = 2.06$, $E_{cut,1713} = 12.9\,\mathrm{TeV}$, $E_{0,1713} = 1\,\mathrm{TeV}$ and $N_{0,1713} = 2.3 \times 10^{-11}\mathrm{TeV}^{-1}\mathrm{cm}^{-2}\mathrm{s}^{-1}$). However the flux above 1 TeV for the ECPL model is about 10% higher than the one for the PL: for this simple calculation, a power-law model can be safely adopted.

First of all, one needs to calculate the normalization of the PL describing the source to be detected

$$\begin{gathered}
\int_{E_{min}}^{E_{max}} \frac{\mathrm{d}N_\gamma}{\mathrm{d}E}\mathrm{d}E = 0.1 \int_{E_{min}}^{E_{max}} \frac{\mathrm{d}N_{1713}}{\mathrm{d}E}\mathrm{d}E \implies \\
\int_{E_{min}}^{E_{max}} N_0 \left(\frac{E_\gamma}{E_0}\right)^{-\Gamma} \mathrm{d}E = 0.1 \int_{E_{min}}^{E_{max}} N_{0,1713} \left(\frac{E_\gamma}{E_{0,1713}}\right)^{-\Gamma_{1713}} \mathrm{d}E \implies \\
\frac{N_0}{E_0^{-\Gamma}} \frac{E_{max}^{-\Gamma+1} - E_{min}^{-\Gamma+1}}{-\Gamma+1} = 0.1 \frac{N_{0,1713}}{E_{0,1713}^{-\Gamma_{1713}}} \frac{E_{max}^{-\Gamma_{1713}+1} - E_{min}^{-\Gamma_{1713}+1}}{-\Gamma_{1713}+1} \implies \\
(E_0 = E_{0,1713} = 1\,\mathrm{TeV}, E_{min} = 1\,\mathrm{TeV}, E_{max} = 100\,\mathrm{TeV} \approx +\infty) \\
N_0 = 0.1\, N_{0,1713} \frac{\Gamma - 1}{\Gamma_{1713} - 1} \implies \\
N_0 = 1.53 \times 10^{-12}\,\mathrm{TeV}^{-1}\mathrm{cm}^{-2}\mathrm{s}^{-1}
\end{gathered} \tag{A.2}$$

The number of photons $\#_\gamma$ with energy in the range $90 - 110\,\mathrm{TeV}$, detected in the time interval t, can then be calculated as

$$\#_\gamma = \int_{90\,\mathrm{TeV}}^{110\,\mathrm{TeV}} \frac{\mathrm{d}N_\gamma}{\mathrm{d}E}\, A_{\mathrm{eff}}\, t\, \mathrm{d}E \tag{A.3}$$

According to (A.3), if one assumes A_{eff} to be constant over the selected energy range, one obtains $A_{\mathrm{eff}} \approx 4.5 \times 10^6\,\mathrm{m}^2$.

In experimental terms, this number directly translates into the need of finding a way to detect VHE γ-rays from astrophysical sources that does not imply flying a km^2 effective area detector to space.

Appendix B

Imaging atmospheric Cherenkov telescopes technique

In this appendix, some basic Physics results that are exploited in IACTs are presented.

B.1 Heitler's model of an e.m. shower

The key points of the development of an e.m. shower, schematically represented in Figure 1.6 can be summarized as follows:

- a VHE $\gamma-$photon with energy E_i enters the atmosphere and produces an electron/positron pair (having energy $E_i/2$ each)
- let us define $d = \lambda_r \log 2$ the distance after which an electron (positron) looses half of its energy due Bremsstrahlung; λ_r is the radiation length in the medium[1]
- at each step, the primary energy of the photon is degraded by a factor of 2: either an electron (positron) halves its energy by radiating a Bremsstrahlung photon, either a photon undergoes pair production. After n steps, the size of the shower will be $x = n\lambda_r \log 2$, whereas the number of particles will be $N = 2^n = 2^{\frac{x}{\lambda_r}\frac{1}{\log 2}} = 2^{\frac{x}{\lambda_r}\frac{\log_2 e}{\log_2 2}} = e^{\frac{x}{\lambda_r}}$
- at the critical energy E_c ($\sim$ $85\,\mathrm{MeV}$ in air) ionization energy losses equal radiative ones; below E_c Bremsstrahlung becomes inefficient and the multiplication ceases
- when all particles reach E_c, the shower has reached N_{max}. This means that $E_i = E_c\, N_{max}$, i.e., the number of particles that develop in an e.m shower is proportional to the initial photon energy
- moreover, one can calculate the depth X_{max} at which the maximum size of the cascade is achieved. If we name n_c the number of steps which are needed for each of the particles to have energy E_c, then $n_c = \log[E_i/E_c]/\log 2$. Therefore, $X_{max} = n_c \lambda_r \log 2 = \lambda_r \log[E_i/E_c]$. That is: the penetration depth at which the maximum of the cascade is reached goes with the logarithm of the initial photon energy E_i

[1] once the medium is known, hence its density, λ_r is equivalent to X_0 defined in 1.2.1

The model presented above is known as *Heitler's* model of an e.m. shower and is reviewed in a nice paper by J. Matthews (Matthews, 2005), along with more realistic simulations. One limitation of this simplified approach is that it largely underestimates the ratio between the produced photons and charged particles, mainly because the radiation of multiple Bremsstrahlung photons is neglected. According to Heitler's model, the amount of electrons approaches the value $N_e \approx \frac{2}{3} N_{max}$ after a few iterations; simulations show instead that the number of photons is more than a factor of six larger than the number of charged particles.

B.2 The Cherenkov effect

If a charged particle travels in a dielectric medium (e.g.,: Earth's atmosphere), it causes the polarization of its molecules; after the particle's passage, electromagnetic waves are emitted in the molecules' relaxation process. At low particle energies, these waves interfere destructively (Grieder, 2010).

However, if the particle travels faster than light's phase velocity in the medium ($v_c = c/n$, with n the medium's refractive index) the radiation adds up in a coherent wave, with angle θ_c. θ_c and n are related by the following formula

$$\cos\theta_c = \frac{1}{\beta\, n} \tag{B.1}$$

with $\beta = v_{particle}/c$.

This phenomenon is named *Cherenkov effect*, after the Soviet scientist Pavel Aleksejevich Cherenkov, who was awarded the Nobel prize in 1958 for first detecting this effect experimentally.

As explained above, the emission of Cherenkov light takes place when the particle travels faster than light in a medium; in other words, it is a threshold process occurring above a given energy. The minimum energy that a particle with rest mass m_0 needs to have for Cherenkov light to be emitted, can be calculated in the limit case in which the particle's velocity is exactly c/n, using the following formula

$$E_{th} \approx \frac{m_0 c^2}{\sqrt{n^2 - 1}} \tag{B.2}$$

If one takes $n \approx 1.003$ for air (this is true at sea level), the threshold energy for an electron (equivalently a positron) can be easily calculated: $E_{th,e} \approx 21\,\mathrm{MeV}$.

As it follows from equation (B.1), the emission angle at the threshold energy $\theta_{c,th} = 0$. The maximum angle can be derived by assuming that the particle has $\beta \approx 1$; for air at sea level this implies $\theta_{c,max} \approx 1.4°$.

If a detector were placed on the ground, how would the distribution of the Cherenkov light look like?

As exemplifying case, one can consider a relativistic particle with $\beta \approx 1$, starting from an altitude of $20\,\mathrm{km}$ above the sea level (a.s.l.) and reaching the ground practically undeflected (i.e., the effect of scattering is neglected).

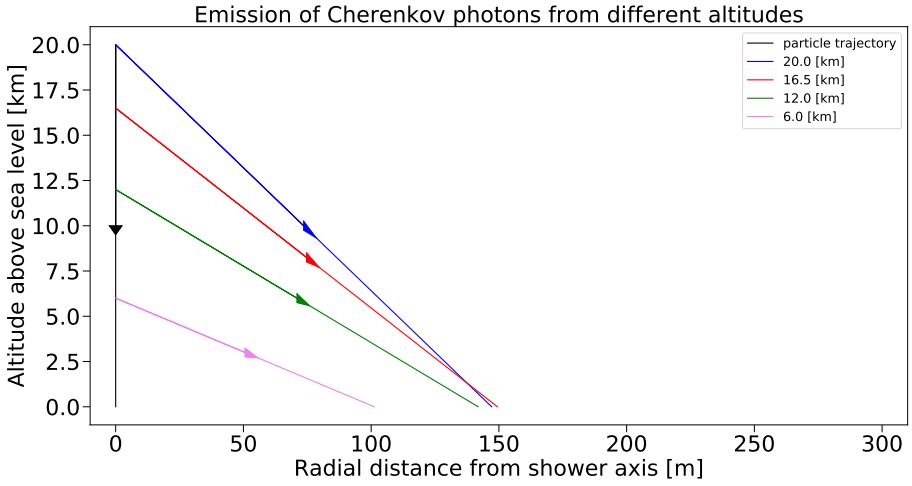

FIGURE B.1: Emission of Cherenkov photons from different altitudes, from a single relativistic particle with $\beta \approx 1$ travelling practically undeflected from $20\,\mathrm{km}$ to the ground. As the particle descends, the Cherenkov angle widens as a consequence of the dependence of the refractive index on altitude.

Along the particle's trajectory, Cherenkov photons are emitted at an angle θ_c. However, as the density of air varies with altitude, θ_c is not constant over the entire path to the ground; more specifically, since the refractive index n decreases with altitude, the smallest θ_c is at the very beginning of the particle's trajectory (as it can be derived from equation (B.1)).

A schematic representation of the widening of the Cherenkov angle with decreasing altitude is shown in Figure B.1

Numerical calculations can be performed making the following assumptions:

$$n(X) = 1.0 + 0.00029 \left(\frac{X}{X_0} \right) \tag{B.3}$$

X is the *atmospheric depth*[2] (expressed in $\mathrm{g\,cm^{-2}}$) and X_0 its value at sea level $X_0 = 1033\,\mathrm{g\,cm^{-2}}$; moreover

$$X = \frac{P_0}{g_0}\, e^{-\frac{M g_0}{R T_0} z} \tag{B.4}$$

where

- $M = 0.028\,964\,4\,\mathrm{kg\,mol^{-1}}$ is the molar mass of Earth's air
- $g_0 = 9.980\,665\,\mathrm{m\,s^{-2}}$ is the standard gravitational acceleration
- $P_0 = 101\,325\,\mathrm{Pa}$
- $R = 8.314\,459\,8\,\mathrm{J\,mol^{-1}\,K^{-1}}$ is the universal gas constant
- $T_0 = 288.15\,\mathrm{K}$

[2]This parametrization is adapted from the one presented in Grieder (2010): $n(X) = 1.0 + 0.00029 \left(\frac{X}{X_0} \right) \left(\frac{T_0}{T} \right)$, with $X_0 = 1030\,\mathrm{g\,cm^{-2}}$, $T_0 = 273.2\,\mathrm{K}$ and T = 204 + 0.91X. The dependence on T is neglected.

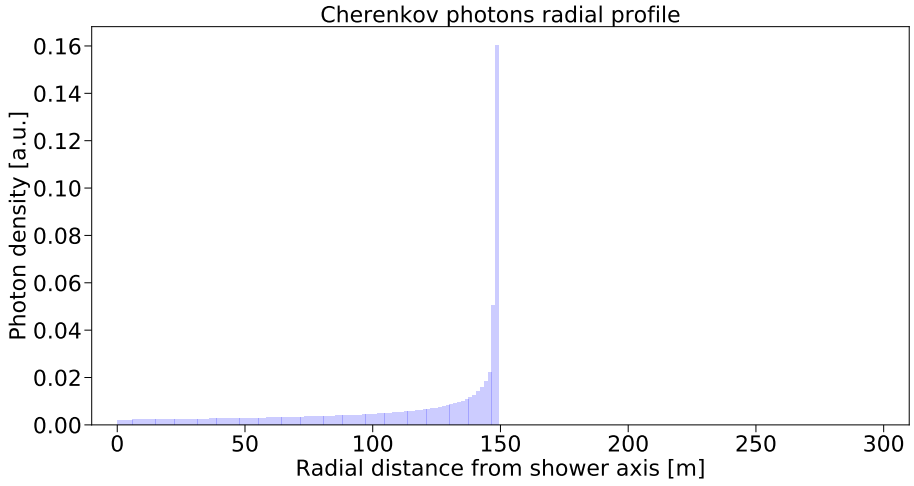

FIGURE B.2: Cherenkov photon density distribution as a function of the radial distance from the shower axis. The graph is built for a single relativistic particle with $\beta \approx 1$, in the hypothesis that scattering does not affect the trajectory of the particle itself. In this ideal case, it is apparent the *Cherenkov ring* effect: most of the light is concentrated on the edge of the so-called *Cherenkov pool*.

- $\frac{Mg_0}{RT_0} = \frac{1}{h_0}$, $h_0 \approx 8.4\,\mathrm{km}$ in the Troposphere (i.e., up to about $20\,\mathrm{km}$ a.s.l.)

Temperature T and gravitational acceleration g are assumed to be constant over the range of distances of interest [3].

Figure B.2 shows the Cherenkov photon density distribution on the ground as a function of the radial distance from the shower axis.

In the ideal case presented so far, the *Cherenkov ring* effect is apparent: as the Cherenkov angle broadens with decreasing altitude, most of the light is concentrated on the edge of the so-called *Cherenkov pool*.

Taking into account the effect of scattering along the particle's trajectory, leads to a flattening of the photon density distribution up to the edge of the Cherenkov pool, after which it drops.

The spectral distribution of the emitted Cherenkov light can be expressed according to the Frank-Tamm formula

$$\frac{\mathrm{d}^2 N}{\mathrm{d}x \mathrm{d}\lambda} = 2\pi\alpha Z^2 \lambda^{-2} \left(1 - \frac{1}{\beta^2 n\left(\lambda\right)^2}\right) \tag{B.5}$$

which gives the number of emitted photons per unit wavelength and unit distance travelled by the particle. Equation (B.5) diverges for small wavelengths; however, below about $300\,\mathrm{nm}$, the atmosphere is not transparent to the Cherenkov light. As a result, the distribution of Cherenkov radiation peaks in the ultraviolet (UV) band, close to optical wavelengths.

[3] This approximation is quite accurate for what concerns g, where the variation from $20\,\mathrm{km}$ to ground is of the order of less than a percent. On the other hand, T varies about 20%; nonetheless, for the sake of simplicity, it is assumed constant.

Appendix C

HESS J1614−518: more complex models

In this appendix, the attempt to test more complex models for HESS J1614−518 is reported. As explained in Section 2.1.3, though a shell model is preferred over a simple Gaussian and seems to be a good approximation for the description of the source, bright residuals in the North and the South are clearly visible. The idea is therefore to try and account for the northern and southern spots by modelling them as additional Gaussian components. In the fits, the starting coordinates of these two components (hereafter N and S) are respectively coincident with the 2FGL[1] sources J1615.2−5138 (N) and J1614.9−5212 (S).

Three different models have been tested:

- *pure* two-Gaussian scenario, i.e. N and S only;
- one shell (HESS J1614−518) and the northern component N;
- one shell (HESS J1614−518) and both the northern (N) and the southern (S) components

In all cases, HESS J1616−508 has been modelled with a Gaussian morphology.

Hereafter the results of this attempt are reported. Along with the table containing the fit parameters (Table C.1), also a table with the $\mathcal{L}_{\mathrm{AIC},H_0}$ values for the different tested models is given (Table C.2); $\mathcal{L}_{\mathrm{AIC},H_0}$ quoted on the last column always compares the more complex models to the simple shell: for both main and cross-check analysis a *pure* two-Gaussian scenario is not favoured over a single shell model, while adding the northern component clearly improves the quality of the fit (though the fit parameters differ substantially between the analyses - see Table C.2). Moreover, while for the main analysis considering the additional southern component brings no further improvement in the fit quality ($\mathcal{L}_{\mathrm{AIC,H_0}}$ in this case is higher than for the shell + N model), the situation is reversed for the cross-check analysis. Especially apparent in the main analysis is the fact that the northern component displaces towards HESS J1616−508, while the southern component tries to cover for the northern spot. These instabilities might be due to the excessive sensitivity of the fit to fluctuations in the maps which are however on a sub-significant scale. In all the fits described so-far, all the parameters of the models have been left un-thawed; further attempts to freeze the coordinates

[1] https://fermi.gsfc.nasa.gov/ssc/data/access/lat/2yr_catalog/

and extensions of N and S to the *pure* two-Gaussian best fit or to the 2FGL catalogued values have been made, though no improvement in the fit quality has been achieved.

Due to the above mentioned issues and for consistency with the other two SNR candidates discovered in this study, HESS J1614−518 has therefore been treated as a simple shell.

TABLE C.1: Results from the study of the new SNR shell candidate HESS J1614−518, in the case more complex morphological models than a simple shell are considered. ^{a}: Galactic longitude of the shell best-fit centroid. ^{b}: Galactic latitude of the shell best-fit centroid. ^{c}: inner radius of the shell model. ^{d}: outer radius of the shell model. ^{e}: Galactic longitude of the northern Gaussian best-fit centroid. ^{f}: Galactic latitude of the northern Gaussian best-fit centroid. ^{g}: standard deviation of the northern Gaussian. ^{h}: Galactic longitude of the southern Gaussian best-fit centroid. ^{i}: Galactic latitude of the southern Gaussian best-fit centroid. ^{l}: standard deviation of the southern Gaussian.

N+S	main	x-check	**shell+N**	main	x-check	**shell+N+S**	main	x-check
			$l_{0,\mathrm{shell}}{}^a$	$331.45°$	$331.44°$	$l_{0,\mathrm{shell}}{}^a$	$331.44°$	$331.46°$
			$b_{0,\mathrm{shell}}{}^b$	$-0.62°$	$-0.61°$	$b_{0,\mathrm{shell}}{}^b$	$-0.61°$	$-0.60°$
			$R_{\mathrm{in}}{}^c$	$0.20°$	$0.24°$	$R_{\mathrm{in}}{}^c$	$0.23°$	$0.26°$
			$R_{\mathrm{out}}{}^d$	$0.39°$	$0.37°$	$R_{\mathrm{out}}{}^d$	$0.39°$	$0.34°$
$l_{0,\mathrm{N}}{}^e$	$331.56°$	$331.48°$	$l_{0,\mathrm{N}}{}^e$	$331.95°$	$331.54°$	$l_{0,\mathrm{N}}{}^e$	$331.95°$	$331.60°$
$b_{0,\mathrm{N}}{}^f$	$-0.58°$	$-0.61°$	$b_{0,\mathrm{N}}{}^f$	$-0.34°$	$-0.65°$	$b_{0,\mathrm{N}}{}^f$	$-0.34°$	$-0.63°$
$\sigma_{\mathrm{N}}{}^g$	$0.22°$	$0.31°$	$\sigma_{\mathrm{N}}{}^g$	$0.46°$	$0.26°$	$\sigma_{\mathrm{N}}{}^g$	$0.47°$	$0.26°$
$l_{0,\mathrm{S}}{}^h$	$331.23°$	$331.21°$				$l_{0,\mathrm{S}}{}^h$	$331.63°$	$331.13°$
$b_{0,\mathrm{S}}{}^i$	$-0.77°$	$-0.74°$				$b_{0,\mathrm{S}}{}^i$	$-0.63°$	$-0.73°$
$\sigma_{\mathrm{S}}{}^l$	$0.10°$	$0.11°$				$\sigma_{\mathrm{S}}{}^l$	$0.14°$	$0.50°$

TABLE C.2: $\mathcal{L}_{\mathrm{AIC},H_0}$ values for the tested models, for both main and cross-check analysis. *: in this case the $\mathcal{L}_{\mathrm{AIC},H_0}$ refers to the improvement of the simple shell model with respect to the pure two-Gaussian scenario, i.e., the simple shell model better represents the source emission than the N+S one.

	$\mathcal{L}_{\mathrm{AIC},H_0}$ main	$\mathcal{L}_{\mathrm{AIC},H_0}$ x-check
N+S	$3.02 \times 10^{-2\star}$	$5.84 \times 10^{-6\star}$
shell+N	5.04×10^{-7}	1.22×10^{-1}
shell+N+S	8.32×10^{-7}	7.91×10^{-7}

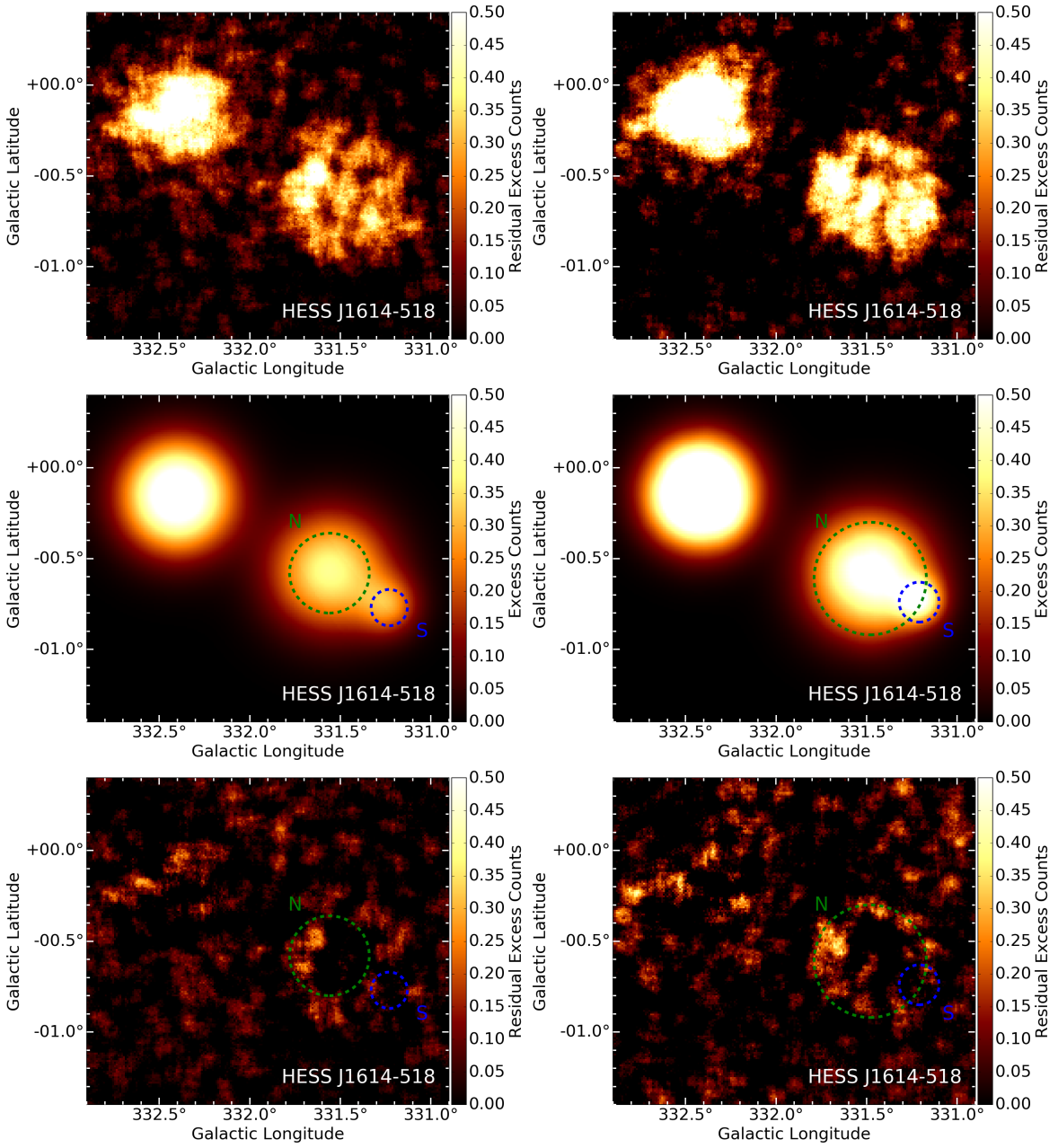

FIGURE C.1: Results from the morphological fit on the TeV SNR shell candidate HESS J1614−518. The left column shows the results obtained on the main analysis maps, while on the right the results from the cross-check one are displayed. *Top:* Residual excess counts after a background only fitting (On $-$ A $\times$ Bkg), smoothed with a $0.05°$ top-hat filter for visualization. *Middle*: Best-fit two-Gaussian model. The green and blue circles indicate the 1σ extension of N and S respectively. The other source appearing in the field of view (HESS J1616−508) has been modelled as additional Gaussian component. *Bottom*: Residual excess counts after modelling of the emission region with a two-Gaussian model, smoothed with a $0.05°$ top-hat filter for visualization. In both the main and cross-check analysis the centroid of the northern component displaces towards the middle of HESS J1614−518, trying to cover the SNR candidate's emission, and thus leaving the northern excess still *unmodelled*. A *pure* two-Gaussian model does not seem to be a sufficiently good representation of the TeV emission.

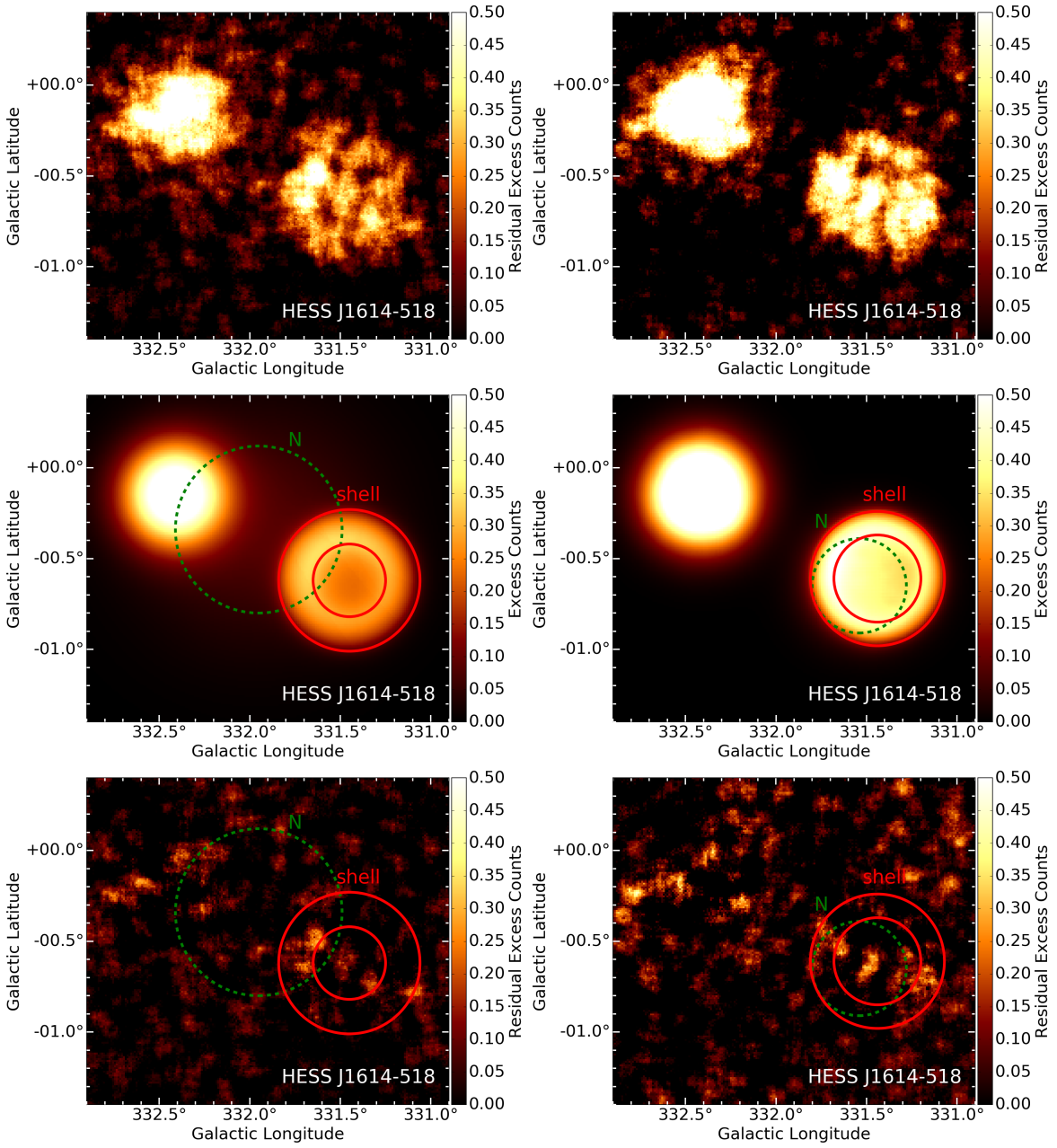

FIGURE C.2: Results from the morphological fit on the TeV SNR shell candidate HESS J1614−518. The left column shows the results obtained on the main analysis maps, while on the right the results from the cross-check one are displayed. *Top:* Residual excess counts after a background only fitting ($\mathrm{On} - A \times \mathrm{Bkg}$), smoothed with a $0.05°$ top-hat filter for visualization. *Middle*: Best-fit shell plus northern Gaussian model. The green circle indicates the 1σ extension of N; the red circles, instead, indicate the inner and outer radius of the shell model. The other source appearing in the field of view (HESS J1616−508) has been modelled as additional Gaussian component. *Bottom*: Residual excess counts after modelling of the emission region with shell plus northern Gaussian model, smoothed with a $0.05°$ top-hat filter for visualization. As it can be noticed for the main analysis, being this time the shell emission properly modelled, the northern Gaussian component mostly tries to cover the emission in-between HESS J1614−518 and HESS J1616−508. This is not the case for the cross-check analysis maps.

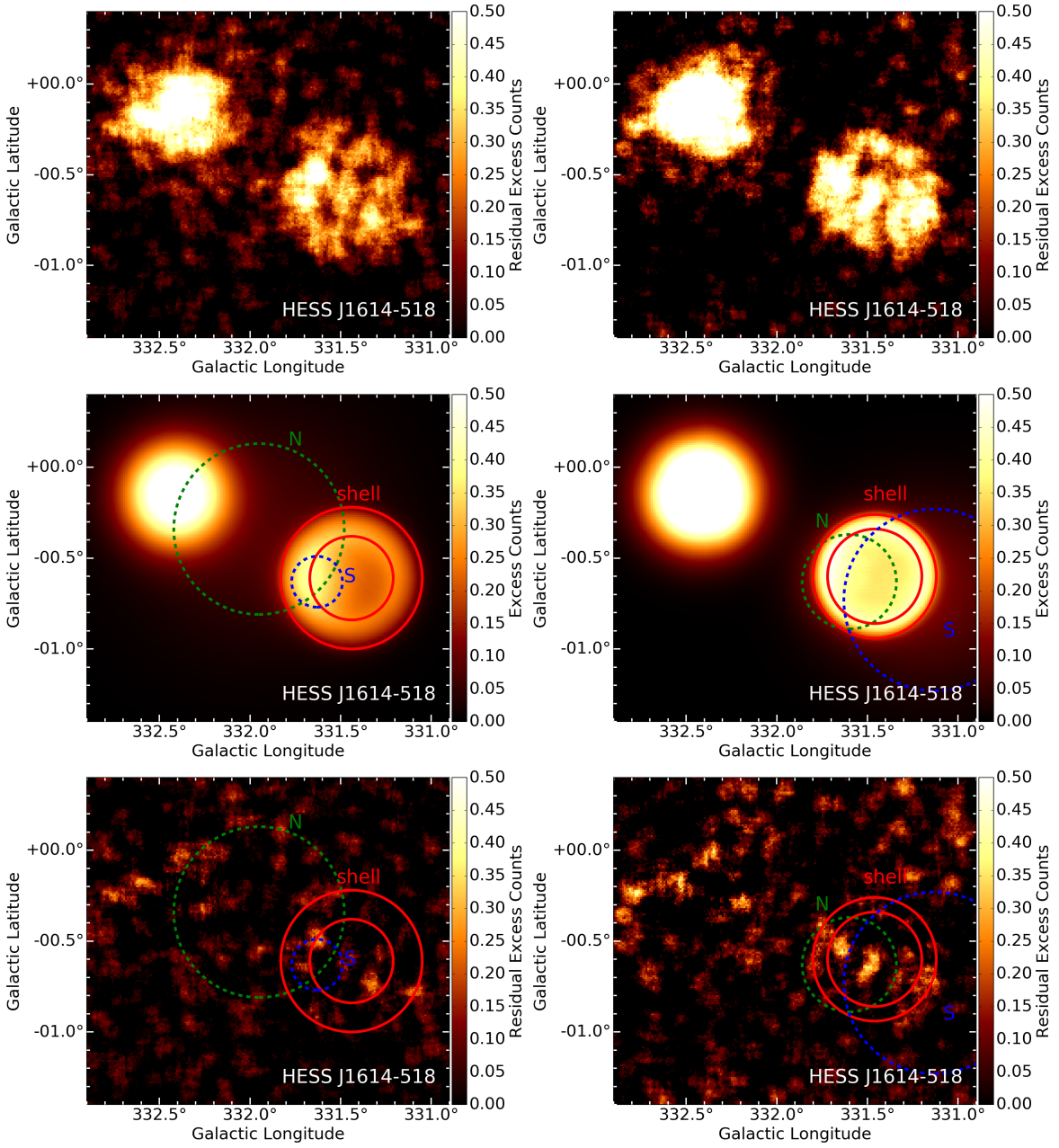

FIGURE C.3: Results from the morphological fit on the TeV SNR shell candidate HESS J1614−518. The left column shows the results obtained on the main analysis maps, while on the right the results from the cross-check one are displayed. *Top:* Residual excess counts after a background only fitting ($\mathrm{On} - A \times \mathrm{Bkg}$), smoothed with a 0.05° top-hat filter for visualization. *Middle*: Best-fit shell plus northern and southern Gaussian model. The green circles indicate the 1σ extension of N and S respectively; the red circles, instead, indicate the inner and outer radius of the shell model. The other source appearing in the field of view (HESS J1616−508) has been modelled as additional Gaussian component. *Bottom*: Residual excess counts after modelling of the emission region with shell plus northern and southern Gaussian model, smoothed with a 0.05° top-hat filter for visualization. For the main analysis, a situation similar to what shown in Figure C.2 takes place; additionally, the southern component tries to account for the northern spot. A similarly unstable situation for the southern component is present in the cross-check analysis; also in this case, a probable explanation is the presence of some low-level emission towards South of HESS J1614−518.

Bibliography

Acero, F. et al. (2009). "A joint spectro-imaging analysis of the XMM-Newton and HESS observations of the supernova remnant RX J1713.7-3946". In: *A&A* 505, pp. 157–167. DOI: 10.1051/0004-6361/200811556. arXiv: 0906.1073 [astro-ph.HE].

Acero, F. et al. (2010). "First detection of VHE γ-rays from SN 1006 by HESS". In: *A&A* 516, A62, A62. DOI: 10.1051/0004-6361/200913916. arXiv: 1004.2124 [astro-ph.HE].

Acero, F. et al. (2013). "Gamma-ray signatures of cosmic ray acceleration, propagation, and confinement in the era of CTA". In: *Astroparticle Physics* 43, pp. 276–286. DOI: 10.1016/j.astropartphys.2012.05.024. arXiv: 1209.0582 [astro-ph.HE].

Acero, F. et al. (2015). "Fermi Large Area Telescope Third Source Catalog". In: *ApJS* 218, 23, p. 23. DOI: 10.1088/0067-0049/218/2/23. arXiv: 1501.02003 [astro-ph.HE].

Ackermann, M. et al. (2013). "Detection of the Characteristic Pion-Decay Signature in Supernova Remnants". In: *Science* 339, pp. 807–811. DOI: 10.1126/science.1231160. arXiv: 1302.3307 [astro-ph.HE].

Aharonian, F. et al. (2006a). "A detailed spectral and morphological study of the gamma-ray supernova remnant <ASTROBJ>RX J1713.7-3946</ASTROBJ> with HESS". In: *A&A* 449, pp. 223–242. DOI: 10.1051/0004-6361:20054279. eprint: astro-ph/0511678.

Aharonian, F. et al. (2006b). "Observations of the Crab nebula with HESS". In: *A&A* 457, pp. 899–915. DOI: 10.1051/0004-6361:20065351. eprint: astro-ph/0607333.

Aharonian, F. et al. (2006c). "The H.E.S.S. Survey of the Inner Galaxy in Very High Energy Gamma Rays". In: *ApJ* 636, pp. 777–797. DOI: 10.1086/498013. eprint: astro-ph/0510397.

Aharonian, F. et al. (2007a). "Detection of extended very-high-energy γ-ray emission towards the young stellar cluster Westerlund 2". In: *A&A* 467, pp. 1075–1080. DOI: 10.1051/0004-6361:20066950. eprint: astro-ph/0703427.

Aharonian, F. et al. (2007b). "H.E.S.S. Observations of the Supernova Remnant RX J0852.0-4622: Shell-Type Morphology and Spectrum of a Widely Extended Very High Energy Gamma-Ray Source". In: *ApJ* 661, pp. 236–249. DOI: 10.1086/512603. eprint: astro-ph/0612495.

Aharonian, F. et al. (2008a). "Discovery of very-high-energy γ-ray emission from the vicinity of PSR J1913+1011 with HESS". In: *A&A* 484, pp. 435–440. DOI: 10.1051/0004-6361:20078715. arXiv: 0802.3841.

Aharonian, F. et al. (2008b). "HESS very-high-energy gamma-ray sources without identified counterparts". In: *A&A* 477, pp. 353–363. DOI: 10.1051/0004-6361:20078516. arXiv: 0712.1173.

Aharonian, F. A. (2004). *Very High Energy Cosmic Gamma Radiation - A Crucial Window on the Extreme Universe*. World Scientific Publishing.

Akaike, H. (1974). "A New Look at the Statistical Model Identification". In: *IEEE Transactions on Automatic Control* 19, pp. 716–723.

Aschenbach, B. (1998). "Discovery of a young nearby supernova remnant". In: *Nature* 396, pp. 141–142. DOI: 10.1038/24103.

Atwood, W. B. et al. (2009). "The Large Area Telescope on the Fermi Gamma-Ray Space Telescope Mission". In: *ApJ* 697, pp. 1071–1102. DOI: 10.1088/0004-637X/697/2/1071. arXiv: 0902.1089 [astro-ph.IM].

Bamba, A. et al. (2012). "Suzaku Observations of the Non-thermal Supernova Remnant HESS J1731-347". In: *ApJ* 756, 149, p. 149. DOI: 10.1088/0004-637X/756/2/149. arXiv: 1207.4182 [astro-ph.HE].

Bellamy, E.H. et al. (1994). "Absolute calibration and monitoring of a spectrometric channel using a photomultiplier". In: *Nuclear Instruments and Methods in Physics Research Section A: Accelerators, Spectrometers, Detectors and Associated Equipment* 339.3, pp. 468–476. ISSN: 0168-9002. DOI: https://doi.org/10.1016/0168-9002(94)90183-X. URL: http://www.sciencedirect.com/science/article/pii/016890029490183X.

Berge, D., S. Funk, and J. Hinton (2007). "Background modelling in very-high-energy γ-ray astronomy". In: *A&A* 466, pp. 1219–1229. DOI: 10.1051/0004-6361:20066674. eprint: astro-ph/0610959.

Bolz, O. (2004). "Absolute Energiekalibration der abbildenden Cherenkov-Teleskope des H.E.S.S. Experiments und Ergebnisse erster Beobachtungen des Supernova-Überrests RX J1713.7-3946". In: *PhD thesis, Ruprecht-Karls-Universität Heidelberg*.

Burnham, K. P. and D. R. Anderson (2002). *Model selection and multimodel inference : a practical information theoretic approach, 2. ed*. Springer.

Burton, M. G. et al. (2013). "The Mopra Southern Galactic Plane CO Survey". In: *PASA* 30, e044, e044. DOI: 10.1017/pasa.2013.22. arXiv: 1307.1027.

Capasso, M. et al. (2017). "The TeV supernova remnant shell HESS J1731-347 and its surroundings". In: *6th International Symposium on High Energy Gamma-Ray Astronomy*. Vol. 1792. American Institute of Physics Conference Series, p. 040026. DOI: 10.1063/1.4968930. arXiv: 1612.00258 [astro-ph.HE].

Case, G. L. and D. Bhattacharya (1998). "A New Σ-D Relation and Its Application to the Galactic Supernova Remnant Distribution". In: *ApJ* 504, pp. 761–772. DOI: 10.1086/306089. eprint: astro-ph/9807162.

Cash, W. (1979). "Parameter estimation in astronomy through application of the likelihood ratio". In: *ApJ* 228, pp. 939–947. DOI: 10.1086/156922.

Cherenkov Telescope Array Consortium, T. et al. (2017). "Science with the Cherenkov Telescope Array". In: *ArXiv e-prints*. arXiv: 1709.07997 [astro-ph.IM].

Cui, Y., G. Pühlhofer, and A. Santangelo (2016). "A young supernova remnant illuminating nearby molecular clouds with cosmic rays". In: *A&A* 591, A68, A68. DOI: 10.1051/0004-6361/201628505. arXiv: 1605.00483 [astro-ph.HE].

de Naurois, M. and L. Rolland (2009). "A high performance likelihood reconstruction of γ-rays for imaging atmospheric Cherenkov telescopes". In: *Astroparticle Physics* 32, pp. 231–252. DOI: 10.1016/j.astropartphys.2009.09.001. arXiv: 0907.2610 [astro-ph.IM].

Donath, A. et al. (2015). "Gammapy: An open-source Python package for gamma-ray astronomy". In: *34th International Cosmic Ray Conference (ICRC2015)*. Vol. 34. International Cosmic Ray Conference, p. 789. arXiv: 1509.07408 [astro-ph.IM].

Doroshenko, V. et al. (2017). "XMM-Newton observations of the non-thermal supernova remnant HESS J1731-347 (G353.6-0.7)". In: *A&A* 608, A23, A23. DOI: 10.1051/0004-6361/201730983. arXiv: 1708.04110 [astro-ph.HE].

Dubus, G. (2013). "Gamma-ray binaries and related systems". In: *A&A Rev.* 21, 64, p. 64. DOI: 10.1007/s00159-013-0064-5. arXiv: 1307.7083 [astro-ph.HE].

Eadie, W. T., D. Drijard, and F. E. James (1971). *Statistical methods in experimental physics*.

Fukuda, T. et al. (2014). "Interstellar Protons in the TeV γ-Ray SNR HESS J1731-347: Possible Evidence for the Coexistence of Hadronic and Leptonic γ-Rays". In: *ApJ* 788, 94, p. 94. DOI: 10.1088/0004-637X/788/1/94. arXiv: 1405.2599 [astro-ph.HE].

Fukui, Y. et al. (2003). "Discovery of Interacting Molecular Gas toward the TeV Gamma-Ray Peak of the SNR G 347.3–0.5". In: *PASJ* 55, pp. L61–L64. DOI: 10.1093/pasj/55.5.L61.

Gabici, S. and F. A. Aharonian (2007). "Searching for Galactic Cosmic-Ray Pevatrons with Multi-TeV Gamma Rays and Neutrinos". In: *ApJ* 665, pp. L131–L134. DOI: 10.1086/521047. arXiv: 0705.3011.

Gadola, Arno (2013). "Towards the First Imaging Atmospheric Cherenkov Telescope Camera with Continuous Signal Digitization Towards the First Imaging Atmospheric Cherenkov Telescope Camera with Continuous Signal Digitization Towards the First Imaging Atmospheric Cherenkov Telescope Camera with Continuous Signal Digitization". PhD thesis. Universität Zürich.

Gaensler, B. M. and P. O. Slane (2006). "The Evolution and Structure of Pulsar Wind Nebulae". In: *ARA&A* 44, pp. 17–47. DOI: 10.1146/annurev.astro.44.051905.092528. eprint: astro-ph/0601081.

Gaisser, Thomas K. (1990). *Cosmic Rays and Particle Physics*. Cambridge University Press.

Giordano, F. et al. (2012). "Fermi Large Area Telescope Detection of the Young Supernova Remnant Tycho". In: *ApJ* 744, L2, p. L2. DOI: 10.1088/2041-8205/744/1/L2. arXiv: 1108.0265 [astro-ph.HE].

Glicenstein, J.-F. and M. Shayduk (2017). "NectarCAM, a camera for the medium sized telescopes of the Cherenkov telescope array". In: *6th International Symposium on High Energy Gamma-Ray Astronomy*. Vol. 1792. American Institute of Physics Conference Series, p. 080009. DOI: 10.1063/1.4969030. arXiv: 1610.04173 [astro-ph.IM].

Green, A. J., S. N. Reeves, and T. Murphy (2014). "The Second Epoch Molonglo Galactic Plane Survey: Images and Candidate Supernova Remnants". In: *PASA* 31, e042, e042. DOI: 10.1017/pasa.2014.37. arXiv: 1410.8247.

Green, D. A. (1984). "Statistical studies of supernova remnants". In: *MNRAS* 209, pp. 449–478. DOI: 10.1093/mnras/209.3.449.

Grieder, P. K. F. (2010). *Extensive Air Shower*. High Energy Phenomena and Astrophysical Aspects.

Hahn, J. et al. (2014). "Impact of aerosols and adverse atmospheric conditions on the data quality for spectral analysis of the H.E.S.S. telescopes". In: *Astroparticle Physics* 54, pp. 25–32. DOI: 10.1016/j.astropartphys.2013.10.003. arXiv: 1310.1639 [astro-ph.IM].

H.E.S.S. Collaboration (2011). "A new SNR with TeV shell-type morphology: HESS J1731-347". In: *A&A* 531, A81, A81. DOI: 10.1051/0004-6361/201016425. arXiv: 1105.3206 [astro-ph.HE].

— (2016a). "Acceleration of petaelectronvolt protons in the Galactic Centre". In: *Nature* 531, pp. 476–479. DOI: 10.1038/nature17147. arXiv: 1603.07730 [astro-ph.HE].

— (2016b). "Deeper H.E.S.S. Observations of Vela Junior (RX J0852.0-4622): Morphology Studies and Resolved Spectroscopy". In: *ArXiv e-prints*. arXiv: 1611.01863 [astro-ph.HE].

— (2016c). "Detailed spectral and morphological analysis of the shell type SNR RCW 86". In: *ArXiv e-prints*. arXiv: 1601.04461 [astro-ph.HE].

— (2016d). "H.E.S.S. observations of RX J1713.7-3946 with improved angular and spectral resolution; evidence for gamma-ray emission extending beyond the X-ray emitting shell". In: *ArXiv e-prints*. arXiv: 1609.08671 [astro-ph.HE].

H.E.S.S. Collaboration et al. (2018a). "A search for new supernova remnant shells in the Galactic plane with H.E.S.S." In: *A&A* 612, A8. DOI: 10.1051/0004-6361/201730737. URL: https://doi.org/10.1051/0004-6361/201730737.

H.E.S.S. Collaboration et al. (2018b). "The H.E.S.S. Galactic plane survey". In: *A&A* 612, A1. DOI: 10.1051/0004-6361/201732098. URL: https://doi.org/10.1051/0004-6361/201732098.

Hillas, A. M. (1985). "Cerenkov light images of EAS produced by primary gamma". In: *International Cosmic Ray Conference* 3.

Holder, J. (2011). "VERITAS: Status and Highlights". In: *International Cosmic Ray Conference* 12, p. 137. DOI: 10.7529/ICRC2011/V12/H11. arXiv: 1111.1225 [astro-ph.HE].

Holler, M. et al. (2015). "Observations of the Crab Nebula with H.E.S.S. Phase II". In: *ArXiv e-prints*. arXiv: 1509.02902 [astro-ph.HE].

Kelner, S. R., F. A. Aharonian, and V. V. Bugayov (2006). "Energy spectra of gamma rays, electrons, and neutrinos produced at proton-proton interactions in the very high energy regime". In: *Phys. Rev. D* 74.3, 034018, p. 034018. DOI: 10.1103/PhysRevD.74.034018. eprint: astro-ph/0606058.

Klochkov, D. et al. (2015). "The neutron star in HESS J1731-347: Central compact objects as laboratories to study the equation of state of superdense matter". In: *A&A* 573, A53, A53. DOI: 10.1051/0004-6361/201424683. arXiv: 1410.1055 [astro-ph.HE].

Knoll, G. F. (2000). *Radiation Detection and Measurement*. John Wiley & Sons.

Koyama, K. et al. (2007). "X-Ray Imaging Spectrometer (XIS) on Board Suzaku". In: *PASJ* 59, pp. 23–33. DOI: 10.1093/pasj/59.sp1.S23.

Lazendic, J. S. et al. (2004). "A High-Resolution Study of Nonthermal Radio and X-Ray Emission from Supernova Remnant G347.3-0.5". In: *ApJ* 602, pp. 271–285. DOI: 10.1086/380956. eprint: astro-ph/0310696.

Li, T.-P. and Y.-Q. Ma (1983). "Analysis methods for results in gamma-ray astronomy". In: *ApJ* 272, pp. 317–324. DOI: 10.1086/161295.

Longair, M. S. (2011). *High energy astrophysics*. Cambridge University Press.

Matthews, J. (2005). "A Heitler model of extensive air showers". In: *Astroparticle Physics* 22, pp. 387–397. DOI: 10.1016/j.astropartphys.2004.09.003.

Maxted, N. et al. (2017). "Probing The Local Environment of the Supernova Remnant HESS J1731-347 with CO and CS Observations". In: *ArXiv e-prints*. arXiv: 1710.06101 [astro-ph.HE].

— (2018). "Probing the local environment of the supernova remnant HESS J1731-347 with CO and CS observations". In: *MNRAS* 474, pp. 662–676. DOI: 10.1093/mnras/stx2727. arXiv: 1710.06101 [astro-ph.HE].

Mitsuda, K. et al. (2007). "The X-Ray Observatory Suzaku". In: *PASJ* 59, S1–S7. DOI: 10.1093/pasj/59.sp1.S1.

Nakanishi, H. and Y. Sofue (2006). "Three-Dimensional Distribution of the ISM in the Milky Way Galaxy: II. The Molecular Gas Disk". In: *PASJ* 58, pp. 847–860. DOI: 10.1093/pasj/58.5.847. eprint: astro-ph/0610769.

Ohm, S., C. van Eldik, and K. Egberts (2009). "γ/hadron separation in very-high-energy γ-ray astronomy using a multivariate analysis method". In: *Astroparticle Physics* 31, pp. 383–391. DOI: 10.1016/j.astropartphys.2009.04.001. arXiv: 0904.1136 [astro-ph.IM].

Press, W. H. et al. (1992). *Numerical Recipes in C*. Cambridge University Press.

Protassov, R. et al. (2002). "Statistics, Handle with Care: Detecting Multiple Model Components with the Likelihood Ratio Test". In: *ApJ* 571, pp. 545–559. DOI: 10.1086/339856. eprint: astro-ph/0201547.

Puehlhofer, Gerd et al. (2015). "FlashCam: a fully-digital camera for the medium-sized telescopes of the Cherenkov Telescope Array". In: DOI: 10.22323/1.236.1039.

Reynolds, S. P. (2011). "Particle acceleration in supernova-remnant shocks". In: *Ap&SS* 336, pp. 257–262. DOI: 10.1007/s10509-010-0559-8. arXiv: 1012.1306 [astro-ph.HE].

Reynolds, Stephen P. (2008). "Supernova Remnants at High Energy". In: *Annual Review of Astronomy and Astrophysics* 46.1, pp. 89–126. DOI: 10.1146/annurev.astro.46.060407.145237. eprint: https://doi.org/10.1146/annurev.astro.46.

060407.145237. URL: https://doi.org/10.1146/annurev.astro.46.060407.145237.

Slane, P. et al. (2001). "RX J0852.0-4622: Another Nonthermal Shell-Type Supernova Remnant (G266.2-1.2)". In: *ApJ* 548, pp. 814–819. DOI: 10.1086/319033. eprint: astro-ph/0010510.

Tian, W. W. et al. (2008). "Discovery of the Radio and X-Ray Counterpart of TeV γ-Ray Source HESS J1731-347". In: *ApJ* 679, L85, p. L85. DOI: 10.1086/589506. arXiv: 0801.3254.

Vallée, J. P. (2014). "The Spiral Arms of the Milky Way: The Relative Location of Each Different Arm Tracer within a Typical Spiral Arm Width". In: *AJ* 148, 5, p. 5. DOI: 10.1088/0004-6256/148/1/5.

Völk, H. J. and K. Bernlöhr (2009). "Imaging very high energy gamma-ray telescopes". In: *Experimental Astronomy* 25, pp. 173–191. DOI: 10.1007/s10686-009-9151-z. arXiv: 0812.4198.

Weekes, T. C. et al. (1989). "Observation of TeV gamma rays from the Crab nebula using the atmospheric Cerenkov imaging technique". In: *ApJ* 342, pp. 379–395. DOI: 10.1086/167599.

Werner, F. et al. (2017). "Performance verification of the FlashCam prototype camera for the Cherenkov Telescope Array". In: *Nuclear Instruments and Methods in Physics Research A* 876, pp. 31–34. DOI: 10.1016/j.nima.2016.12.056. arXiv: 1612.09528 [astro-ph.IM].

Yamazaki, R. et al. (2006). "TeV γ-rays from old supernova remnants". In: *MNRAS* 371, pp. 1975–1982. DOI: 10.1111/j.1365-2966.2006.10832.x. eprint: astro-ph/0601704.

Zirakashvili, V. N. and V. S. Ptuskin (2008). "Diffusive Shock Acceleration with Magnetic Amplification by Nonresonant Streaming Instability in Supernova Remnants". In: *ApJ* 678, 939-949, pp. 939–949. DOI: 10.1086/529580. arXiv: 0801.4488.

Acknowledgments

Along the path of my education, this is the third time I am granted the privilege to express my gratitude for the realization of a thesis work. The consciousness that nobody is self-made and the ineffable need to take a deep breath and say *thank you*, are probably the highest moments a man can experience in his life, and it always feels extraordinary when they come.

Punctual as always, come however the apologies for anybody I might forget: please forgive me if your names are not on these pages, the help and support I surely received are not less important, nor were less appreciated.

First of all I would like to thank Prof. Dott. Andrea Santangelo, for giving me the opportunity to join the IAAT and for supervising my work. Thank you for taking the time to give me advice, were it scientific or not.

My gratitude also extends to Prof. Dr. Jochum, for agreeing to be my advisor and for the always pleasant meetings of the Kepler Center.

To Dr. Gerd Pühlhofer: thank you for guiding me within the H.E.S.S. Collaboration and the FlashCam team. Thank you for your questions, for the patience to listen and answer to mine, for your tireless thoroughness. I hope you enjoyed supervising my work at least as much as I did learning from you.

To Dr. Chris J. Tenzer and Thomas Schanz: thank you for your abnegation in caring and supporting the Institute in every little detail, constantly and relentlessly. Thank you for always being there, for the inspiration you were and still are to me.

To Dr. Helene Tenzer: thank you for your kindness and hospitality, I had a really great time.

To Dr. Daniel Gottschall: thank you for welcoming me even before I actually arrived at the Institute for the first time. Thank you for helping me moving my first steps within H.E.S.S., for the meetings together. You are welcome for the plants, I would have never let them die! Jokes aside and more importantly, thank you for being my colleague.

Within the members of the H.E.S.S. Collaboration, a special thanks goes to Benjamin and Nigel for working together on HESS J1731−347, and to the whole new shells task group: without your support this work would have not seen the light.

A special thanks goes also to Nebiha, for accompanying me throughout the shift in Namibia, and to the local crew as well. To Volker, Albert, Frikkie and Toni: thank you for your patient work, for your insights on the instrument, for your support during a wonderfully though month at the H.E.S.S. site. Thank you Volker for the night talks, for your being straight and kind at the same time.

To the FlashCam team: thanks for letting me be part of such a highly motivated and driven work group.

To all the great colleagues at the Institute: thank you for sharing a part of the way with me. A slice of cake, a coffee, a football match, the painful process of searching for a flat in Tübingen, a piece of advice. Thanks to Sebastian, Felix, Jörg, Gabi, Jürgen, Martina, Conny, Sara, Samuel, Lisa, Emanuele, Yudong, Cristian, the Ducci.

To all the friends met outside the University: to Vera, Luca, Marco, Valeria, Tinka, Frieder, Johnny and Caro. You made my life in Tübingen unforgettable, thank you for the time spent together.

To my first *colleagues*, now proudly Doktoren: to Leo and Riccardo. Thank you for the last ten years and for growing together, even though often far away.

To all my new colleagues at FBK: it is also thanks to your support that I could make it throughout this effort.

To Mamma, Papà and Stefania: thank you for leading the way, for letting me fly so far and yet hold my hand tight. This thesis is truly more your achievement than it is mine.

To Alexandra: thank you for the last year, for supporting me and for *caterpillaring* together.

To Nonno Ciro and Nonna Mina: please accept my apologies for having taken so long to finish.

Once more, to the reader who had the courage to arrive this far in reading: thank you! I hope you enjoyed the work.